

BULLETIN OF MAGNETIC RESONANCE

*The Quarterly Review Journal of the
International Society of Magnetic Resonance*

VOLUME 15

February 1993

NUMBER 3

Contents

PROCEEDINGS OF THE XITH MEETING
OF THE INTERNATIONAL SOCIETY OF
MAGNETIC RESONANCE, PART III 141

REVIEW

Spin Counting in Dipolar Coupled Spin 1/2
Systems by Multiple Quantum Coherence,
Son-Jong Hwang and B. C. Gerstein 211

CALENDAR OF FORTHCOMING
CONFERENCES 229

RECENT MAGNETIC RESONANCE BOOKS . 231

INSTRUCTIONS FOR AUTHORS 238

BULLETIN OF MAGNETIC RESONANCE

*The Quarterly Review Journal of the
International Society of Magnetic Resonance*

Editor:

DAVID G. GORENSTEIN

*Department of Chemistry
Purdue University
West Lafayette, IN 47907 U.S.A.
Fax: 317-494-0230
INTERNET: david@chem.purdue.edu*

Editorial Board:

E.R. ANDREW

*University of Florida
Gainesville, Florida, U.S.A.*

LAWRENCE BERLINER

*Ohio State University
Columbus, Ohio, U.S.A.*

ROBERT BLINC

*E. Kardelj University of Ljubljana
Ljubljana, Yugoslavia*

H. CHIHARA

*Osaka University
Toyonaka, Japan*

GARETH R. EATON

*University of Denver
Denver, Colorado, U.S.A.*

DANIEL FIAT

*University of Illinois at Chicago
Chicago, Illinois, U.S.A.*

SHIZUO FUJIWARA

*University of Tokyo
Bunkyo-Ku, Tokyo, Japan*

DAVID GRANT

*University of Utah
Salt Lake City, Utah, U.S.A.*

ALEXANDER PINES

*University of California
Berkeley, California, U.S.A.*

MIK PINTAR

*University of Waterloo
Waterloo, Ontario, Canada*

CHARLES P. POOLE, JR.

*University of South Carolina
Columbia, South Carolina, U.S.A.*

BRIAN SYKES

*University of Alberta
Edmonton, Alberta, Canada*

The *Bulletin of Magnetic Resonance* is a quarterly review journal by the International Society of Magnetic Resonance. Reviews cover all parts of the broad field of magnetic resonance, viz., the theory and practice of nuclear magnetic resonance, electron paramagnetic resonance, and nuclear quadrupole resonance spectroscopy including applications in physics, chemistry, biology, and medicine. The *BULLETIN* also acts as a house journal for the International Society of Magnetic Resonance.

CODEN: BUMRDT

ISSN: 0163-559X

Bulletin of Magnetic Resonance, The Quarterly Journal of International Society of Magnetic Resonance. 1993 copyright by the International Society of Magnetic Resonance. Rates: Libraries and non-ISMAR members \$80.00, members of ISMAR, \$25.00. All subscriptions are for a volume year. All rights reserved. No part of this journal may be reproduced in any form for any purpose or by any means, abstracted, or entered into any data base, electronic or otherwise, without specific permission in writing from the publisher.

Council of the International Society of Magnetic Resonance

President: R. FREEMAN, England

Vice-President: A. PINES, U.S.A.

Founding Chairman: D. FIAT, U.S.A.

Secretary-General: R.K. HARRIS, England

Treasurer: R.R. VOLD, U.S.A.

Past President: C.P. SLICHTER, U.S.A.

J. ANGLISTER
Israel

E.D. BECKER
U.S.A.

M.R. BENDALL
Australia

R. BLINC
Yugoslavia

G. BODENHAUSEN
Switzerland

W.S. BREY
U.S.A.

P.T. CALLAGHAN
New Zealand

H. CHIHARA
Japan

S. CLOUGH
England

L.G. CONTI
Italy

R. DESLAURIERS
Canada

R.R. ERNST
Switzerland

E.L. HAHN
U.S.A.

K.H. HAUSSER
Germany

J.W. HENNEL
Poland

M.J.R. HOCH
S. Africa

C.L. KHETRAPAL
India

V.J. KOWALEWSKI
Argentina

P.C. LAUTERBUR
U.S.A.

E. LIPPMAA
Estonia

B. MARAVIGLIA
Italy

M. MEHRING
Germany

H. PFEIFER
Germany

M.M. PINTAR
Canada

C.P. POOLE
U.S.A.

M. PUNKINEN
Finland

L.W. REEVES
Canada

G.C.K. ROBERTS
England

P. SERVOZ-GAVIN
France

J. STANKOWSKI
Poland

N.V. VUGMAN
Brazil

J.S. WAUGH
U.S.A.

K. WUTHRICH
Switzerland

C.S. YANNONI
U.S.A.

The aims of the International Society of Magnetic Resonance are to advance and diffuse knowledge of magnetic resonance and its applications in physics, chemistry, biology, and medicine, and to encourage and develop international contacts between scientists.

The Society sponsors international meetings and schools in magnetic resonance and its applications and publishes the quarterly review journal. The *Bulletin of Magnetic Resonance*, the house journal of ISMAR.

The annual fee for ISMAR membership is \$20 plus \$25 for a member subscription to the *Bulletin of Magnetic Resonance*.

Send subscription to:

International Society of Magnetic Resonance
Professor Regitze R. Vold, Treasurer
Department of Chemistry, 0342
University of California, San Diego
9500 Gilman Drive
La Jolla, CA 92093-0342
(619) 534-0200; FAX (619) 534-7042
Bitnet: rvold@ucsd.bitnet

**Proceedings of the XIth Meeting of the
International Society of Magnetic Resonance**

Part III

July 19 - 24, 1992

Vancouver, B. C. Canada

Co-Editors: D. G. Gorenstein and C. A. Fyfe

Contents

Interactions of Hirudin Analogs with Bovine and Human Thrombins: ESR Studies, L. J. Berliner and J. K. Woodford	142
The NMR Spectra of Homonuclear Two-Spin Systems Under Magic-Angle and Off-Magic-Angle Spinning, T. Nakai and C. A. McDowell	149
Coreflood Experiments on Casper Sandstone: Using Magnetic Resonance Imaging to Measure Flow Velocities, M. Robinson Merrill	154
NMR Imaging of Solid Polymers, D. G. Cory and W. E. Maas	160
Biochemical and Biophysical Effects of Dexamethasone on Human Lymphoblastoid Cell Lines, Studied by ³¹P and ¹H NMR Spectroscopy and Fluorimetry, R. Ricciolini, A. Miccheli, E. Piccolella, A. Tomassini, C. Manetti, M. E. Di Cocco and F. Conti	165
Peripheral Arteriopathy in the Rat: Effect of Levocarnitine Propil Treatment Stud- ied by ³¹P NMR Spectroscopy, T. Aureli, G. Capuani, M. E. Di Cocco, A. Miccheli, N. Corsico, A. Nardone, E. Arrigoni Martelli and F. Conti	169
Tunnel Splitting of 2,3-Butanedione with Pressure Studied Using Low-field NMR Tunnelling Spectroscopy, P. M. Debenham, P. J. McDonald, A. J. Horsewill and D. Vijayaraghavan	172
Spin-Lattice Relaxation for Dideuterium, L. C. ter Beek and E. E. Burnell	175
High-Resolution ¹³C and ¹⁵N Solid-State NMR Investigations of the Curing Re- action of Cyanate Resins, C. A. Fyfe, J. Niu, S. Rettig, N. E. Burlinson, C. Reidsema, D. Wang and M. Poliks	179
³¹P NMR Study on Phytase - Catalyzed Hydrolysis of Phytate, E. Brosio, E. Carnovale, M. Delfini, L. Pizzoferrato and G. Veglia	183
Molecular Beam Magnetic Resonance via the Longitudinal Stern-Gerlach Effect, L. J. Mueller and D. P. Weitekamp	187
Fourier-Transform Time-Sequenced Optical Nuclear Magnetic Resonance of Gallium Arsenide, S. K. Buratto, J. Y. Hwang, N. D. Kurur, D. N. Shykind and D. P. Weitekamp	190
NMR Characterization of the Homopolymers and Copolymers Formed from Tetraethoxysilane and Methytriethoxysilane in a Sol-Gel Process, C. A. Fyfe, P. P. Aroca and Y. Zhang	195
Comparison of Short-Range Interactions in Zero Electric Field Gradient Mixtures, T. Chandrakumar and E. E. Burnell	199
²H NMR Studies of Membrane Stabilization by Vitamin E, S. R. Wassall, S. Ayalasomayajula, G. L. Griffith, M. A. McCabe, W. D. Ehringer and W. Stillwell	205

Interactions of Hirudin Analogs with Bovine and Human Thrombins: ESR Studies

L. J. Berliner

Department of Chemistry, The Ohio State University,
120 West 18th Avenue, Columbus, Ohio 43210-1173, U.S.A.

and

J. K. Woodford

University of Cincinnati, Dept. of Pharmacology and Medicinal Chemistry
Med Center ML #4, Cincinnati, OH 45627-0004, U.S.A.

1 Introduction

Hirudin is a 65 amino acid thrombin specific inhibitor from the leech, *hirudis mecidinales*. It is currently the most potent anticoagulant thrombin inhibitor known. The interactions between thrombin and synthetic or natural (polypeptide) inhibitors has been characterized by x-ray crystallography. However, elements of structural disorder in the x-ray picture are always clouded by the following uncertainties: are there multiple conformers of the protein crystal packing effects or did true conformational changes result from the enzyme:inhibitor interactions?

NMR work by Scheraga and co-workers [1] with bovine thrombin and various hirudin and C-terminal inhibitor analogs showed that certain regions of these inhibitors (and/or the enzyme) were too mobile to resolve by TRNOE. Furthermore, rapid kinetics measurements by Stone and Hofsteenge [2] strongly suggest that multiple binding steps occur in thrombin:hirudin complex formation. The studies outlined below exemplifies the application of spin labeling as a probe of local, dynamic structural changes of thrombin in solution.

The technique utilizes the active site probes depicted in Figure 1 [3], [4]. The ESR spectrum

reflects the mobility and hence the local interactions between the nitroxide ring and the protein. These interactions are primarily hydrophobic (van der Waals contacts) with some contributions from steric restrictions. While specific assignments of protein residues are impossible to assign by ESR alone, changes in this region which alter protein-nitroxide interactions are detectable with high sensitivity. Most of the work in the thrombin field involves nitroxides which contain the reactive, serine-195 specific sulfonyl fluoride group. This results in a covalent sulfonate linkage which is isostructural to the tetrahedral intermediate in the mechanism of serine proteases. These probes, which are of dimensions of 10 to 15 Å in length, are sensitive both to ligands binding in the substrate binding pocket as well as conformational changes elicited from points distant to the active site [5].

The ESR method can detect small, yet significant differences in structure and conformation between bovine and human thrombin, respectively. With the high level of sequence homology and x-ray structures reported for both proteins we know that the differences at the three dimensional static level are slight [6] - [8]. Yet several pieces of indirect evidence have suggested unusual differences, such as reactivity with exosite benzamidine affinity label analogs [9], the fibrinogen clotting behavior of the

Figure 1. Structures of sulfonyl fluoride spin label used in this study. The spin label nomenclature is described in Berliner et al. (12). The arrows (\downarrow) denote the bond attacked by Ser195. p-IV (*p*-CO-6NH), 4-(2,2,6,6-tetramethyl piperidine-1-oxyl)-*p*-(fluorosulfonyl)-benzamide; p-V (*p*-CO-5NH), 4-(2,2,5,5-tetramethyl-pyrrolidine-1-oxyl)-*p*-(fluorosulfonyl)benzamide; m-IV (*m*-CO-6NH, 4-(2,2,6,6-tetramethyl-piperidine-1-oxyl)-*m*-(fluorosulfonyl)benzamide; m-V (*m*-CO-5NH), 3-(2,2,5,5-tetramethyl-pyrrolidine-1-oxyl)-*m*-(fluorosulfonyl)-benzamide; m-VI (*m*-NCO-6 OH), *N*-(*m*-fluorosulfonyl-benzene)-4-*O*-(2,2,6,6-tetramethyl piperidine-1-oxyl) carbamate; m-VII (*m*-NCO-6NH), *N*-(*m*-[fluorosulfonyl]phenyl)-4-*N*-(2,2,6,6-tetramethyl-piperidine-1-oxyl) urea. From [4] with permission.

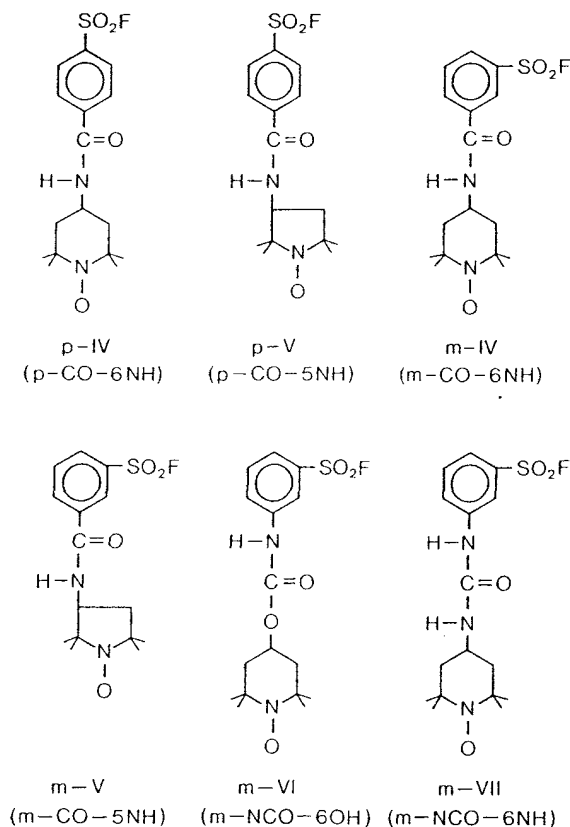


Figure 2. X-band ESR spectra of active site spin labeled human and bovine α -thrombins (A) m-V labeled human α -thrombin; (B) m-V bovine α -thrombin, (C) p-V human α -thrombin in the presence of saturating sucrose; (D) p-V bovine α -thrombin in the presence of saturating sucrose; (E) p-V bovine α -thrombin in the presence of 10 mM indole, and saturating sucrose. Conditions were pH 6.5, 0.05 M Tris-HCl, 0.75 M NaCl, 20° C. Protein concentrations were typically 0.07-0.08 mM. Arrows (\downarrow) indicate points used in determining the maximum hyperfine splitting ($2 T_{||}$). From [4] with permission.

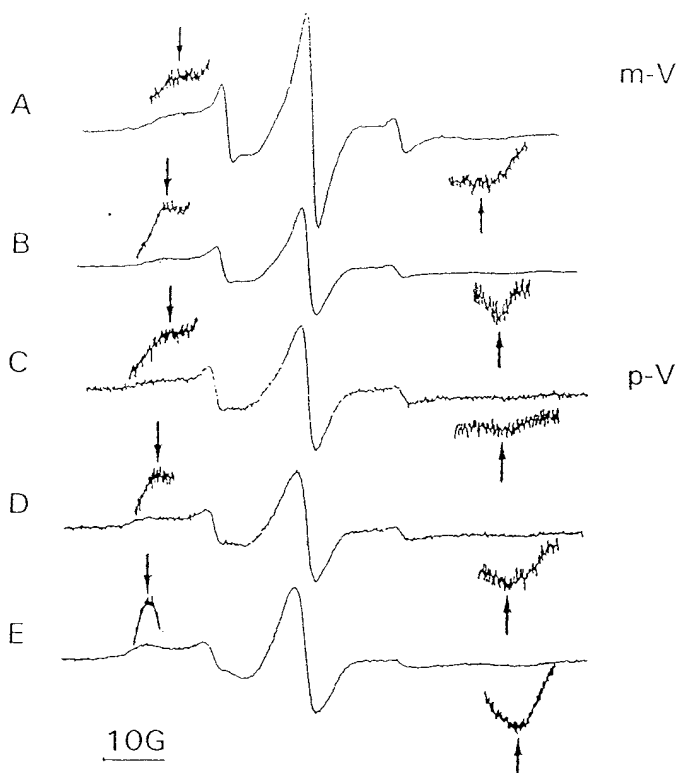


Table 1. Sequences of HV2-Lys47, and 21-mer and 12-mer C-terminal fragments.

HV2-Lys47	
Ile-Thr-Tyr-Thr-Asp-Cys-Thr-Glu-Ser-Gly-Gln-Asn-Leu-Cys-Leu-Cys-Glu-Gly-Ser-Asn-Val-Cys-	22
1	
Gly-Lys-Gly-Asn-Lys-Cys-Ile-Leu-Gly-Ser-Asn-Gly-Lys-Gly-Asn-Gln-Cys-Val-Thr-Gly-Glu-Gly-	44
23	
Thr-Pro-Lys-Pro-Glu-Ser-His-Asn-Asn-Gly-Asp-Phe-Glu-Glu-Ile-Pro-Glu-Glu-Tyr-Leu-Gln	65
45	
21-mer	
Thr-Pro-Lys-Pro-Gln-Ser-His-Asn-Asp-Gly-Asp-Phe-Glu-Glu-Ile-Pro-Glu-Glu-Tyr-Leu-Gln	65
45	
12-mer	
Gly-Asp-Phe-Glu-Glu-Ile-Pro-Glu-Glu-Tyr-Leu-Gln	65
54	

Table 2. Primary sequences of HV1 and HV2-Lys47.

HV1	Val-Val-Tyr-Thr-Asp-Cys-Thr-Glu-Ser-Gly
HV2-Lys47	Ile-Thr-Tyr-Thr-Asp-Cys-Thr-Glu-Ser-Gly
	1 10
HV1	Gln-Asn-Leu-Cys-Leu-Cys-Glu-Gly-Ser-Asn
HV2-Lys47	Gln-Asn-Leu-Cys-Leu-Cys-Glu-Gly-Ser-Asn
	11 20
HV1	Val-Cys-Gly-Gln-Gly-Asn-Lys-Cys-Ile-Leu
HV2-Lys47	Val-Cys-Gly-Lys-Gly-Asn-Lys-Cys-Ile-Leu
	21 30
HV1	Gly-Ser-Asp-Gly-Glu-Lys-Asn-Gln-Cys-Val
HV2-Lys47	Gly-Ser-Asn-Gly-Lys-Gly-Asn-Gln-Cys-Val
	31 40
HV1	Thr-Gly-Glu-Gly-Thr-Pro-Lys-Pro-Gln-Ser
HV2-Lys47	Thr-Gly-Glu-Gly-Thr-Pro-Asn-Pro-Glu-Ser
	41 50
HV1	His-Asn-Asp-Gly-Asp-Phe-Glu-Glu-Ile-Pro
HV2-Lys47	His-Asn-Asn-Gly-Asp-Phe-Glu-Glu-Ile-Pro
	51 60
HV1	Glu-Glu-Tyr-Leu-Gln
HV2	Glu-Glu-Tyr-Leu-Gln
	61 65

(proteolytically cleaved) bovine β -thrombin (10% residual activity), vs. human β -thrombin (zero activity) [10], [11] and their differential binding behavior with bovine pancreatic trypsin inhibitor [12], [13]. These differences are demonstrated structurally in the ESR spectra (Figure 2) of *m*-V and *p*-V labelled human and bovine thrombins, respectively. Here the nitroxide is reporting interactions at about 10Å from the covalent phenylsulfonyl linkage (serine 195). We note that the bovine ESR spectra show less nitroxide mobility, i.e. stronger interactions between the nitroxide and the enzyme, as measured by their larger hyperfine extrema splittings $2T_{\parallel}$ (denoted by arrows). Some of these differences are attributed to a difference in flexibility in the β -insertion loop (residues 59-61), containing Trp 60D and the δ -insertion loop 145-150. In particular, the δ -loop contains a major substitution at residue 149E, from Lys in human to the (oppositely charged) Glu in bovine thrombin [7].

2 Interactions of Active Site Labeled Thrombins and Recombinant Hirudins and Hirudin Analogs

In order to address the kinetic results [2] with direct physical evidence, we examined the binding of intact recombinant hirudin HV2-Lys47, (Transgene, Strasbourg, France) and two C-terminal fragments, named 12-mer and 21-mer (Marion Merrell-Dow, Cincinnati, OH). Their respective sequences are shown below:

Figure 3 depicts ESR spectra for *m*-VII labeled bovine thrombin alone and complexed with 12-mer, 21-mer and HV2-Lys47 hirudin, respectively. Upon saturating with 12- or 21-mer essentially no changes were observed in $2T_{\parallel}$, within experimental accuracy. However, complexation with HV2-Lys47 resulted in a major immobilization of the piperidinyl nitroxide moiety, with only a slight amount residual motion. Presumably, the large hirudin molecule has sterically hindered nitroxide motion but could also contribute to structural changes which favor stronger hydrophobic interactions with the enzyme surface. In the case of *p*-V spin labeled human (data not shown) complexed with 12-mer or 21-mer, are observed label immobilization the $2T_{\parallel}$ changed from 49.5 to 60 Gauss. Then with HV2-Lys47; the *p*-V human thrombin complex was even more immobilized, $2T_{\parallel} = 63.3$ Gauss. On

the other hand, *p*-V labeled bovine thrombin showed changes only upon binding HV2-Lys47 as also found for *m*-VII bovine thrombin (Figure 6). If one compares human (not shown) vs. bovine *m*-VII thrombin alone, the larger $2T_{\parallel}$ for bovine (51.6 Gauss vs. human, 49.1 Gauss) exemplifies their subtle structural differences discussed earlier.

What are the structural explanations for the differences in sensitivity to binding of C-terminal hirudin fragments? The *p*-V label was found to reside in a binding locus on human thrombin that was sensitive to the binding of apolar ligands [15], while the *m*-VII label bound to a locus which was distinguished between human α - and γ -thrombins. Secondly, the *p*-V site is structurally linked to the binding of 12-mer and 21-mer to human thrombin, but has lost this linkage in the case of bovine thrombin. The major structural difference between the two species in hirudin C-terminal binding appears to be at Lys149E (human), which forms a salt bridge with Asp55 of HV2-Lys47, but is substituted by Glu149E in bovine thrombin. That is, one expects no interaction (in fact, repulsion) between Glu149E bovine and Asp55 of hirudin, the 12-mer or 21-mer C-terminal analogs. Consequently, it appears that the *p*-V label is either interacting directly with loop 145-150 or is perturbed as a result of binding interactions between hirudin analogs and human thrombin. Preliminary molecular graphics studies of spin labeled thrombin models revealed that the nitroxide could interact with either insertion loop (145-150, 59-61).

3 Distinguishing Between Hirudin Isoinhibitors

To date some hirudin isoinhibitors have been isolated from medicinal leeches, their relative amounts varying with geographic origin of the leech. The scheme below lists the primary sequences of two recombinant hirudin forms, HV1 and HV2-Lys47. These differ by eight residues which are indicated in bold. Upon examining whether the dynamic solution probes might be sensitive to the small spin labels hirudin sequence differences upon complexing various labeled-thrombins. Figure 4 depicts ESR spectra for HV1 and HV2-Lys47, respectively complexed with *m*-VII- and *p*-III- ϵ -labeled-thrombins, where the ϵ -form is proteolytically cleaved at

Figure 3 X-band ESR spectra of bovine *m*-VII- α -thrombin in the absence and presence of 12-mer ($\approx 100 \mu\text{M}$), 21-mer ($\approx 100 \mu\text{M}$), and HV2-Lys47 ($\approx 70 \mu\text{M}$). Thrombin concentration was $50\text{-}60 \mu\text{M}$. The arrows indicate the hyperfine extrema, the positions of the outermost peaks. Conditions were 0.75 M NaCl , 0.05 M Tris , $\text{pH } 6.5$, $20 \pm 2^\circ \text{ C}$. From [14] with permission.

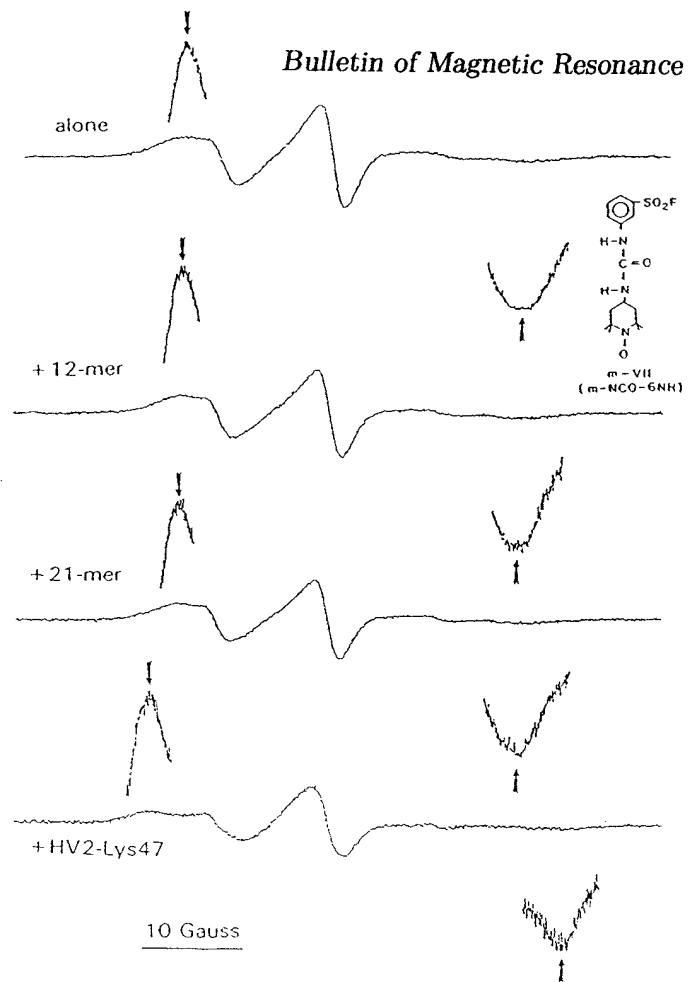
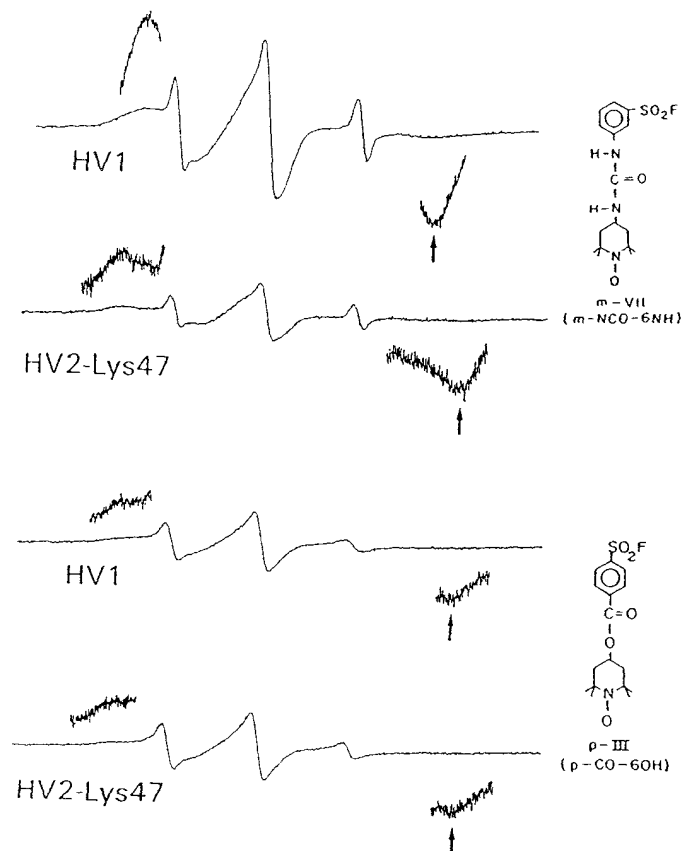


Figure 4 X-band ESR spectra of spin labeled human ϵ -thrombin ($50\text{-}60 \mu\text{M}$) complexed with HV1 ($\sim 70 \mu\text{M}$) and HV2-Lys47 ($\sim 70 \mu\text{M}$), respectively. The upper spectra are *m*-VII- ϵ -thrombin; the lower spectra are *p*-III- ϵ -thrombin. All spectra were measured at $\text{pH } 6.5$, 0.05 M Tris , 0.75 M NaCl , $20 \pm 2^\circ \text{ C}$. Protein concentration was typically $50\text{-}90 \mu\text{M}$. From [16] with permission.



149A. The differences in immobilization between HV2-Lys47 and HV1 are quite striking, comparing the hyperfine extrema $2T_{\parallel}$ (indicated by arrows). The larger splitting of HV2-Lys47 indicates a greater nitroxide immobilization vs. the HV1- complex.

The data obviously suggest that structural differences exist between the HV1 and HV2-Lys47-thrombin complexes. While these monitor the active site region, the changes may be elicited from a more distant site. Note that the larger $2T_{\parallel}$ is usually observed for HV2-Lys47:spin labeled thrombin complexes in most of these results suggesting that binding interactions with HV2-Lys47 result in a greater nitroxide immobilization than with HV1. Since these labels (p-III and m-VII) should occupy spatially distinct regions in thrombin [15], the differences can be localized to the phenylsulfonyl binding region rather than the locus occupied by the nitroxide ring. Another possibility is that HV2-Lys47 'blankets' the active site more, restricting the nitroxide rotation more severely. The results suggest that loop 145-150 (which contain both the ϵ - and ζ -thrombin cleavages), may interact differently with the two hirudin forms [17], [18]. Due to insertions both loops 145-150 and 70-80 contain 11 residues, while loop 59-61 contains 12. Examination of the crystallographic structure of HV2-Lys47:human α -thrombin complex shows that Ile 1 was principally involved in non-polar interactions at the

catalytic site [19]. We assume that in HV1 the substitution of a Val should make little difference. N-terminal residue 2 binds at the edge of the specificity pocket and does not appear to contribute to the overall binding. In the center of the hirudin sequence residues 31-36 were disordered and residue 53 was also found to have poorly defined electron density in the crystal [19].

There are only two residues which appear to be critical: Lys24, which is a hydrogen bonded (potentially) to thrombin through a water molecule (the substitution of Gln24 in HV1 should modify this interaction); and Glu49, which forms an ion pair with His51 of thrombin. In HV1, the substitution with Gln49 should disallow an ion pair. While residue 49 lies near the catalytic site, residue 24 resides nearer to thrombin loops 59-61 and 70-80. Presently, we cannot rule out one over the other as responsible for the spectral differences exhibited in Figure 4.

In summary, ESR spin labeling applications are extremely sensitive to long range conformational changes elicited in thrombin-anticoagulant interactions.

Acknowledgements

This research was supported in part by a grant from the USPHS (RR03126).

REFERENCES

- ¹Scheraga, H. A., Gibson, K., and Ni, F., (1992) **Thrombin: Structure and Function**, Berliner, L. J. (ed.), Plenum Publishing, New York, NY, pp. 63-85
- ²Stone, S. R., and Hofsteenge, J., (1986) *Biochem.* 25:4622-4628.
- ³Berliner, L. J., (1980) "Spectroscopy in Biochemistry, Vol. 2," Bell, J. E. (ed.), CRC Press, Boca Raton, Florida pp. 1-56.
- ⁴Nienaber, V. L., and Berliner L. J., (1991) *Thrombosis and Haemostasis* 65:40-45.
- ⁵Berliner, L. J. and Shen, Y. Y. L., (1977) *Biochem.* 16:4622-4626.
- ⁶Bode, W., Mayr, I., Baumann, U., Huber, R., Stone, S. R., and Hofsteenge, J., (1989) *EMBO. J.* 8:3467-3475.
- ⁷Bode, W., Huber, R., Rydel, T. J., and Tulinsky, A., (1992) **Thrombin: Structure and Function**, Berliner, L. J. (ed.), Plenum Publishing, New York, NY, pp 3-61.
- ⁸Berliner L. J., Birktoft, J. J., Miller, J. L., Musci, G., Scheffler, J. E., Shen Y. Y., and Sugawara, Y., (1986) *Annals N. Y. Acad. Sci.* 488:80-95.
- ⁹Sonder, S. A., and Fenton, J. W. II, (1983) *Thromb. Res.* 32:623-629.
- ¹⁰Lottenberg, R., Hall, J. A., Fenton, J. W., Jackson, C. M., (1982) *Thromb. Res.* 28:313-332.
- ¹¹Lundblad, R. L., Nesheim, M. E., Straight, D. L., Sailor, S., Bowie J., Jenzano, J. W., Robert, J. D., and Mann K. G., (1984) *J. Biol. Chem.* 259:6991-6995.

- ¹²Ascenzi P., Coletta M., Amiconi G., De Cristofaro R., Bolognes M., Guarneri M., and Menegatti E., (1988). *Biochim. Biophys. Acta* 956:156-161.
- ¹³Sugawara Y., Birktoft J.J. and Berliner L.J. (1986), *Sem. Thromb. Haem.* 12:209-212.
- ¹⁴Berliner, L. J., and Woodford, J. K. (1993) , **The Design of Synthetic Inhibitors of Thrombin** Claeson, G., Scully, M.F., Kakkar, V.V., Deadman, J. (eds.), Plenum Publ. Corp., New York, in press.
- ¹⁵Berliner, L. J., Bauer, R. S., Chang, T-L, Fenton, J. W. II, and Shen, Y. Y. L., (1981) *Biochem* 20:1831-1837.
- ¹⁶Rowand, J. K., and Berliner, L. J. (1992) *J. Prot. Chem.* 11:483-480.
- ¹⁷Brower, M. S., Walz, D. A., Garry, K. E., and Fenton, J. W. II, (1987) *Blood* 69:813-819.
- ¹⁸Brezniak, D. V., Brower, M. J., Witting, J. I., Walz, D. A., and Fenton, J. W. II, (1989) *Biochem.* 29:3536-3542.
- ¹⁹Rydel, T. J., and Tulinsky, A., (1991) *J. Mol. Biol.* 221:583-601

The NMR spectra of homonuclear two-spin systems under magic-angle and off-magic-angle spinning

Toshihito Nakai and Charles A. McDowell

Department of Chemistry, University of British Columbia,
2036 Main Mall, Vancouver, B.C., Canada, V6T 1Z1

1. Introduction

The solid-state NMR spectroscopy for dipolar-coupled spin systems may yield a variety of information on molecular structures and motions [1]. One notable point in comparison with isolated spin systems is that, without appealing to single crystal studies, the spectra of such systems using powdered samples (powder patterns) may give the (mutual) orientations of the principal axes of dipolar and chemical-shift tensors, in addition to the principal components of these tensors. Thus, because of their importance, the methods for analysing the powder patterns of such systems have been studied [2-4], and many applications were reported.

As is well known, one of the difficulties in the measurement of powder patterns for stationary samples is the reduction of spectral sensitivities or the time-consuming experiments, resulting from the large distribution of resonance frequencies. To overcome this drawback, the line narrowing due to sample spinning is generally effective. One approach to retrieve the tensor information from the spinning spectra is the simulation of the spinning sideband intensities measured under magic-angle spinning (MAS) [5,6]. The other approach is to obtain the scaled powder patterns under off-magic-angle spinning (OMAS) [7-10]. For isolated spin systems (e.g. ^{13}C natural abundance systems) or heteronuclear coupled systems (e.g. ^{13}C - ^1H coupled systems), the analysis of the spinning spectra is straightforward and so has often been demonstrated.

However, it is difficult to analyse the MAS or OMAS spectra for homonuclear spin

systems; the Hamiltonian dominating the systems, which depends on time due to the sample spinning, is not commutable with itself at different times (homogeneous Hamiltonian) [5], and therefore the time-evolution of the systems cannot be expressed in a closed form.

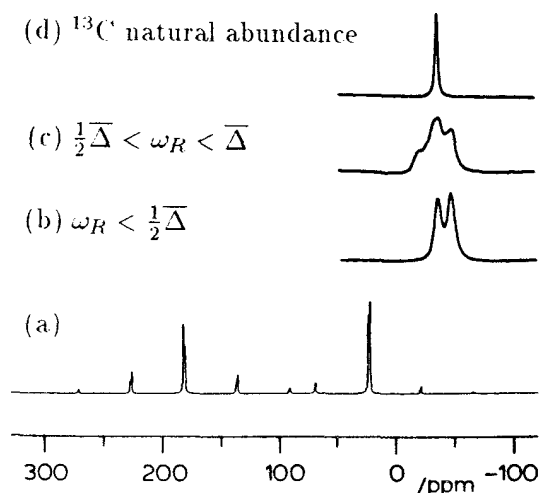
We recently described [11,12] the spinning spectra of the homonuclear two-spin systems successfully, using Floquet theory [13-16]. The Floquet theory has several advantages in comparison with the average Hamiltonian theory (AHT) [5,17] which has often been used: (i) it is not subject to the restriction for AHT which is valid only for spinning frequencies ω_R higher than the size of the total Hamiltonian; (ii) the calculation of the high-order perturbation corrections is easy and yields virtually exact spectra as far as the perturbation expansion converges; (iii) the theory can describe the states at other than multiples of cycle time of the systems (rotor spinning period), and consequently can be used to calculate the spinning sideband structures, while only the rotor synchronously-sampled spectra can be obtained from AHT.

In the present paper, we demonstrate how to determine the spin parameters for homonuclear two-spin systems from the MAS and OMAS spectra, using ^{13}C doubly-labeled sodium acetate $\text{Na}^{13}\text{CH}_3^{13}\text{COO}$ and palmitic acid $\text{CH}_3(\text{CH}_2)_{13}^{13}\text{CH}_2^{13}\text{COOH}$. Here, we restrict ourselves to the cases where the isotropic-shift difference of the two spins $\bar{\Delta}$ is large enough and does *not* satisfy the rotational resonance conditions, $\bar{\Delta} = n\omega_R$ [18-24]; the excluded cases can also be described by the Floquet theory and will be reported elsewhere.

2. MAS lineshapes and line positions

Figure 1 shows the MAS spectrum of ^{13}C doubly-labeled sodium acetate. The individual sidebands exhibit the doublets (Fig.1(b)), simply because the J coupling between two carbon nuclei characterizes the lineshapes. At the other spinning frequencies, however, the triplet-like lineshapes may unexpectedly appear (Fig.1(c)), suggesting that the origin of the "MAS lineshapes" [5] is not so simple. Also, the line positions, which may be defined as the centers of gravity of the lineshapes, may shift from the isotropic-shift positions observed for the ^{13}C natural abundance sample ("additional shifts") [20].

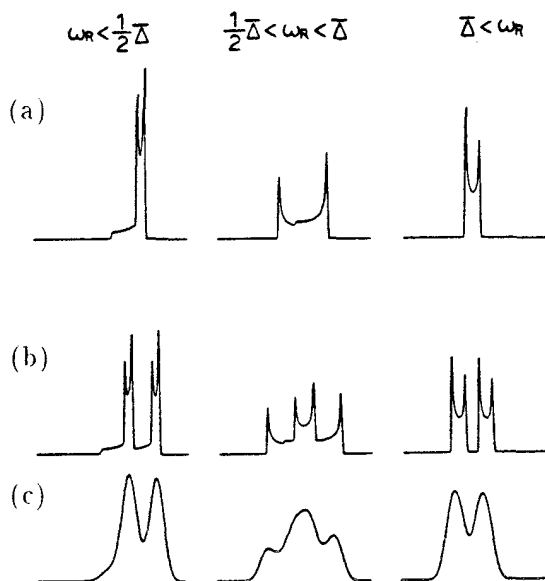
Fig.1



These features intrinsic to the spinning spectra for homonuclear two-spin systems can be reproduced by considering the second- or higher-order anisotropic interactions in the Floquet theory. In Fig.2 are illustrated the MAS lineshapes calculated to second order. The second-order anisotropies are not removed by MAS and thereby may cause the frequency distributions (Fig.2(a)). The distributions alter with the spinning frequencies, and the triplet-like lineshapes as well as the doublets can be reproduced, by taking into account the J splitting (Fig.2(b)) and line broadening (Fig.2(c)). The centers of gravity of the calculated lineshapes are gen-

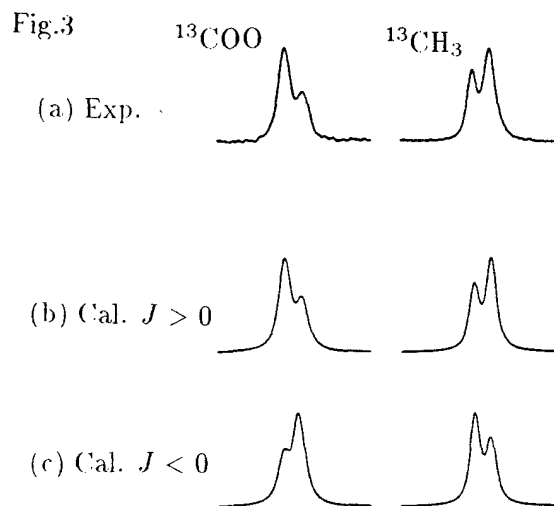
erally displaced from the isotropic-shift positions, similar to the experimental results. It is to be noted that, although the above second-order calculation describes the basic features of the spectra, the higher-order corrections should be calculated until the perturbation expansion converges, to reproduce the experimental spectra. The recurrence equations in the Floquet theory enable us to estimate the higher-order corrections efficiently [11].

Fig.2



In principle, if we can observe the fine structures in the experimental spectra, as can be seen in the spectra calculated without convolution shown in Fig.2(b), we can determine the various spin parameters by spectral simulation. The practical broadenings may, however, usually conceal such informative structures, and so it is extremely difficult to determine all the parameters only from the broadened lineshapes. Nevertheless, some parameters can easily be deduced. First of all, the MAS lineshapes observed at low spinning frequencies ($\omega_R < \frac{1}{2}\bar{\Delta}$) exhibit the J -split doublets, and the magnitudes of the J constants are immediately determined. Furthermore, the asymmetry in intensity of

the doublets may reflect the signs of J couplings (Fig.3); for sodium acetate, we determined $J_{CC} = +54$ Hz. Secondly, we found that the additional shifts are determined by the dipolar couplings as well as known parameters ω_R and Δ (it holds true strictly to second order and approximately to higher order). Therefore, by simulating the values of the additional shifts for various spinning frequencies, we determined the carbon-carbon distance in sodium acetate to be 1.55 Å.



3. MAS spinning sidebands

In analogy of the isolated spin systems and heteronuclear coupled spin systems, the analysis of the spinning sidebands is considered to be useful to obtain the information on the anisotropic interactions. In Fig.4 is illustrated the change of the spinning sidebands calculated for several orientations of the chemical-shift tensors. Obviously, the asymmetry in intensity of the doublets of the individual sidebands changes dramatically. We can therefore determine the spin parameters by simulating the lineshapes of the sidebands as well as their intensities. The experimental MAS sidebands and their simulation for sodium acetate are shown in Fig.5. As optimal parameters, we determined not only the tensor components but also the tensor orientations as depicted in Fig.6. For example, the least shielding direction of the

carboxyl carbon is almost parallel to the C-C direction, suggesting that the two C-O bonds are equivalent in this compound.

Fig.4

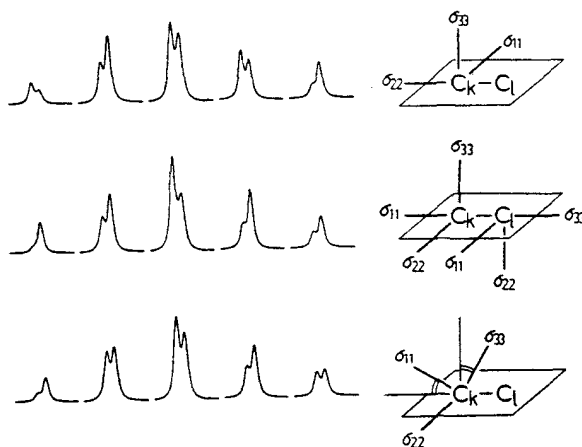


Fig.5

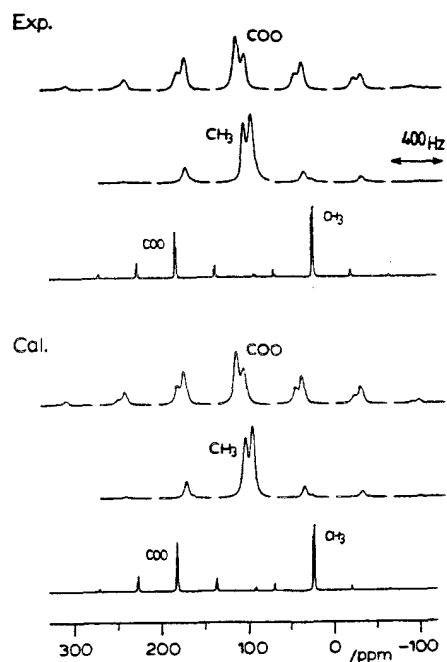
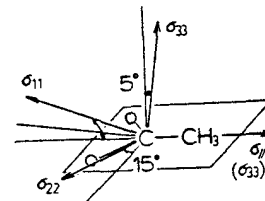


Fig.6

COO (255,210,105)
 CH_3 (34,34,7) ppm
 $r = 1.55 \text{ \AA}$
 $J = +54 \text{ Hz}$



4. OMAS scaled powder patterns

Another possibility for obtaining the spin parameters is the analysis of the scaled powder patterns observed under OMAS. In the OMAS spectra, we can detect the noticeable fine structures in spite of the practical broadenings, which smear out the MAS fine structures. The calculated OMAS spectra illustrated in Fig.7 show that these fine structures are sensitive to the spin parameters, and so we applied this strategy to palmitic acid. By reproducing the experimental OMAS spectra of this compound with calculation (Fig.8), we obtained various spin parameters as shown in Fig.9. Among them, the interesting point is that the least shielding direction of the carboxyl carbon is no longer parallel to the C-C direction, as in the case of sodium acetate. This is caused by the fact that the two C-O bond are not equivalent; namely, one is a single bond and the other is a double bond. In other words, the proton transfer along the hydrogen bonds in the dimers is not so fast as to equalize the two C-O bonds at room temperature at which the experiments were performed.

Fig.7

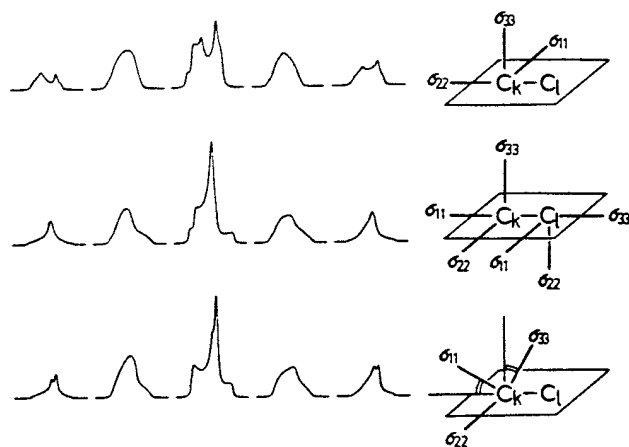


Fig.8

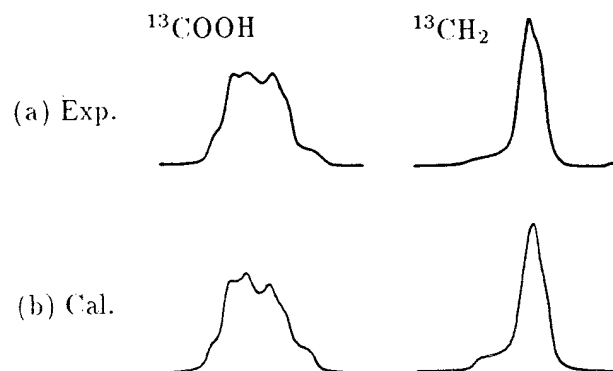
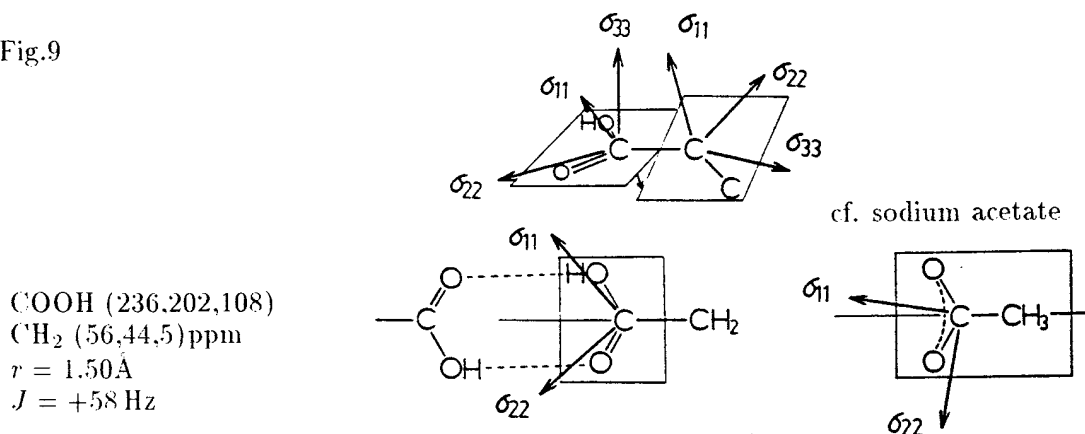


Fig.9



5. Conclusion

As described above, the sample-spinning techniques for homonuclear two-spin systems are effective to enhance the spectral sensitivities, and do not sacrifice the structural information on the systems at the cost of line narrowing as well as for isolated spin systems or heteronuclear coupled spin systems. Theoretical difficulties in treating the homogeneous Hamiltonian for homonuclear systems under sample spinning can be overcome using the Floquet theory. The theory allows us to simulate the notable spectral features, such as the unique lineshapes and spinning sideband structures, determining the spin parameters for sodium acetate and palmitic acid.

Acknowledgements

We thank the Natural Sciences and Engineering Research Council (NSERC) of Canada for research grants to C.A.McD. Moreover, T.N. wishes to express his gratitude to NSERC for the award of an International Postdoctoral Fellowship and to the Izaak Walton Killam Foundation for the award of a postdoctoral fellowship.

References

- [1]. C.A.Fyfe, "Solid State NMR for Chemists", C.F.C.Press, Guelph, (1983).
- [2]. W.P.Power and R.E.Wasylishen, *Ann.Rept.NMR Spectr.*, **23**, 1 (1991).
- [3]. K.W.Zilm and D.M.Grant, *J.Am.Chem.Soc.*, **103**, 2913 (1981).
- [4]. M.Linder, A.Höhener, and R.R.Ernst, *J.Chem.Phys.*, **73**, 4959 (1980).
- [5]. M.M.Maricq and J.S.Waugh, *J.Chem.Phys.*, **70**, 3300 (1979).
- [6]. J.Herzfeld and A.E.Berger, *J.Chem.Phys.*, **73**, 6201 (1980).
- [7]. E.O.Stejskal, J.Schaefer, and R.A.McKay, *J.Magn.Reson.*, **25**, 569 (1977).
- [8]. R.E.Taylor, P.G.Pembleton, L.M.Ryan, and B.C.Gerstein, *J.Chem.Phys.*, **71**, 4541 (1979).
- [9]. H.Miura, T.Terao, and A.Saika, *J.Chem.Phys.*, **85**, 2458 (1986).
- [10]. N.K.Sethi, D.M.Grant, and R.J.Pugmire, *J.Magn.Reson.*, **71**, 476 (1987).
- [11]. T.Nakai and C.A.McDowell, *J.Chem.Phys.*, **96**, 3452 (1992).
- [12]. T.Nakai and C.A.McDowell, *Mol.Phys.*, **77**, 569 (1992).
- [13]. J.H.Shirley, *Phys.Rev.*, **B138**, 979 (1965).
- [14]. D.R.Dion and J.O.Hirschfelder, *Adv.Chem.Phys.*, **35**, 265 (1976).
- [15]. Y.Zur, M.H.Levitt, and S.Vega, *J.Chem.Phys.*, **78**, 5293 (1983).
- [16]. S.Vega, E.T.Olejniczak, and R.G.Griffin, *J.Chem.Phys.*, **80**, 4832 (1984).
- [17]. U.Haeberlen and J.S.Waugh, *Phys.Rev.*, **175**, 453 (1968).
- [18]. E.R.Andrew, E.Bradbury, R.G.Eades, and V.T.Winn, *Phys.Lett.*, **4**, 99 (1963).
- [19]. E.R.Andrew, S.Clough, L.F.Farnell, T.D.Glendhill, and I.Roberts, *Phys.Lett.*, **21**, 505 (1966).
- [20]. B.H.Meier and W.L.Earl, *J.Am.Chem.Soc.*, **109**, 7937 (1987).
- [21]. D.P.Raleigh, G.S.Harbison, T.G.Neiss, J.E.Roberts, and R.G.Griffin, *Chem.Phys.Lett.*, **138**, 285 (1987).
- [22]. D.P.Raleigh, M.H.Levitt, and R.G.Griffin, *Chem.Phys.Lett.*, **146**, 71 (1988).
- [23]. Z.-H.Gan and D.M.Grant, *Mol.Phys.*, **67**, 1419 (1989).
- [24]. A.Kubo and C.A.McDowell, *J.Chem.Phys.*, **93**, 7156 (1990).

Coreflood Experiments on Casper Sandstone: Using Magnetic Resonance Imaging to Measure Flow Velocities

M. Robinson Merrill

Chemical Engineering Department
University of Wyoming
P. O. Box 3295
Laramie, Wyoming 82071-3295

INTRODUCTION

In conventional coreflood experiments, the displacement efficiency is estimated by measuring oil recovered as a function of injection volume. However, such experiments give no indication of how much of the core is actually contacted by the displacement fluid. To better understand the flow processes occurring within the rock, it is desirable to get a three-dimensional map of the flow velocities during the injection process. Regions showing no flow velocity correspond to regions which will not be contacted by the displacement fluid.

In this study, magnetic resonance imaging (MRI) is used to obtain fluid velocities in Casper sandstone during water injection into a water-filled core. A 2-D image of the interstitial water velocity is obtained in arbitrary cross-sections, with pixel sizes on the order of 1mm square.

Casper sandstone has a porosity of 16-21% and a permeability of about 77-88md. It is homogeneous on a large scale, although it contains layers of varying porosity and permeability which are apparent in the images. The core was cut so that the bulk flow would be roughly parallel to the layers. The presence of layers in the core suggests that fluid displacement experiments will show preferential channeling into high permeability layers.

The local velocity and porosity data for the core are used to obtain a graphical correlation between velocity and porosity. Since velocity is proportional to permeability, such a graph can give an empirical representation of how fluid channels within a heterogeneous core. The results show that as local porosity increases, the local flow velocity increases. Thus, higher porosity regions of the core are better contacted by the displacement fluid.

Using MRI to measure fluid velocities inside cores is extremely difficult. Because of high mineral content and high surface-to-volume ratios inside the cores, the T_2 relaxation constant is quite short (approximately 6 msec for Casper sandstone). To measure velocities accurately, pulse sequences with very short spin-echo times are required. In addition, the signal-to-noise ratio for core imaging experiments is only on the order of 10:1. Unless the flow rate is quite high inside the core, the effect of the signal-to-noise ratio on the accuracy of the velocity measurement can be catastrophic. Because of these conditions, long experiments are required to get adequate signal-to-noise by signal averaging. In this study, a modified 3D FT pulse sequence is used to obtain the shortest echo times possible, and yet have a sufficiently long flow encode time to measure the slow velocities observed in coreflood experiments.

Only axial flow was measured in this work. However, by varying the direction of the flow encode gradients, the same pulse sequence can be used to measure the other two orthogonal flow components, and thus obtain the entire velocity vector for each point in the core.

EXPERIMENTAL PROCEDURE

A sample of Casper sandstone was used in these experiments. It had a diameter of 62.5 mm, a length of 116 mm, an average porosity of 21%, and an estimated permeability of about 80 md. It was cored with its axis approximately parallel to the bedding planes in the sample.

A modified Hassler-type coreholder was used in the flow experiments. This coreholder was specially designed for use in the imager and had no metal parts which might interfere with the RF signals or cause inhomogeneities in the magnetic field. A diagram of the coreholder is shown

in Figure 1. It is composed of a 3 inch PVC pipe with two plexiglass end caps. The caps are held on by eight Delrin rods with nylon washers and nuts. A tube of rubber is placed inside the PVC pipe and wrapped around the ends. A vacuum is used to pull the rubber against the PVC pipe. The core and Lucite spacers are placed inside the sleeve, and the end caps are screwed on. The vacuum is removed, and nitrogen gas is introduced into the annulus between the rubber and the PVC. It is this overburden pressure of nitrogen (at about 120 psi) which is used to prevent bypassing of the fluid around the perimeter of the core. It is estimated that such a coreholder can withstand pressures up to about 150 psi.

The core was vacuum saturated before being placed inside the coreholder. First, the dry, clean core was placed in a vacuum chamber for 24 hours to remove all the air from the pore spaces. Then, while still under vacuum, a 1% KCl solution was introduced into the vacuum chamber until it covered the core. The core and KCl solution were left in the vacuum for four hours, and then they were returned to atmospheric pressure.

Following vacuum saturation of the core, it was placed in the Hassler coreholder. The KCl solution was then injected into the core for twelve hours, to ensure that the core was completely saturated prior to imaging. A flow rate of 2321 cm³/hr was used.

A three-dimensional Fourier transform (3D FT) pulse sequence was modified to acquire the MRI data. A diagram of the sequence is shown in Figure 2. It employs a conventional three-dimensional spin-echo sequence, with the addition of flow encode gradients (GF in Figure 2) for measurement of the flow velocities.

The benefit of using a 3D FT pulse sequence is that it uses a second phase encode gradient for slice selection, instead of a slice selective gradient. Because this gradient can be applied simultaneously with the other phase encode gradient and a hard 90° pulse can be used, the length of the echo time is minimized.

The flow encode gradient lobes are positioned on each side of the 180° pulse, thus maximizing the flow encode time while minimizing the echo time. Such a configuration requires a very accurate 180° pulse, so that the total area of the flow encode gradients is zero. The parameters for the velocity measurements are shown in Table 1.

For the measurement of the porosities, the pulse sequence shown in Figure 2 was used, with the flow encode gradients set to zero. The values of the other parameters are shown in Table 2.

THEORY

Porosity Measurements

The magnitude of the signal obtained using a 3D FT pulse sequence is directly proportional to the amount of water contained in the image voxel. The values of the porosity in each voxel were calculated by dividing the magnitude of the signal by a constant, such that the average porosity for the core was equal to the value of 21% measured in the lab by weighing. This method is valid only if the echo time is small enough so that signal is not lost due to T₂ relaxation. It assumes that there is only a single T₂ relaxation time for the entire core, which may not always be valid. It also assumes a fairly homogeneous core, so that a subregion of the porosity is equal to the porosity of the entire core sample.

Velocity Measurements

The velocity of the flow is measured in terms of the phase of the transverse spin magnetization. The phase shift (ϕ) in a voxel due to fluid moving with a constant velocity component V_i in the i coordinate direction is given by Hahn's equation¹,

$$\phi = \gamma m_1 V_i, \quad (1)$$

where m_1 is the first moment of the gradient,

$$m_1 = \int t G_i(t) dt. \quad (2)$$

For the bipolar, trapezoidal gradients used in these experiments, Eq. (1) simplifies to

$$\phi = \gamma G_i \Delta (\delta + r_t) V_i, \quad (3)$$

where Δ is the time separating the gradient pulses, r_t is the ramp time of the gradient pulse, δ is the duration of the pulse, and G_i is the magnitude of the pulse (see Figure 2).

Differentiating Eq. (3) with respect to G_i , we obtain

$$(d\phi/dG_i) = \gamma \Delta (\delta + r_t) V_i. \quad (4)$$

Therefore, the velocity in a voxel is directly proportional to the slope of the line resulting from a graph of ϕ versus G_i . In our experiments, we determined this slope from the observed phase at three different values of G_i : -9.8 G/cm, 0 G/cm, and +9.8 G/cm. Using the linear regression to obtain the velocity should be more accurate than measuring the phase shift at only one value of the gradient, since it helps to cancel out noise effects.

Unfortunately, one cannot simply image the flow and

obtain the phase shift directly from the data. Because of eddy currents and other effects, one must have data to reference with the given phase. For that reason, two data sets were obtained for every value of the flow encode gradient: one with no flow going through the core, and the second with the flow turned on. The phase difference between the two images was used as ϕ in Eq. (4).

It is possible to obtain all three components of the velocity vector by performing three experiments using three orthogonal gradients to flow encode the x-, y-, and z-directional flow. However, only z-directional (axial) flow was measured in this study.

EXPERIMENTAL RESULTS

Figure 3 shows qualitative images of the porosity and positive and negative flow velocities for eight image slices through the Casper sandstone core. The image slices are shown perpendicular to the direction of flow.

The images of the porosity show evidence of the bedding planes in the core, as seen by the variations in the grey-scale of the image. If we make a frequency distribution of the porosity for the eight slices (porosity distribution), we get the graph shown in Figure 4. It indicates that the porosity does not have a normal distribution, but can be modeled very nicely using a bimodal distribution, where 67% of the core has an average porosity of 18.9%, and 33% of the core has an average porosity of 24.7%. It is believed that the two values of the porosity correspond to two different types of bedding planes in the core.

The flow images indicate that the bulk of the flow is in the positive direction, with some negative flow apparent only at the edges of the core (which are believed to be caused by noise in the data and/or bypassing of the fluid around the perimeter of the core). The flow in the positive direction appears to be fairly uniform.

For each value of the porosity (rounded to the nearest whole number), the velocity was determined from the MRI data. A running sum of the velocities was kept, and then the average velocity was calculated by dividing the sum of the velocities by the number of points at a particular value of the porosity.

The data obtained from this calculation are shown in Figure 5. In this figure, a graph of the average velocity versus porosity is superimposed on the porosity distribution. The data indicate that as the local porosity increases, the average velocity through the voxel also increases. This supports the assumption that as porosity increases, permeability also increases. An empirical equation relating velocity and porosity could be developed from this data and used in

coreflood simulation programs. A straight line fit to the data (ignoring points where the porosity distribution shows that very few values were obtained) gives the relationship,

$$V = 0.013862 + 0.017786 \phi \dots \dots (4)$$

where V is the velocity in cm/sec and ϕ is the porosity as pore volume percent. The fit is shown graphically in Figure 5.

Figure 6 shows a histogram of the velocities for the core (velocity distribution). A Gaussian distribution is superimposed on the data. The distribution appears to be fairly normal, and indicates an average velocity of 0.018 cm/sec through the core. This number is much smaller than the average interstitial velocity calculated using the flow rate of 2321 cm³/hr (which gives a velocity of 0.10 cm/sec). The most likely explanation is that bypassing of the fluid occurred in a thin film around the outside of the core. This is possible, because the overburden pressure differential on the rubber sleeve was only about 10 psi (0.069 MPa). It is recommended that a higher overburden pressure be used in future experiments.

CONCLUSIONS

1. Measurements of local flow velocities and local porosities have been made on a sample of Casper sandstone. Qualitative images of the porosities show evidence of bedding planes in the core. A bimodal fit to the porosity distribution indicates two types of layers in the core, one with an average porosity of 18.9%, and one with an average porosity of 24.7%.
2. The images of the velocity show that the bulk of the flow is in the same direction as the applied pressure gradient, with a small number of points at the edge of the core having an apparent velocity in the opposite direction.
3. A velocity distribution has been plotted for the core. The velocity distribution has a Gaussian shape.
4. The relationship between average velocity and porosity has been presented graphically and indicates that local velocity increases with an increase in local porosity. A straight line can be used to obtain an empirical relationship between average velocity and porosity in this core sample.
5. A higher overburden pressure is recommended to prevent bypassing of the fluid around the outside of the core.

NOMENCLATURE

- G_i = Gradient applied in the i coordinate direction
- m_1 = First moment of the flow gradient
- r_t = Gradient ramp time
- t = Time
- V = Velocity
- V_i = Velocity in the i coordinate direction
- γ = Gyromagnetic ratio (4260 Hz/G for ^1H)
- δ = Flow encode gradient duration
- Δ = Time separating flow encode pulses
- ϕ = Phase shift in a voxel due to flow
- \emptyset = Porosity

ACKNOWLEDGEMENT

The authors would like to thank Dominic Palese for building the coreholder used in the experiments.

REFERENCES

1. Hahn, E. L.: "Detection of sea-water motion by nuclear precession," *J. Geophys. Res.* (1960) 65, 776-777.

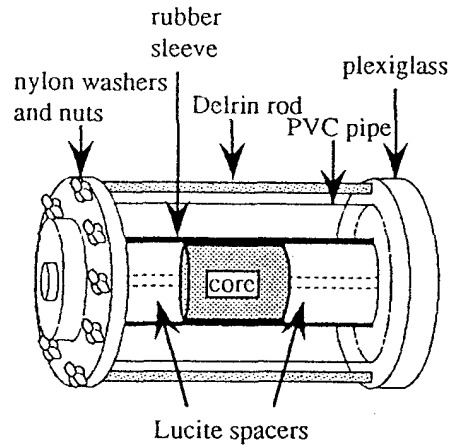


Figure 1
Hassler Core Holder

Table 1
Flow Imaging Parameters

	Velocity	Porosity
Number of averages	32	8
Recycle time (sec)	0.40	2.0
Number of slices	16	16
Axial field of view (mm)	128	128
Image field of view (mm)	64	64
Image resolution	64	64
Echo time (msec)	15	1.5
Flow gradient (G/cm)	-9.8, 0, +9.8	0
δ (msec)	6.477	0
r_t (msec)	0.175	0.175
Δ (msec)	7.025	0

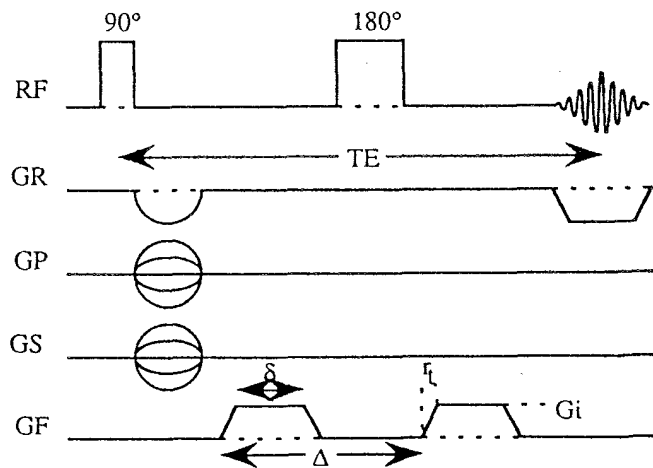


Figure 2
3DFT Flow Pulse Sequence

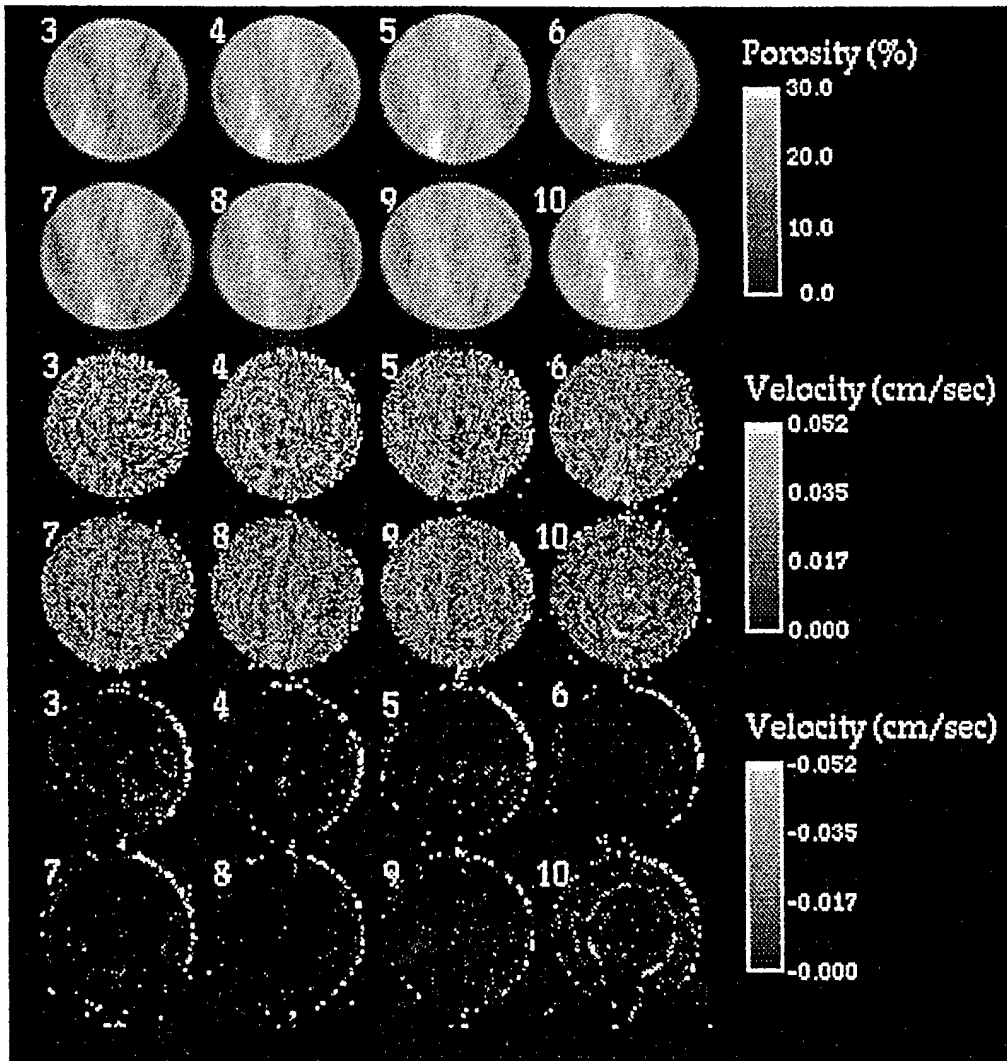


Figure 3

Casper Sandstone Porosity and Flow Images

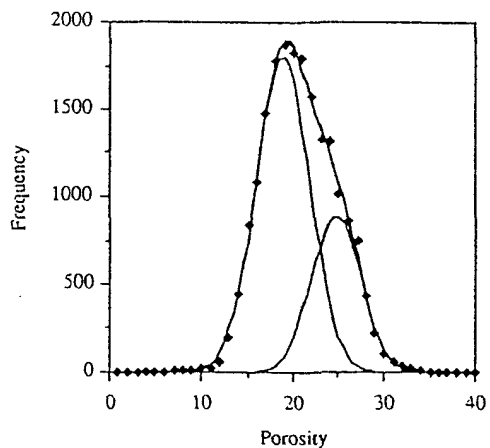


Figure 4
Bimodal Frequency Distribution of Porosity for Casper Sandstone

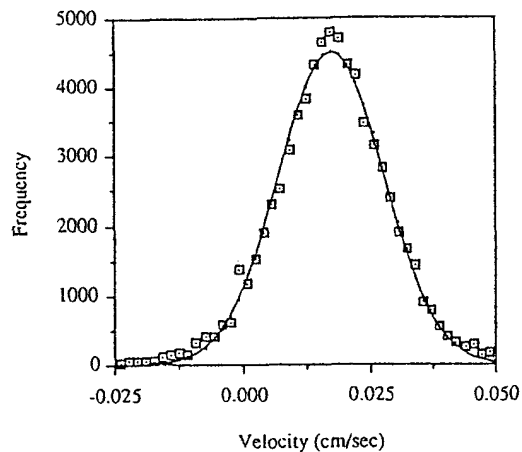


Figure 6
Velocity Distribution for Casper Sandstone

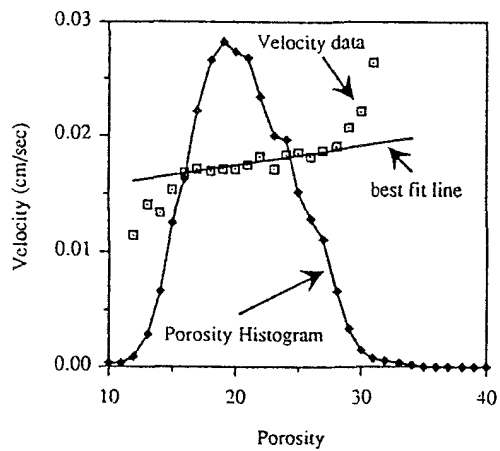


Figure 5
Variation of Average Velocity with Porosity

NMR Imaging of Solid Polymers

D. G. Cory, and W. E. Maas

Bruker Instruments, Inc.
19 Fortune Drive
Billerica, MA 01821, USA

1 Introduction

NMR imaging is being extended to the exploration of solid state samples with the intention of exploring spatial characteristics on the sub 100 μm scale (1-6). Some questions of interest are the processing and aging properties of synthetic polymers and composites (7-9), the spatial variation in chemical composition of natural composites (such as coal (10)), and the spatially dependent chemistry of reaction beds and diffusing systems (11). Although compared to other imaging approaches the available resolution is limited, there is a wide range of chemical and physical contrast mechanisms that are available including the possibility of introducing chemically specific spin labels. These allow studies that are not possible by other imaging methods.

For sensitivity reasons, ^1H NMR has been the main focus of solid state imaging studies, although ^{13}C (12-14), ^2H (8), ^{19}F (15,16), ^{27}Al (17, 18), ^{29}Si (19), and ^{11}B (20) have also been explored. These other nuclei allow an even wider range of contrasts to be built into the imaging experiment, but the main motivation is still to obtaining higher resolution images, and contrast has taken a back seat to sensitivity.

The major impediment to obtaining

NMR images of solid samples is that the natural line width is large (up to 50,000 Hz for rigid proton-rich solids) and so to resolve two adjacent volume elements the gradient induced spread in frequency across a single voxel must be greater than this line width,

$$\text{resolution} = \text{line width}/\text{gradient strength}.$$

Naturally, as the gradient is increased so too is the frequency spread of the image and therefore the bandwidth of the receiver must also be increased. This results in an increase in noise and leads to the conclusion that the time to acquire an image is directly proportional to the NMR line width of the sample.

The approaches to NMR imaging of solids fall into two well defined classes: those that rely upon large magnetic field gradients for resolution (21) while accepting a loss in sensitivity; and those that attempt to reduce the NMR line width to gain both sensitivity and resolution. Since the solid state NMR line width is of the order of 5,000 times broader than the liquid state line width, there is a real advantage to employing line-narrowing for solid state imaging. These arguments apply directly only to the NMR line width during acquisition, and phase encoding schemes can employ extremely large gradients with no loss in sensitivity provided that the gradient is switched off

on a time scale short compared to the life time of the FID (18).

2 Line-Narrowing Approaches to Solid State Imaging

In general the narrowest possible NMR resonance is desired to achieve the highest resolution and sensitivity. At the same time the line width should be uniform throughout the sample to avoid image distortions. Conceptually then the goal is to reduce the NMR resonance to a delta function and therefore to average all internal Hamiltonians to zero. This averaging can be accomplished in multiple-steps as with the combination of MAS (6,22,23) and multiple-pulse methods (24), the combination of MREV-8 and Carr-Purcell cycles (25, 26), or the combination of magic angle rotation in spin space and Carr-Purcell cycles in the magic angle rotating frame (27); or the averaging can be accomplished all at once with what are termed time-suspension cycles. Time-suspension cycles average all time independent internal Hamiltonians simultaneously to zero (28, 29). All of these approaches work to some extent and the particular choice of a line-narrowing scheme is not critical. Here we discuss a particular form of time-suspension cycle that has been shown to give excellent line narrowing with a wide range of materials (29) and is at the same time very forgiving of imperfections in the experimental set-up.

The gradient Hamiltonian is a linear I_z interaction and if the gradient is applied continuously, it is indistinguishable from other I_z interactions (such as chemical and susceptibility shifts). Therefore, when using a time-suspension cycle the gradient must be applied as a time dependent interaction to preserve a non-zero gradient averaged Hamiltonian.

There are many approaches that can be taken to give a time dependence to the gradient, including constant time experiments (30), oscillating gradients (31) and pulsed gradients (32). Ignoring the technical difficulties or benefits of one method over another, the important consideration is to control the gradient modulation such that the gradient does not interfere with the line-narrowing efficiency of the coherent averaging scheme (28,33). Pulsed gradients offer the greatest flexibility in placement, and are essential for gradient decoupling in the phase encoding domain.

3 Gradient Decoupling

In an over-simplified argument, the gradient can be thought of as a spatially increasing resonance offset. During a multiple-pulse experiment any offset leads to phase evolution between RF pulses, so the effective phase differences between sequential RF pulses is a function of the resonance offset. Most multiple-pulse experiments are designed to work on resonance and by forcing them off resonance these extra phase shifts reduce the extent to which the undesired interactions are refocussed.

Keeping to this simple picture, recall that the gradient is an I_z operator, so if the gradient is applied only in I_z toggling frame windows, then to zero-order the gradient can not influence the line-narrowing efficiency of the multiple-pulse cycle. The toggling frame windows are intervals between RF pulses in a reference frame that transforms with the RF pulses, and the conclusion follows since the dynamics from two interactions that commute are purely additive. To decouple the gradient to higher order, the gradient pulses are separated by multiple-pulse subcycles whose overall

propagators are ± 1 so that the gradient propagator and the entire sub-cycle propagator still commute (33).

Since the longest windows of the time-suspension multiple-pulse cycle are generally about 5-10 μs , this demands that the gradient be applied as very short pulses (32), and the technology for this is known (34). Also, since the gradient can be turned on and off during any single window of a pulse-cycle, there is no point in applying the gradient in a window where its effect will not accumulate, and so the gradient scaling factor is simply given by its duty cycle, and the effective field direction is along the z axis.

4 Time Sequenced Second Averaging

Time suspension cycles average all internal Hamiltonians and so in the absence of a pulsed gradient, the spins experience no net evolution. However, even though the spins are toggled through a complex trajectory, the final spin state is very sensitive to residual interactions (29) which generally arise

from experimental imperfections. It is useful to compare time-suspension cycles and multiple-pulse spin locking. In multiple-pulse spin locking, all internal Hamiltonians can also be averaged, but there exists an effective field about which a coherent evolution takes place and as long as this effective field is stronger than the Hamiltonians to be averaged, they do not contribute to the overall spin dynamics. With a time suspension cycle there is no effective (or dominant) field and every small interaction with a non-zero average contributes to the spin dynamics. These extra terms originate from a variety of sources such as pulse imperfections and RF coil imperfections, and they lead to a residual line broadening. The presence of a pulsed gradient removes the broadening through a process of second averaging (35). In effect, the gradient introduces an effective field, so that interactions that are perpendicular to the gradient effective field are averaged to zero, while the parallel portions add coherently to the gradient evolution but are normally sufficiently small as to be negligible. The difficulty arises since the gradient passes through zero and hence locally the line is once again broadened.

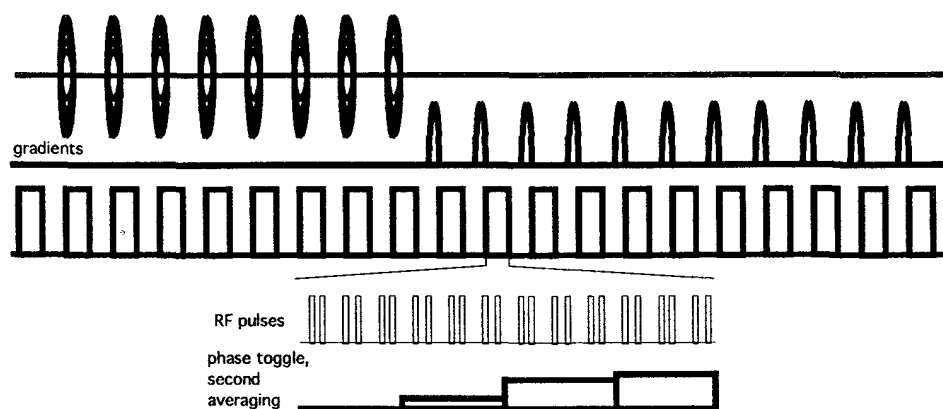


Figure 1. Schematic pulse sequence for NMR imaging of solids showing the pulsed gradients along with the multiple-pulse line-narrowing cycle and the RF phase shifts that are used for second averaging.

This local broadening can be removed by adding an additional interaction that is along the gradient direction and hence adds to it. If this second averaging is performed simultaneously with the gradient pulses the position of lower resolution is merely shifted in the image and little has been accomplished. A preferred approach is to apply the second averaging interaction in separate windows so that the error terms are always modulated regardless of the relative size of the second averaging interaction and the gradient interaction. This is called time sequenced second averaging. The averaging should be uniform throughout the image and so it is convenient to introduce this by a phase shift of the RF, or by a systematic variation in the RF pulse lengths. Figure 1 shows a pulse sequence which combines all of the ideas that have been discussed above.

5 Results and Discussions

The image in Figure 2 was acquired by a 2-D Fourier imaging augmentation of the scheme that is outlined in Figure 1 on a Bruker Instruments, Inc. 400 MHz AMX spectrometer with a Solidscope™ accessory. The sample is a poly(methylmethacrylate) phantom with the geometry shown in the figure 3. The gradient pulses were 5 μs long, the 90° pulse length was 1.8 μs and the shortest time between RF pulses was 1.7 μs (corresponding to a long window of 5.2 μs). The second averaging phase shift was 7.5°. The image is a 64 x 64 pixel reconstruction, yielding an in-plane resolution of just under 100 μm , and was recorded in approximately 30 min.

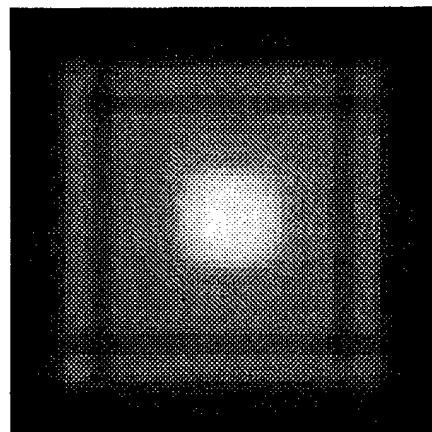


Figure 2. The 2-D Fourier image of the poly(methylmethacrylate) phantom shown in figure 3.

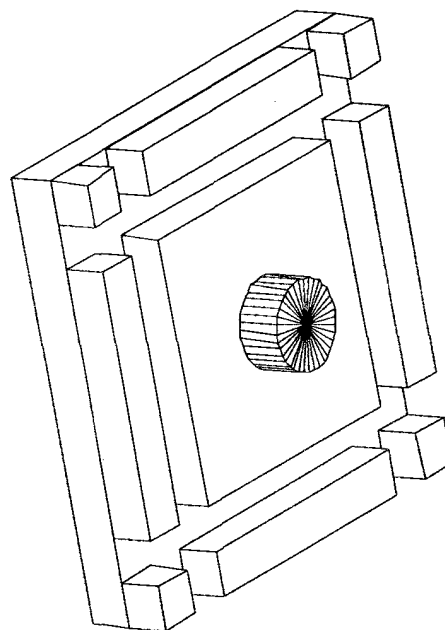


Figure 3 A schematic representation of the poly(methylmethacrylate) phantom.

6 Conclusions

High resolution NMR images of solid samples can be obtained using multiple-pulse line-narrowing techniques. For the

best results in terms of resolution and sensitivity, time-suspension cycles should be employed in combination with pulsed gradients suitably decoupled from the multiple-pulse cycle. Time sequenced second averaging is useful to avoid residual distortions associated with weak errors in the method. Taken together full three dimensional images can be obtained of common synthetic polymers.

7 References

1. D. G. Cory, Annual Reports on NMR Spectroscopy, 1992, **24**, 87.
2. P. Jezard, J. J. Attard, T. A. Carpenter, and L. D. Hall, Prog. NMR Spectro., 1991, **23**, 1.
3. J. B. Miller, D. G. Cory, and A. N. Garroway, Phil. Trans. R. Soc. A, 1990, **333**, 413.
4. J. B. Miller, Trends in Anal. Chem., 1991, **10**, 59.
5. J. M. Listrud, S. W. Sinton, and G. P. Drobny, Anal. Chem. 1989, **61**, 23A.
6. W. S. Veeman, and D. G. Cory, Adv. Magn. Reson., 1989, **13**, 43.
7. D. G. Cory, J. C. de Boer, and W. S. Veeman, Macromol., 1989, **22**, 1618.
8. E. Günther, B. Blümich, and H. W. Spiess, Mol. Phys., 1990, **71**, 477.
9. P. Blümler, and B. Blümich, Macromol., 1991, **24**, 2183.
10. S. L. Dieckman, P. Rizo, N. Gopalsami, J. P. Heesch, and R. E. Botto, J. Am. Chem. Soc., 1992, **114**, 2717
11. L. G. Butler, D. G. Cory, K. M. Dooley, J. B. Miller, and A. N. Garroway, J. Am. Chem. Soc., 1992, **114**, 125.
12. D. G. Cory, and W. S. Veeman, J. Phys. E: Sci. Instrum., 1989, **22**, 180.
13. N. M. Szeverenyi, and G. E. Maciel, J. Magn. Reson., 1984, **60**, 460.
14. C. G. Fry, A. G. Lind, M. F. Davis, D. W. Duff, and G. E. Maciel, J. Magn. Reson., 1989, **83**, 656.
15. P. J. McDonald, and P. F. Tokarczuk, J. Phys. E., 1989, **22**, 948.
16. J. H. Strange, Phil. Trans. R. Soc. A, 1990, **333**, 427.
17. S. W. Sinton, J. H. Iwamly, B. Ewing, and G. P. Drobny, Spectroscopy, 1991, **6**, 3.
18. M. S. Conradi, J. Magn. Reson., 1991, **93**, 419.
19. J. R. Moore, L. Garrido, and J. L. Ackerman, Ceram. Eng. Sci. Proc., 1990, **90**, 370.
20. P. Bendel, M. Davis, E. Berman, G. W. Kabalka, J. Magn. Reson., 1990, **88**, 369.
21. A. A. Samoilenko, and K. Zick, Bruker Report, 1990, (1), 41.
22. D. G. Cory, J. W. M. van Os, and W. S. Veeman, J. Magn. Reson., 1988, **76**, 543.
23. D. G. Cory, A. M. Reichwein, J. W. M. van Os, and W. S. Veeman, Chem. Phys. Lett., 1988, **143**, 467.
24. G. C. Chingas, J. B. Miller, A. N. Garroway, J. Magn. Reson., 1986, **66**, 530.
25. J. B. Miller, and A. N. Garroway, J. Magn. Reson., 1989, **82**, 529.
26. J. B. Miller, and A. N. Garroway, J. Magn. Reson., 1986, **67**, 575.
27. F. De Luca, B. C. De Simone, N. Luger, B. Maraviglia, and C. Nuccetelli, J. Magn. Reson., 1990, **90**, 124.
28. D. G. Cory, J. B. Miller, R. Turner, and A. N. Garroway, Mol. Phys., 1990, **70**, 331.
29. D. G. Cory, A. N. Garroway, and J. B. Miller, J. Magn. Reson. 1990, **87**, 202.
30. S. Emid and J. H. N. Creyden, Physica 1985, **125B**, 81.
31. P. J. McDonald, J. J. Attard, and D. J. Taylor, J. Magn. Reson., 1987, **72**, 224.
32. J. B. Miller, D. G. Cory, and A. N. Garroway, Chem. Phys. Lett., 1989, **164**, 1.
33. D. G. Cory, Proceedings of the 1st International Conference on NMR Microscopy (in press).
34. M. Conradi, A. N. Garroway, D. G. Cory, and J. B. Miller, J. Magn. Reson., 1991, **94**, 370.
35. A. Pines and J. S. Waugh, J. Magn. Reson., 1975, **8**, 50.

BIOCHEMICAL AND BIOPHYSICAL EFFECTS OF DEXAMETHASONE ON HUMAN LYMPHOBLASTOID CELL LINES, STUDIED BY ^{31}P AND ^1H NMR SPECTROSCOPY AND FLUORIMETRY

R. Ricciolini[§], A. Miccheli^{*}, E. Piccolella[#], A. Tomassini^{*}, C. Manetti^{*},
M.E. Di Cocco^{*} and F. Conti^{*}.

[§] Institute for Research on Senescence - Pomezia, Italy

^{*} Dept. of Chemistry - University "La Sapienza" - Rome, Italy

[#] Dept. of Immunology - University of "Tuscia" - Viterbo, Italy

1 Introduction

Recently has been reported that, in several cell lines, Dexamethasone, a synthetic glucocorticoid, modulates the sphingolipid metabolism and the intracellular sphingosine levels [1].

It was suggested [1] that its effects could be mediated by the production of sphingosine from membrane sphingomyelin.

Sphingosine modulates the cellular functions both through inhibition of protein kinase C (PK-C) activities and through a direct action on enzymes involved in phospholipid metabolism regulation [2].

In the present study we have examined the effect of Dexamethasone on Epstein Barr Virus transformed B lymphocytes on lipid composition and metabolism.

In particular sphingosine levels by ^{31}P and ^1H NMR spectroscopy, high performance liquid chromatography (HPLC) and Dexamethasone effects on membrane structure by fluorimetry have been investigated.

Furthermore, Dexamethasone effects on cellular proliferation and IgM secretion have been evaluated.

2 Materials and Methods

B lymphocytes from peripheral blood were transformed by means of EBV obtained from marmoset lymphoblastoid line B95-8 [3]. The resulting lymphoblastoid cell line was maintained in culture as described previously [4].

The concentration of Dexamethasone (Dex) used throughout the experiment was $2 \cdot 10^{-7}$ M.

For NMR experiments, following 30 min, 60 min, 120 min, 6 hr and 18 hr incubation periods at 37 °C EBV-B were harvested and washed three times in cold saline solution (4 °C).

Cells were subjected to chloroform/methanol/water extraction (2:2:1, v/v) [5]. The resulting aqueous and organic phases were separated, dried under N_2 flow, and stored at -80 °C. Incubation's media were saved and used for extracellular Choline (Cho) dosage performed by enzymatic- amperometric sensor [6].

For fluorimetry experiments, the effect of Dexamethasone and Sphingosine on membranes were evaluated measuring the diphenylhexatriene (DPH) polarization on intact cells, on a ISS-K2 spectrofluorometer [7].

The NMR measurements were carried out on the aqueous and organic phase of cellular extracts, on a XL300 Varian Spectrometer.

Cellular viability and proliferation, sphingosine levels and IgM secretion were determined as reported [4,8,9].

3 Results

The presence of Dexamethasone in the culture medium inhibits cellular growth at concentration ranging from 10^{-9} to 10^{-6} M.

The concentration used for the experiments shown is $2 \cdot 10^{-7}$ M (40% inhibition of cellular growth).

Fig. 1 depicts a typical P-31 NMR spectrum of the aqueous phase of control cell extract.

Treatment with Dexamethasone caused no significant change in phosphorylated metabolites, such as NTP, NDP, Pi, NAD, DPDE, nor changes in the cellular energy charge.

An increase of 25% of the intracellular phosphorylcholine (PCho) levels was observed only at 30 min of incubation with Dexamethasone; at the same time a significant increase (ca. 70%) is observed in extracellular Cho levels, as determined by an amperometric biosensor.

Treatment with Dexamethasone produced a significant increase at 30 min of incubation (ca. 100%) in intracellular Sphingosine levels, returning to control values after 1 hr of treatment.

A similar intracellular Sphingosine increase (ca. 98%) was observed when cells were incubated with extracellular Sphingosine levels for 30 min under the same conditions.

The IgM concentration in the medium shows a decrease (-45%) after a 18 hr incubation with both Dexamethasone or Sphingosine as determined through ELISA.

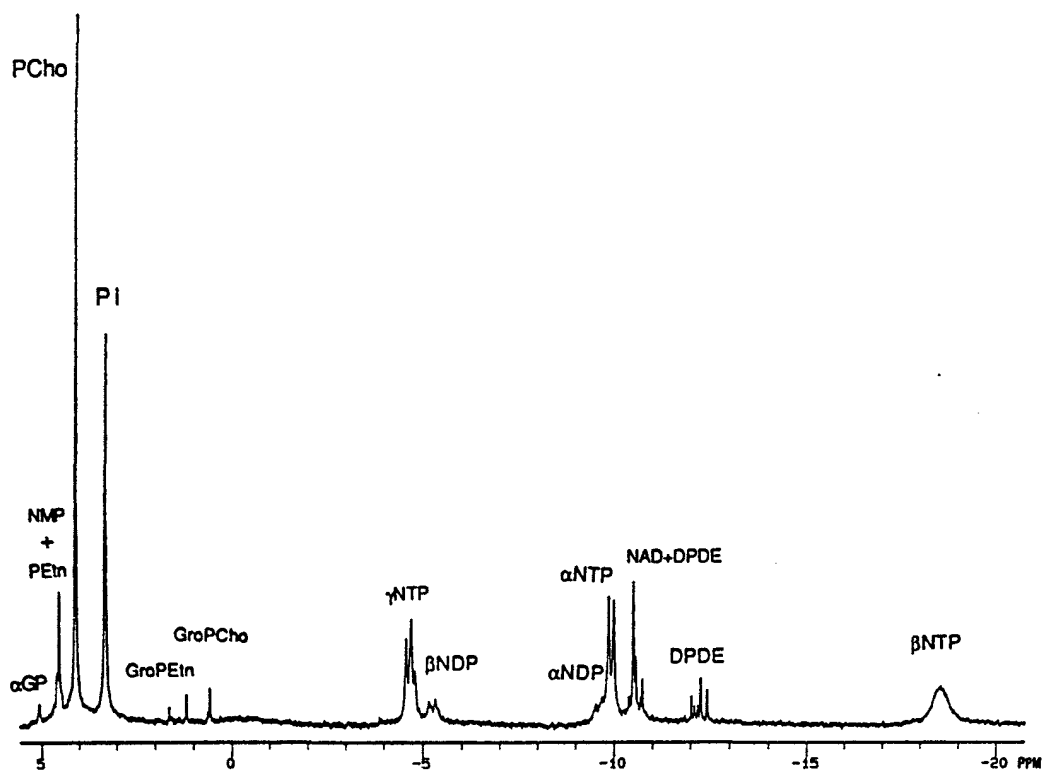
In Fig. 2 and 3 are reported a ^1H -1 and P-31 NMR spectra of extracts from untreated EBV-B lymphocytes.

Cells incubated with Dexamethasone for 30 min, 60 min and 120 min do not show any significant change in the concentration of phospholipids.

A ca. 30% increase in cholesterol levels at 30' of Dexamethasone treatment is observed which return to untreated cell values at 60 min and 120 min of incubation. Analogously, EBV-B lymphocytes incubated with Sphingosine for 30 min show a ca. 60% increase in cholesterol levels. (Fig.4)

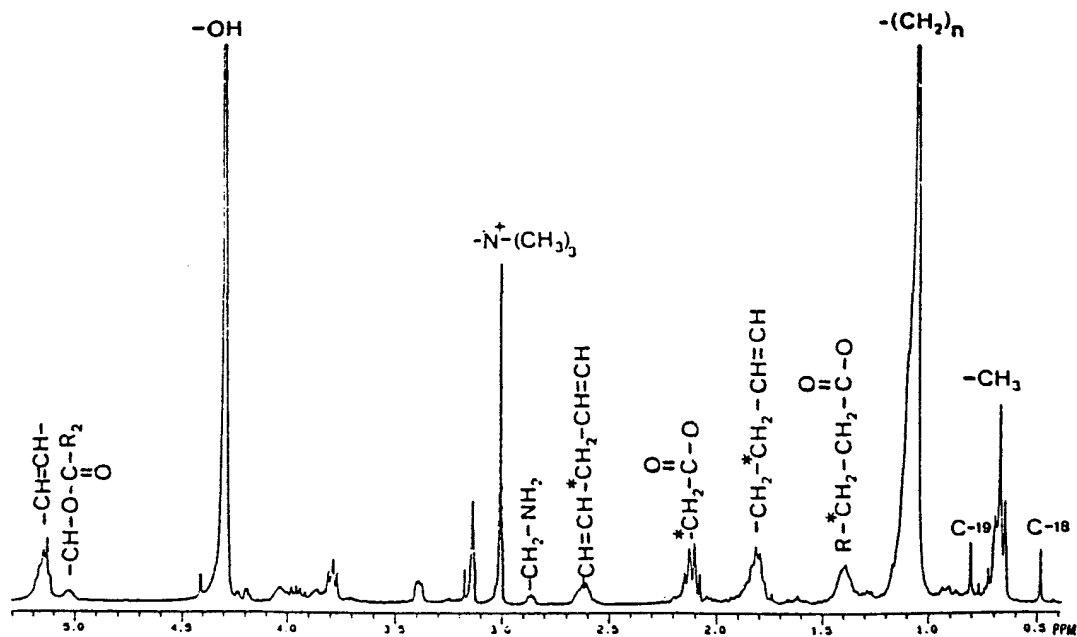
In agreement with cholesterol increase, the DPH polarization of cells treated with Dexamethasone or Sphingosine show a 15% and 40% increase respectively after 30 min of incubation.

Fig. 1



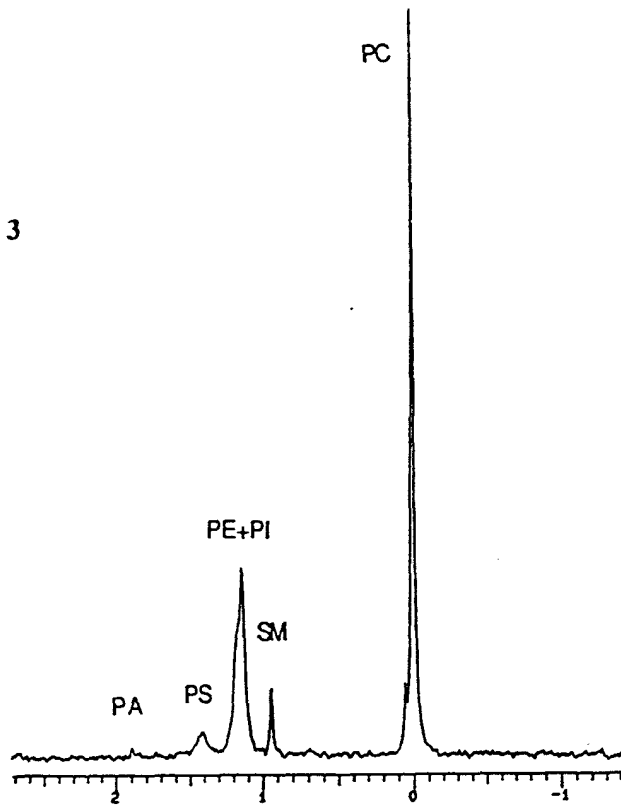
Spectra were carried out on a XL 300 Varian spectrometer. ^{31}P NMR spectra were obtained using a Waltz decoupling technique under the following spectral conditions: pulse width = $12 \mu\text{s}$ (45° pulse) delay time between pulses = 4 s; 16 K memory; spectral width = 10000 Hz; and temperature = 22°C .

Fig. 2



High resolution ^1H NMR spectra were obtained under the following spectral conditions: pulse width = $10 \mu\text{s}$ (45° pulse); delay time between pulses = 4 s; 16 K memory; spectral width = 4000 Hz; temperature = 22°C .

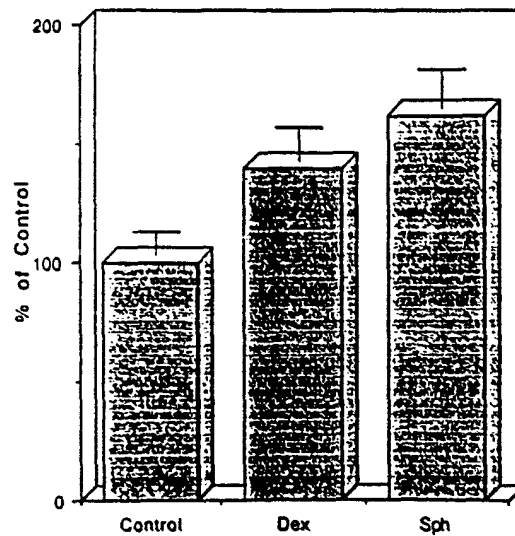
Fig. 3



Spectra were carried out on a XL 300 Varian spectrometer. ³¹P NMR spectra were obtained using a Waltz decoupling technique under the following spectral conditions: pulse width=12 μs (45° pulse) delay time between pulses = 4 s; 16 K memory; spectral width=10000 Hz; and temperature = 22°C.

Changes in total cholesterol concentrations (30 min)

Fig. 4



4 Discussion

-Significant modifications on sphingosine and cholesterol levels, intracellular PCho, extracellular Cho, cellular proliferation and IgM secretion are present only at 30 minutes and 1 hour of treatment.

-The 30 min treatment with Dexamethasone cause an increase in the cellular sphingosine level.

-Dexamethasone and Sphingosine [4,8] cause a breakdown of choline containing phospholipids, an increase in cholesterol level as well as a decrease in cellular proliferation and IgM secretion.

-The increase in total cholesterol level is consistent with an increase in the membrane rigidity as measured by DPH polarization in intact treated cells.

-The transient increase in total cholesterol could not be due to metabolic effect but more to a sphingosine dependent inhibition of cholesterol mobilization from intracellular stores in agreement with previous data relative to different cell line [10].

-This hypothesis should be confirmed by the use of specific probes in fluorescence experiments.

5 References

- 1-Ramachandran C.K., Murray D.K. and Nelson D.H. (1990) *Biochim. Biophys. Res. Commun.* 167, 607-613.
- 2-Merril A.H. Jr. (1991) *J. Bioenerg. Biomembr.* 23, 83-104.
- 3-Lombardi G., Del Gallo F., Vismara D., Piccolella E., De Martino C., Garzelli G., Puglisi C. and Colizzi V. (1987) *Cell. Immunol.* 107, 131-139.
- 4-Miccheli A., Ricciolini R., Piccolella E., Delfini M. and Conti F. (1991) *Biochim. Biophys. Acta* 1093, 29-35.
- 5-Bligh E.G. and Dyer W.J. (1959) *Can. J. Biochem. Physiol.* 37, 911-917.
- 6-Campanella L., Tomassetti M. and Sammartino M.P. (1988) *Analyst* 113, 77-80.
- 7-Van Blitterswijk W.J., Van Der Meer W.B. and Hilkmann H. (1987).
- 8-Miccheli A., Ricciolini R., Lagana' A., Piccolella E. and Conti F. (1991) *Biochim. Biophys. Acta* 1095, 90-92.
- 9-Boirivant M., Quintieri F., Pugliese O., Famularo C., Fais F. and Pallone F. (1990) *J. Clin. Immunol.* 10, 128-134.
- 10-Mendez A.J., Oram J.F. and Bierman E. L. (1991) *J. Biol. Chem.* 266, 10104-10111.

PERIPHERAL ARTERIOPATHY IN THE RAT: EFFECT OF LEVOCARNITINE PROPIL TREATMENT STUDIED BY ^{31}P NMR SPECTROSCOPY

Aureli T.,* Capuani G.,* Di Cocco M.E.,# Miccheli A.,# Corsico N.,\$ Nardone A.,\$
Arrigoni Martelli E.\$ and Conti F.#

* Institute for Research on Senescence and \$ Research and Development, SIGMA-TAU, Pomezia, Italy - #
Dept. of Chemistry, University "La Sapienza" Rome - Italy

1 INTRODUCTION

Peripheral vascular disease (PVD) is a common human pathological condition associated to a reduced motor performance and impairment in the muscle energy metabolism. Patients affected by PVD showed an alteration in carnitine homeostasis, and it has been also reported that carnitine administration in these patients induces a marked improvement in walking capacity (1).

In the present study we applied ^{31}P nmr spectroscopy in order to a) characterize the biochemical changes occurring in muscular tissue, following to an experimental model of peripheral vascular insufficiency in the rat.

b) to evaluate the effectiveness of levocarnitine propil (Propionil-l-carnitine ; PLC) a naturally occurring derivative of carnitine to counteract the damage in the muscle energy metabolism.

2 METHODS

Male wistar rats weighing 270-290 g were used. Peripheral vascular insufficiency was induced by sodium laurate (Na-laurate) injection in both femoral arteries as described in (2). Animals were subdivided into 6 groups: A (control), B (sham operated), C (sham operated + PLC), D (Na-laurate), E (Na-laurate + PLC after 24h), F (Na-laurate + PLC after 4 days). PLC treatment started 24 h after Na-laurate injection and lasted for 14 days, at the daily dose of 120 mg/kg b.w. by oral gavage. In the E group, PLC treatment started after 4 days from Na-laurate administration. All the rats were sacrificed after 15 days from surgical procedures and gastrocnemius muscle was frozen and extracted using a mixture of chloroform, methanol and water at final proportion of 2:2:1 (v/v) according to (3).

3 RESULTS AND CONCLUSIONS

In table 1 are reported the values expressed as % of total ^{31}P of metabolites observed in muscle extracts from 5

groups under study. Arterial administration of Na-laurate causes severe alterations on muscle energy metabolism, such as a decrease in the phosphocreatine (PCr) and ATP, content and increase in inorganic phosphate (Pi), ADP, and AMP+IMP. These changes could be likely due to an indirect effect deriving from the peripheral vascular insufficiency on muscle tissue. However a direct damaging action of Na-laurate on muscle tissue mediated by its detergent properties has to be also considered. Na-laurate treatment induces also a severe decrease in total muscle phosphorous content as evidenced in figure 2; which is suggestive of a muscular fibres necrosis. This effect was also evidenced by in vivo ^{31}P nmr spectra at different times after Na-laurate injection (fig.3), although the metabolite ratios (i.e. PCr/Pi, ATP/Pi seem to recovery to the control levels after 28 days of arteropathy induction. PLC treatment appears to be effective to counteract the alterations in muscle energy metabolism as evidenced by recovery of phosphorylated metabolite levels after 15 days (tab.1) and protects muscle from necrosis when started after 24 h but not after 4 days (fig. 1). However in this group high-energy phosphate levels are significantly higher than Na-laurate group suggesting a renewal of energy metabolism mediated by PLC also on muscle damaged fibres.

REFERENCES

- 1 Brevetti G., Chiarello M., Ferulano G. et al. *Circulation* 1988; 77: 767-773
- 2 Ashida S., Ishihara M., Ogawa H. et al. *Thromb. Res.* 1980; 18: 55-67
- 3 Miccheli A., Aureli T., Conti F. et al. *Cell. Mol. Biol.* 1988; 34: 591-603.

Table 1

Level (expressed as % of ^{31}P) of the metabolites observed in muscle extracts from the 6 groups under study.

	A	B	C	D	E	F
ATP	10,85±0,88	11,17±0,44	10,92±0,43	6,57±1,78**	10,69±2,12***	9,02±2,06
PCr	37,72±6,28	33,80±5,13	36,75±3,34	25,47±3,57*	33,03±5,41**	32,00±3,30@@
ADP	1,30±0,27	1,51±0,18	1,33±0,36	3,59±0,50***	2,58±2,06	3,85±1,63 ^
Pi	18,13±2,54	19,54±2,84	17,94±0,96	31,97±9,74*	21,22±7,27	24,13±5,00
AMP+IMP	2,16±0,99	3,01±0,61	2,33±1,32	12,26±6,83*	5,12±3,85 **	7,31±3,20 ^
SP	4,84±1,71	3,93±0,98	3,99±1,96	4,77±1,16	2,14±0,31 + #	2,65±0,21\$@
NAD+DPDE	2,72±0,33	3,29±0,84	2,98±0,56	4,71±1,20	3,51±0,80	4,10±1,51

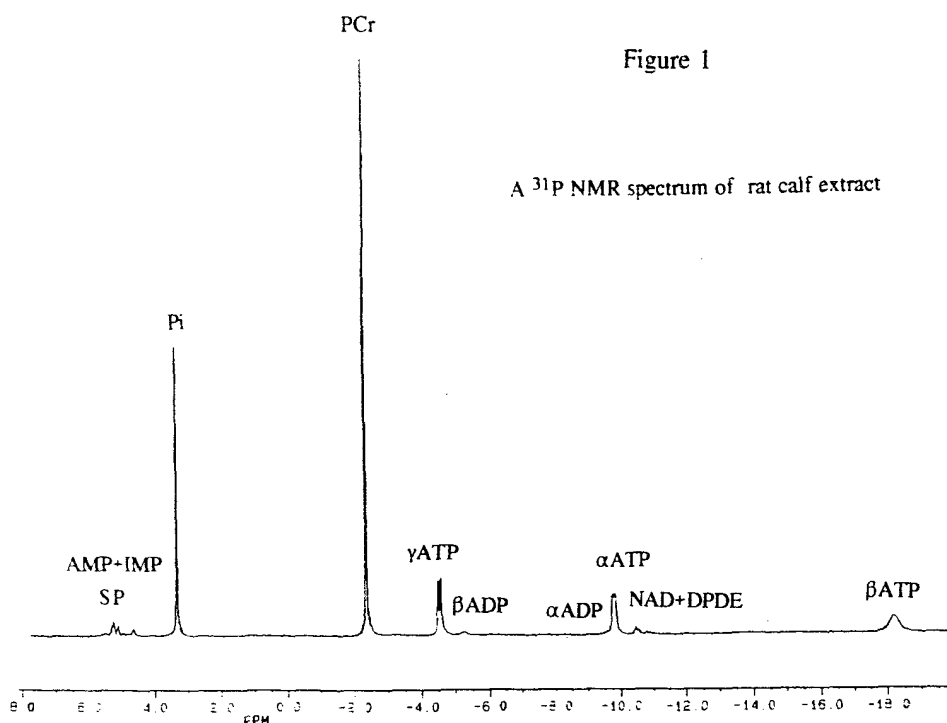
* p<0.05 D vs B; ** p<0.005 D vs B; *** p<0.001 D vs B;

^ p<0.05 F vs B # p<0.005 E vs D @ p<0.01 F vs D

+ p<0.01 E vs B \$ p<0.05 F vs B ## p<0.05 E vs D

@@ p<0.05 F vs D ### p<0.01 E vs D (Student's t-test)

A: control
 B: sham operated
 C: sham PLC
 D: Na-laurate
 E: Na-laurate+PLC (after 24 h)
 F: Na-laurate+PLC (after 4 days)



Total phosphorous contents values in rat muscles, expressed as $\mu\text{moles/mg}$ of protein, relative to different experimental groups.

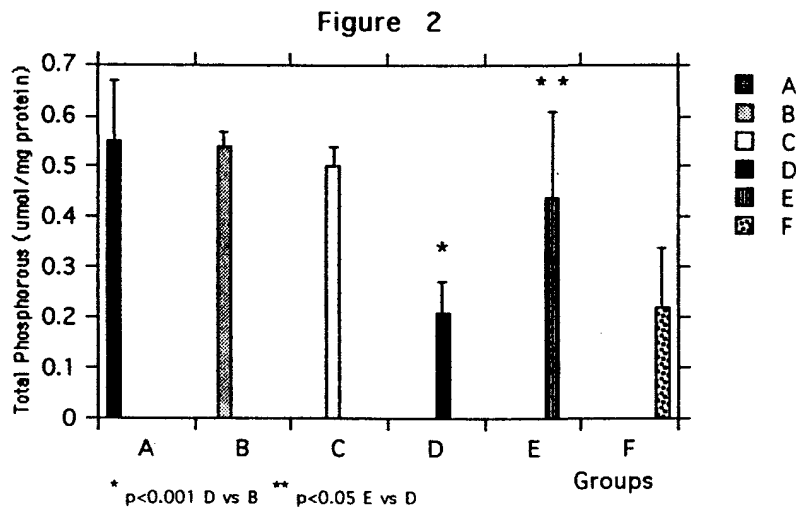
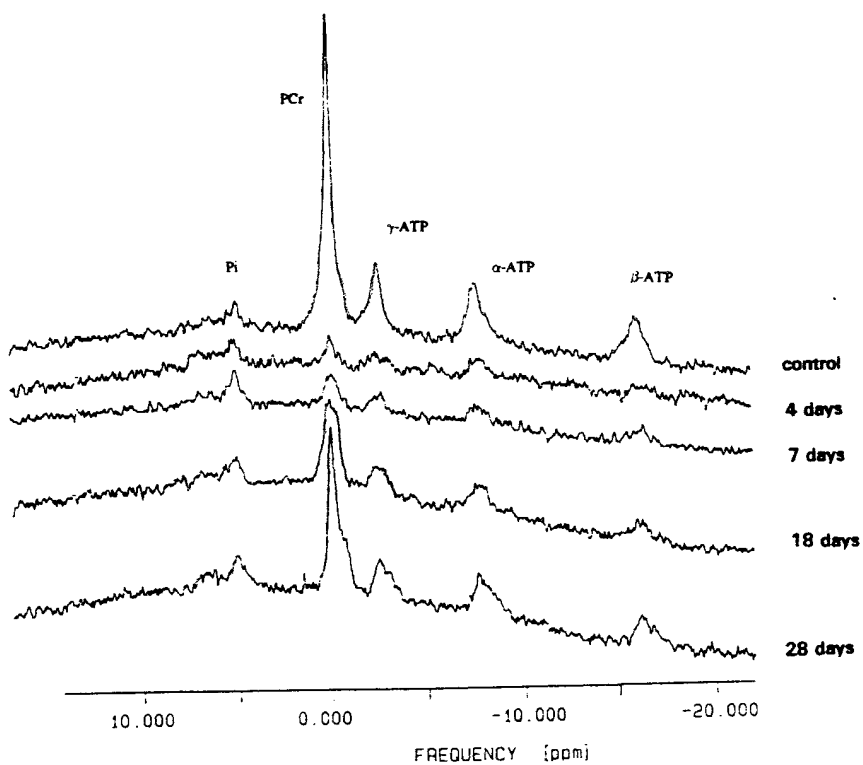


Figure 3



In Vivo ^{31}P NMR spectra of rat calf monitored before and after Na laurate injection

Tunnel Splitting of 2,3-Butanedione with Pressure Studied Using Low-field NMR Tunnelling Spectroscopy

P.M.Debenham[†], P.J.McDonald^{*}, A.J.Horsewill[†] and D.Vijayaraghavan^{*},

^{*}Department of Physics, University of Surrey, Guildford, UK. GU2 5XH

[†]Department of Physics, University of Nottingham, UK. NG7 2RD

December 20, 1992

Abstract

We report on the variation of a methyl tunnel splitting with pressure. The measurements are the first studies of the pressure variation of a methyl tunnel splitting using low-field, of order 80 gauss, dipole-dipole driven NMR spectroscopy with rapid field-cycling. Pressures up to 1.8kbar were applied with an operating temperature of 4.2K. In addition proton spin-lattice relaxation time T_1 data has been collected up to 6.25kbar. Using an established theoretical model the two data sets have been combined to give the tunnel splitting throughout the entire pressure range. Further calculations give the potential barriers, including a small six fold term, needed within the crystal to produce these results. The overall height of the hindering potential and its shape are compared with the potential calculated from the crystal structure.

1 Introduction

Methyl group dynamics shows a smooth transition from a low temperature quantum tunnelling regime [2, 3, 4] to a higher temperature thermally activated hopping regime. The methyl thermometer model [3] says that the thermal hopping rate is only determined by the height of the potential barrier hindering rotation and by the sample temperature. This results in a well demonstrated correlation between the quantum tunnelling frequency and the classical temperature at which the spin lattice relaxation time T_1 is a minimum. By using a sample with a high inter molecular component to the hindering potential, application of hydrostatic pressure allowed us to smoothly vary the hindering potential and so study the effect this had on the dynamical motion of the methyl group.

In our study we used both conventional measurements of the proton spin lattice relaxation time and field cycling NMR to measure the tunnelling frequency of our sample diacetyl (2,3-Butanedione). Both sets of measurements were performed at a range of pressures between atmospheric and 6.25kbar. All measurements of the quantum tunnelling frequency were performed at 4.2K. The pressure was applied to the sample using a three stage helium compressor.

2 Theory

To analyse the NMR data we require a mathematical model connecting the experimental observables, namely the tunnel frequency, ν_t , T_1 , and the barrier height, $V(\phi)$. We used

the methyl thermometer model [3] with the single change that instead of just using a threefold potential, $V(\phi)$, we used a potential containing threefold and sixfold contributions.

$$V(\phi) = \frac{V_3}{2}(1 - \cos(3\phi)) + \frac{V_6}{2}(1 - \cos(6\phi + \delta)) \quad (1)$$

Solving the standard hamiltonian for a methyl group with this form of potential $V(\phi)$, gives the eigenvalues and eigenstates. From this the tunnelling frequency and the expectation values of the angular momentum are obtained. The T_1 values then are calculated using the simple BPP expression for spin-lattice relaxation time [2, 4]. The only variable to adjust to give the exact fit is the value of T_1 at one particular point.

3 Results

Figures 1 and 2 show the spectra obtained using low field field-cycling NMR at a range of pressures. These spectra clearly show that the tunnel frequency reduces as the pressure increases. Computer fits using three Gaussian lines of equal width were used to obtain the values of tunnel frequency later used.

Spin lattice relaxation time measurements (Figure 3) show that the temperature θ_{min} , of the T_1 minimum moves to higher temperature as pressure increases.

The ratio of $V_3:V_6$ was primarily determined by the optimum fit to the atmospheric T_1 data while the sum V_3+V_6

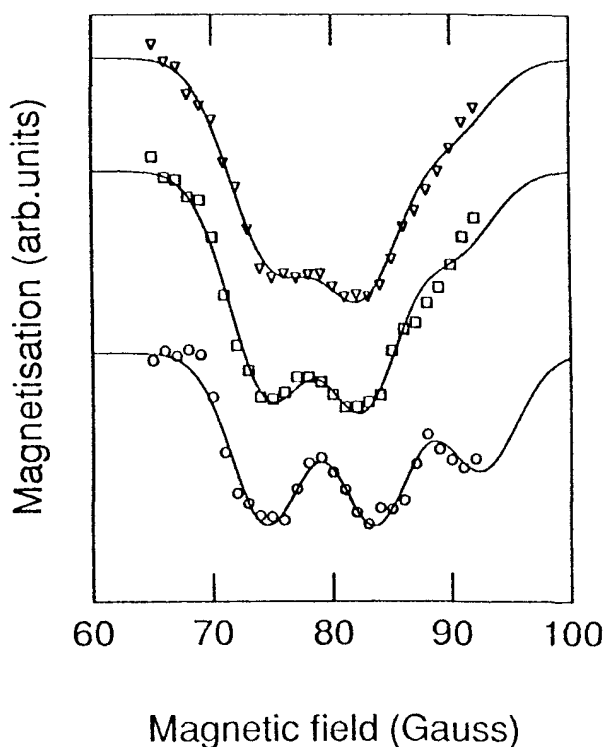


Figure 1: Tunnelling spectra recorded from Diacetyl at atmospheric pressure (circles), 0.43kbar (squares) and 0.66kbar (triangles). Computer fits to the data are shown as solid lines.

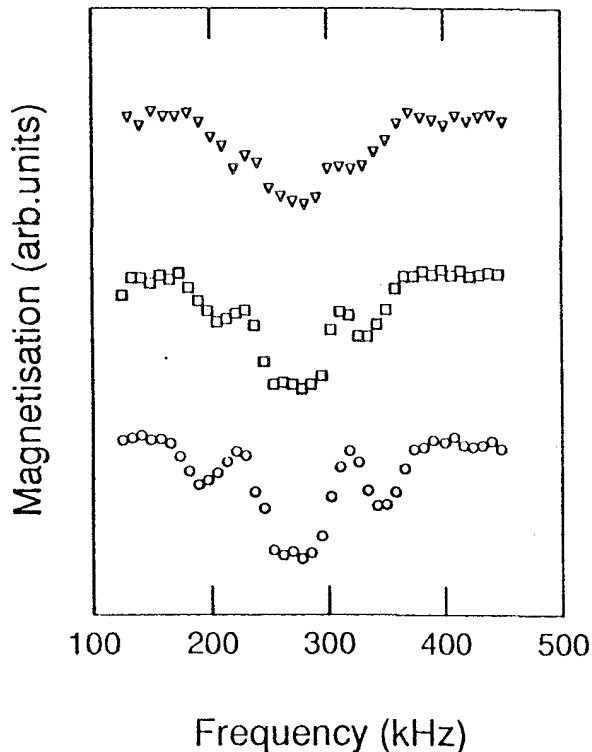


Figure 2: Tunnelling spectra recorded from Diacetyl at atmospheric pressure (circles), 0.24kbar (squares) and 1.0kbar (triangles).

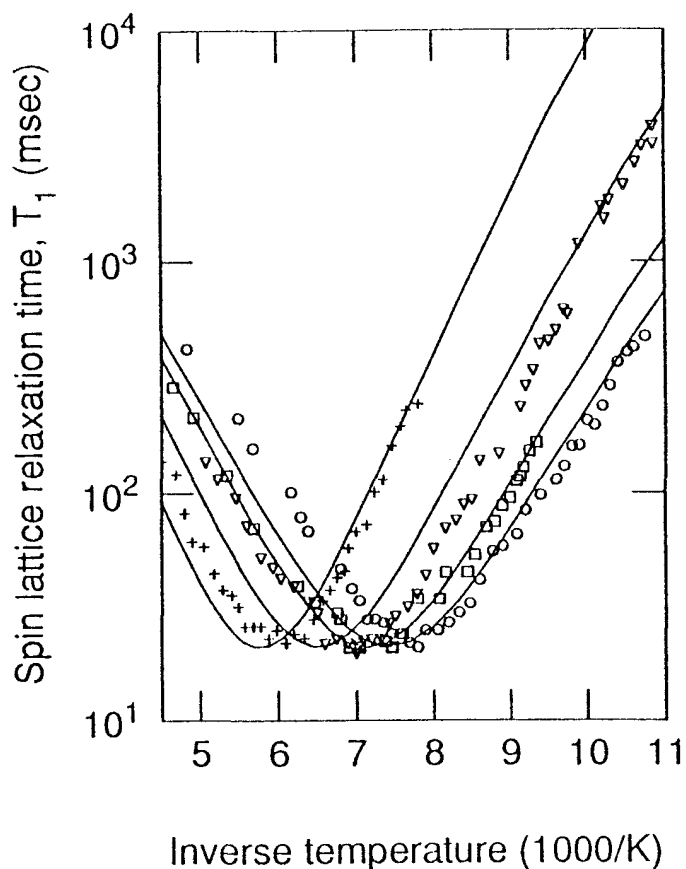


Figure 3: Temperature dependence of the spin lattice relaxation time, T_1 in diacetyl measured at atmospheric pressure (circles), 1.0kbar (squares), 3.4kbar (triangles) and 6.25kbar (crosses) together with respective fits according to the modified methyl thermometer model.

was determined by the fit to the tunnel splitting. For the higher pressures the ratio was kept constant with V_6 being 19% of the total potential and the sum was varied. In all cases $\delta = 0^\circ$.

4 Structural analysis

From lattice sums of pairwise interactions between methyl hydrogen atoms [1] it was calculated that V_6 should be 18% of the total barrier. This agrees well with our observed value of 19%.

By use of the compressibility of a typical crystal and assuming the interatomic potential to be of form Kr^{-n} we can calculate from the rate of change of hindering potential with pressure, $\frac{\partial V}{\partial p}$, that $n=11.6$. This parameter corresponds to the inter molecular term of the potential only as the intra molecular term is insensitive to pressure.

5 Conclusion

Our results have extended the methyl thermometer correlation down to a tunnel frequency of 6.25kHz with a corresponding θ_{min} of 169K. The small sixfold term added to the hindering potential gives the best fit and is partially justified by analysis of diacetyl's crystal structure. Finally the exponent value ($n=11.6$) or the interatomic potential agrees with other materials and is consistent with the repulsive part of a Lennard Jones inter atomic potential.

This work has been published in full in Molecular Physics [5].

References

- [1] A.M. Alsanossi and A.J. Horsewill. *Chem.Phys*, 160:25, 1992.
- [2] S. Clough, A. Heidemann, A.J. Horsewill, J.D. Lewis, and M.N.J. Paley. *J.Phys.C*, 14:L525, 1981.
- [3] S. Clough, A. Heidemann, A.J. Horsewill, J.D. Lewis, and M.N.J. Paley. *J.Phys.C*, 15:2495, 1982.
- [4] S. Clough and P.J. McDonald. *J.Phys.C*, 15:L1039, 1982.
- [5] P.J. McDonald, D. Vijayaraghavan, P.M. Debenham, and A.J. Horsewill *Molec.Phys*, 78:219, 1993.

Spin-Lattice Relaxation for Dideuterium

Leon C. ter Beek and E. Elliott Burnell

Department of Chemistry, University of British Columbia,
2036 Main Mall, Vancouver, B.C., Canada V6T 1Z1

The Zeeman spin-lattice relaxation rates for ortho- and para-dideuterium, 2H_2 , have been measured experimentally in partially oriented nematic solvents at 304 K using 2H -NMR. The solvents used are: PCH-7, 1132 and a 55 wt% 1132/EBBA mixture. These oriented solvents make it possible to separate the resonances of the ortho and para configurations thereby facilitating the determination of the relaxation rates directly without multi-exponential analysis. The relaxation rate of para-dideuterium is about twice that of ortho-dideuterium in all experiments.

We have derived expressions for the Zeeman spin-lattice relaxation rates based on a quadrupolar, dipolar, and spin-rotation Hamiltonian. By performing the proper averaging over the rotational states, we obtain excellent agreement with our experimental results.

I. INTRODUCTION

Both the ortho and para species for two coupled deuterons are observable with 2H -NMR. Around liquid nitrogen temperatures Hardy [1,2] observed that the ortho-species of dideuterium relaxes more slowly than the para-species. This is because almost all of the ortho-species are in the $J=0$ rotational state. This state is spherically symmetric and therefore not responsible for relaxation. In this paper we will show both experimentally and theoretically that both species will have distinct relaxation rates at much higher temperatures.

The master equation for the evolution of the density matrix under the effect of a random perturbation [3-5] from a Hamiltonian containing only the quadrupolar interaction predicts that the Zeeman spin-lattice relaxation rate $R(F_{10})$, where $F_{10} = I_z$ [6], of dideuterium is equal for ortho and para configurations [7]. Including the dipolar term in the Hamiltonian predicts different relaxation rates for both species due to the cross-terms between the dipolar and quadrupolar couplings.

The 2H -NMR spectrum of oriented dideuterium has been investigated by Burnell *et al.* [8-10]. It has been shown that the NMR signals from the ortho and para species are distinguishable and can be calculated from the transition frequencies as a function of the coupling constants [8]. Although the solute dideuterium has a very small order parameter of about 10^{-3} , justifying the isotropic average for our calculation, the couplings are sufficient to give rise to observable splittings due to the quadrupolar and dipolar interactions. The 2H -NMR spectrum of dideuterium dissolved in an anisotropic liquid is dominated by these quadrupolar and dipolar interactions (Figure 1).

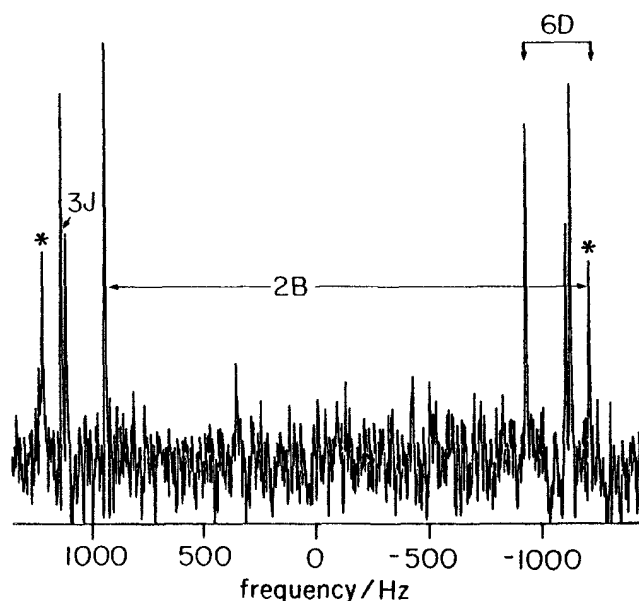


FIG. 1. A 400 MHz 2H -NMR-spectrum of dideuterium partially oriented in the nematic liquid crystal mixture 55 wt% 1132/EBBA at 304 K. The *'s label the transitions from para-dideuterium.

II. THEORY

For homonuclear diatomic molecules in which the nuclei obey Bose-Einstein statistics the product of the spin and vibration-rotation wave functions is symmetric with respect to permuting the individual nuclei. The states into which the molecule can be separated are ortho and para corresponding to the six symmetric spin states for total angular momentum $I=0$ and 2 and the three anti-symmetric spin states for $I=1$, respectively. The para species can occupy the odd rotational levels ($J=1,3,5,\dots$), and the ortho species the even ones ($J=0,2,4,\dots$). The rate of conversion between the ortho and para states is extremely slow in the absence of strong magnetic field gradients. Therefore, these states are well defined in our NMR experiments and give rise to separate spectra.

For a small diatomic molecule the rotational states are well defined since the rotational levels J are well separated and thus not much affected by life-time shortening due to the many collisions in the dense medium. Therefore we can treat a diatomic molecule as a well-defined quantum rotor and weigh each state by the appropriate Boltzmann factor.

The measured Zeeman spin-lattice relaxation rate $R(F_{10})$ can be expressed as a weighted average over the even or odd rotational states for ortho and para, respectively

$$R(F_{10}) = \sum_J' P_J (R(F_{10}))_J \quad (1)$$

$$P_J = \frac{(2J+1)e^{-J(J+1)\theta/T}}{\sum_J' (2J+1)e^{-J(J+1)\theta/T}} \quad (2)$$

where θ is the rotational constant for dideuterium and T the absolute temperature. The primes on the summation symbols indicate that the summations are to be taken over even J (ortho) or odd J (para).

In order to calculate the relaxation expressions in the Redfield approximation we need to write our total interaction Hamiltonian in spherical tensor form. For two nuclei with spin-1 we focus on the quadrupolar $\hbar\mathcal{H}_q$ and dipolar $\hbar\mathcal{H}_d$ second rank interaction Hamiltonians given by [3]

$$\mathcal{H}_q = \sqrt{\frac{24\pi}{5}} \frac{B}{3} \sum_{m=-2}^2 (-1)^m f_{2m}(I_1 + I_2) Y_{2-m}(\theta(t), \phi(t)) \quad (3)$$

and

$$\mathcal{H}_d = \sqrt{\frac{24\pi}{5}} D \sum_{m=-2}^2 (-1)^m f_{2m}(I_1, I_2) Y_{2-m}(\theta(t), \phi(t)) \quad (4)$$

where

$$B = \frac{3e^2qQ}{4\hbar} \quad (5)$$

is the quadrupolar coupling constant of the spin-1 nucleus and

$$D = -\frac{\mu_0 \hbar \gamma^2}{4\pi r^3} \quad (6)$$

is the dipolar coupling constant between the nuclei. $Y_{2m}(\theta, \phi)$ is a spherical harmonic of the angles θ and ϕ associated with the vector joining the two nuclei and f_{2m} is the m -th spherical component of the normalized irreducible tensor of rank 2 associated with either the quadrupolar, $f_{2m}(I_1 + I_2)$, or dipolar, $f_{2m}(I_1, I_2)$, interaction.

$$f_{20}(I_1 + I_2) = \sqrt{\frac{1}{6}} (3(I_{1z}^2 + I_{2z}^2) - 4) \quad (7)$$

$$f_{20}(I_1, I_2) = \sqrt{\frac{1}{6}} (2I_{1z}I_{2z} - \frac{1}{2}(I_{1+}I_{2-} + I_{1-}I_{2+})) \quad (8)$$

$$f_{2\pm 1}(I_1 + I_2) = \mp \frac{1}{2} (I_{1z}I_{1\pm} + I_{1\pm}I_{1z} + I_{2z}I_{2\pm} + I_{2\pm}I_{2z}) \quad (9)$$

$$f_{2\pm 1}(I_1, I_2) = \mp \frac{1}{2} (I_{1z}I_{2\pm} + I_{1\pm}I_{2z}) \quad (10)$$

$$f_{2\pm 2}(I_1 + I_2) = \frac{1}{2} (I_{1\pm}^2 + I_{2\pm}^2) \quad (11)$$

$$f_{2\pm 2}(I_1, I_2) = \frac{1}{2} (I_{1\pm}I_{2\pm}) \quad (12)$$

Since the ortho and para states don't mix we can write the f_{2m} as a direct sum of the f_{2m}^{ortho} and the f_{2m}^{para} and evaluate each of them separately. However, the transitions between the $I=0$ and $I=2$ states do play an important role for the ortho species as will be shown later. Note that the f_{2m} are second rank spherical tensors associated with the Hamiltonian and the F_{lm} are spherical tensors associated with the possible spin-states [11].

The master equation for relaxation of an observable F_{lm} under the Hamiltonian $\mathcal{H}_q + \mathcal{H}_d$ is given by

$$\begin{aligned} \frac{d}{dt} \langle F_{lm} \rangle = & - \sum_{n=-2}^2 Tr([F_{lm}, Df_{2n}(I_1, I_2) \\ & + \frac{B}{3} f_{2n}(I_1 + I_2)], Df_{2-n}^\dagger(I_1, I_2) \\ & + \frac{B}{3} f_{2-n}^\dagger(I_1 + I_2)], (\sigma - \sigma_{eq})) J(n\omega) \end{aligned} \quad (13)$$

The conditions for the validity of this master equation (eg. fast motion) have been discussed by Abragam

[3]. The coupling constants are in angular frequency units. The spectral density $J(\omega)$ is given by $|(-1)^m \sqrt{\frac{24\pi}{5}} Y_{2m}|^2 j(\omega)$, which in the case of classical isotropic tumbling ($|\overline{Y_{2m}}|^2 = \frac{1}{4\pi}$) reduces to $\frac{6}{5}j(\omega)$, where $j(\omega)$ is the reduced spectral density. In the short correlation time limit the spectral density is proportional to the correlation time τ_l , associated with the l -th rank interaction.

Using Equation 13, the results of the time dependence of the expectation value of F_{10} for para- and ortho-dideuterium are given by the following differential equations:

$$\frac{d}{dt} \langle F_{10}^{para} \rangle = -\frac{2}{15}(B-3D)^2 \{j_1 + 4j_2\} \times (\langle F_{10}^{para} \rangle - \langle F_{10}^{para} \rangle_{eq}) \quad (14)$$

$$\begin{aligned} \frac{d}{dt} \langle F_{10}^{ortho} \rangle = & -\frac{2}{15}(B^2 + \frac{6}{5}BD + \frac{27}{5}D^2) \{j_1 + 4j_2\} \\ & \times (\langle F_{10}^{ortho} \rangle - \langle F_{10}^{ortho} \rangle_{eq}) \\ & - \frac{2}{15}(\frac{48}{5}BD + \frac{36}{5}D^2) \{j_1 - j_2\} \langle F_{30}^{ortho} \rangle \end{aligned} \quad (15)$$

The effective interaction for para dideuterium is $B-3D$, which is in agreement with expectation based on the splitting between the para-lines in the spectrum of dideuterium. If there were no mixing between the $|2,0\rangle$ and $|0,0\rangle$ states the effective interaction for the ortho-state would be $B+3D$, but due to mixing the effective interaction is more complicated. Naturally, the two rates are equal when the spins are not coupled (i.e. $D=0$) and the equations become identical to those for a single spin $I=1$ [7,12].

In the relaxation of F_{10} of the ortho-species there is a cross term to the octapolar magnetization, F_{30} . Fortunately, in the short correlation time limit this term vanishes, since $j_1 = j_2$ ¹.

The first rank spin-rotation interaction which is very important for diatomic molecules [2] can simply be added to the final expression since there will be no cross terms between first and second rank interactions. Using the short correlation time limit and the assumption normally used for dideuterium in the gas phase, that relaxation does not depend on transitions between J levels [3], we end up with the following equations for the relaxation of F_{10} of dideuterium for every J -level:

$$\begin{aligned} R(F_{10}^{ortho})_J = & \frac{2}{3}W^2 J(J+1)\tau_1 + \\ & \frac{2}{15}(B^2 + \frac{6}{5}BD + \frac{27}{5}D^2)5\tau_2 \frac{J(J+1)}{(2J-1)(2J+3)} \end{aligned} \quad (16)$$

¹In a later paper we'll be dealing with all 5 relaxation terms for the para- and all 14 terms for the ortho-species for two coupled spin-1 nuclei. In all cases cross terms vanish in the short correlation time limit.

Liquid Crystal	$R(F_{10}^{ortho})^{-1\dagger}$ (s)			$R(F_{10}^{para})^{-1}$ (s)
PCH-7	12.4±1.5	12.5±3.4	12.1±1.0	6.2±1.5
ZLI-1132*	10.4±1.3	10.6±0.6	11.7±0.6	6.6±0.6
55% 1132/EBBA	12.3±1.5	12.7±2.0	12.3±1.9	6.3±0.9

TABLE I. The Zeeman relaxation times for ortho and para dideuterium in several nematic solvents. † These values are measured from the three different ortho-peaks of one half of the spectrum (see Fig. 1). * Data from [14]

$$\begin{aligned} R(F_{10}^{para})_J = & \frac{2}{3}W^2 J(J+1)\tau_1 + \\ & \frac{2}{15}(B-3D)^2 5\tau_2 \frac{J(J+1)}{(2J-1)(2J+3)} \end{aligned} \quad (17)$$

where W is the spin-rotation coupling constant between the magnetic moments of the spins and the magnetic field produced at their sites by the rotation of the molecule. We neglect the J dependence of W , B , and D [13], since it is very small for dideuterium.

III. EXPERIMENTAL

The 2H_2 gas, prepared by electrolyzing 99.8% liquid 2H_2O , was condensed at liquid helium temperature into three 9 mm OD standard pyrex glass tubes, chosen so they fit snugly inside high resolution 10 mm OD NMR tubes. Each of the tubes contains one of the following liquid crystal solvents: PCH-7, Merck ZLI-1132, or a 55 wt% ZLI-1132/EBBA mixture. All three solvents were commercially available. The tubes were flame sealed and a final pressure of 2H_2 above the solvent of about 25 atm at 304 K is obtained. The 2H -NMR spectra for the Zeeman spin-lattice relaxation times were acquired at 304 K on a Bruker WH-400 spectrometer using a standard $(\pi - t_1 - \frac{\pi}{2} - acquisition)$ inversion recovery sequence and 64 scans.

IV. EXPERIMENTAL RESULTS AND DISCUSSION

The experimental results were obtained by fitting the $R(F_{10})$ data sets $\{S(t)\}$ for ortho and para to a three parameter fit

$$S(t) = C_1 - C_2 e^{-t/C_3} \quad (18)$$

which in the case of the spin-inversion recovery experiment with perfect 180° pulses gives the equilibrium magnetization $C_1 = M_0$, $C_2 = 2M_0$, and the Zeeman spin-lattice relaxation time $C_3 = R(F_{10})^{-1}$. The relaxation times obtained for each of the four peaks in one half of the dideuterium spectrum are given in Table 1.

To compare the relaxation equations with experiment we use a τ_1/τ_2 ratio of 3 [15], take the values for $\theta=43.826$

$K, W = 55.090 \times 10^3 \text{ s}^{-1}$, $B = 1060.25 \times 10^3 \text{ s}^{-1}$, and $D = -43.007 \times 10^3 \text{ s}^{-1}$ for dideuterium from reference [13,16], and find the value of τ_2 ($4.3 \times 10^{-13} \text{ s}$) that gives the best fit to our experimental results. From the one parameter fit to τ_2 we obtain a spin-lattice relaxation time $R(F_{10})^{-1}$ of 6.3 s for para and 12.5 s for ortho dideuterium. These values agree very well with the experimental values given in Table 1.

V. CONCLUSIONS

Interference effects between the second rank dipolar and quadrupolar interactions give different expressions for the relaxation of ortho and para species of a homonuclear diatomic molecule with nuclear spins $I \geq 1$. Also the different J dependencies for ortho and para dideuterium contribute to the different measured relaxation rates. In the long correlation time limit the spin-lattice relaxation rate for the ortho-species is predicted to be non-exponential because of the coupling between the Zeeman and octapolar order. Experimental results on the spin-lattice relaxation time $R(F_{10})$ of dideuterium are in excellent agreement with our calculations, showing a ratio of 0.5 between the ortho and para spin-lattice relaxation rates.

VI. ACKNOWLEDGEMENTS

The authors wish to thank Dr. K.R. Jeffrey for useful discussions and for recalculating our relaxation expressions independently considering transition probabilities between the various energy levels. This work is supported by a research grant from the National Sciences and Engineering Research Council of Canada.

- [8] E.E. Burnell, C.A. de Lange, J.G. Snijders, 1982, *Phys. Rev. A*, **25-4**, 2339
- [9] E.E. Burnell, A.J. van der Est, G.N. Patey, C.A. de Lange, J.G. Snijders, 1987, *Bull. Magn. Res.*, **9**, 4
- [10] A.J. van der Est, E.E. Burnell, J. Lounila, 1988, *J. Chem. Soc., Faraday Trans. 2*, **84**, 1095
- [11] H.A. Buckmaster, R. Chatterjee, Y.H. Shing, *Phys. Stat. Sol.*, **13a**, 9-50 (1972)
- [12] K.R. Jeffrey, 1981 *Bull. Magn. Res.*, **3**, 69
- [13] N.F. Ramsey, 1956, *Molecular Beams*, Oxford University Press.
- [14] E.E. Burnell, C.A. de Lange, private communication
- [15] M. Bloom, I. Oppenheim, *Advances in Chemical Physics*, **12**, 549 (J.O. Hirschfelder, editor), Wiley, New York
- [16] R.F. Code, N.F. Ramsey, 1971, *Phys. Rev. A*, **4**, 1945

-
- [1] W.N. Hardy, *PhD thesis, University of British Columbia*, 1964
 - [2] M. Bloom, 1972, in MTP International Review of Science, physical chemical science series one, Vol. 4, (C.A. McDowell, editor), Butterworth, London
 - [3] A. Abragam, 1961, *The Principles of Nuclear Magnetism*, Clarendon Press, Oxford
 - [4] C.P. Slichter, 1989, *Principles of Magnetic Resonance*, Springer Verlag
 - [5] M. Goldman, 1988, *Quantum Description of High-Resolution NMR in Liquids*, Clarendon Press, Oxford
 - [6] The Zeeman spin-lattice relaxation rate is more commonly known as $1/T_{1Z}$. In this paper we adopt a more general notation since we are dealing with different time dependences of the spherical tensors F_{lm} .
 - [7] M. Bloom, P. Beckmann, B.C. Sanctuary, 1976, *Can. J. Phys.*, **54**, 2209

HIGH-RESOLUTION ^{13}C AND ^{15}N SOLID-STATE NMR INVESTIGATIONS OF THE CURING REACTION OF CYANATE RESINS

C. A. Fyfe; J. Niu; S. Rettig; and N. E. Burlinson

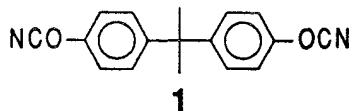
Dept. of Chemistry, Univ. of British Columbia, Vancouver, Canada, V6T 1Z1
and

C. Reidsema; D. Wang and M. Poliks

IBM Corp., Systems Technology Division, Endicott, NY, USA

INTRODUCTION

Traditional electronic circuit boards are made from glass fibre reinforced epoxy resins. However, they often fall short of the thermal and electrical performance demands of many modern high speed devices. With trends toward increased circuit densities, shorter propagation delays, elevated operating temperatures, and higher reliability, many new advanced materials are being developed to satisfy these demand. Among these materials, cyanate resins are considered to be very promising,^[1] exhibiting many superior properties for high speed electronic circuit boards^[2]. The cyanate resin most commonly used is based on Bisphenol A dicyanate (BPADCN) 1. The present work is an investigation of the curing mechanism of cyanate resin both in solution and in the bulk by ^{13}C and ^{15}N high resolution solid-state NMR.

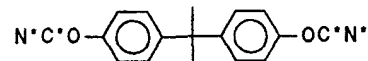
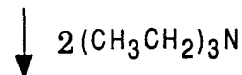
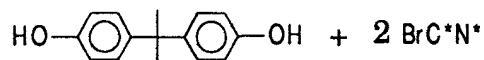


EXPERIMENTS

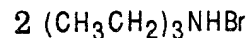
1. NMR EXPERIMENT

^{13}C and ^{15}N CP MAS solid state NMR spectra were obtained using Bruker CXP-100 and MSL-400 spectrometers with the magic angle set by using the ^{79}Br resonance of KBr.^[3] TMS and neat formamide were used as the references for ^{13}C and ^{15}N chemical shifts respectively.

2. SYNTHESIS OF ^{13}C AND ^{15}N LABELLED CYANATE FOR NMR STUDY:



+



-C* N^- represents $^{13}\text{C}^-\text{N}^-$ or $^{15}\text{N}^-\text{C}^-$

RESULTS

In the solid state ^{13}C NMR spectra (Figure 1) of BPADCN 1 monomer, the -OCN carbon gives rise to three peaks due to residual dipolar coupling to the directly bonded ^{14}N ($I=1$) quadrupolar nucleus, which are reduced but not eliminated by MAS.^[4] Figure 1D shows the CP/MAS spectrum with sidebands removed by the TOSS sequence^[5]. The spectrum obtained at 100 MHz (1D) is much cleaner as the three resonances have become almost degenerate because the quadrupolar coupling is greatly reduced at the higher frequency.

The ^{15}N NMR spectrum (Figure 2A) of the labelled BPADCN 1 monomer shows two sharp

resonances, indicating a site symmetry lower than the symmetry of the isolated molecule in solution (also reflected by the two methyl resonances in the ^{13}C NMR spectrum (Figure 1A).

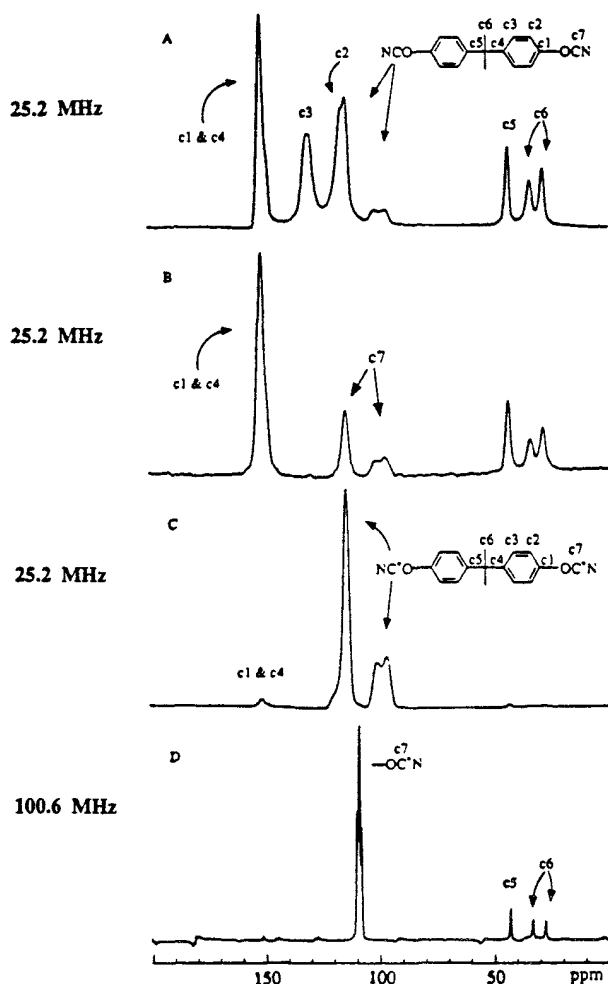


Figure 1. Solid state ^{13}C CP/MAS NMR spectra of (A) natural abundance BPADCN monomer at 25.2 MHz, (B) natural abundance BPADCN monomer using the NQS sequence at 25.2 MHz, (C) the ^{13}C enriched BPADCN monomer using the NQS sequence at 25.2 MHz, and (D) the ^{13}C enriched BPADCN monomer using the TOSS sequence at 100.6 MHz.

Figures 2B-D show ^{15}N spectra of the solid obtained from the solution curing process. The intensity of the species at high field is greatly enhanced by the cross polarization process.

Because there are protons directly attached to the ^{15}N nucleus in this case and this interaction relatively depends on $1/r^6$, which will extremely affect the spectrum obtained with short contact time.

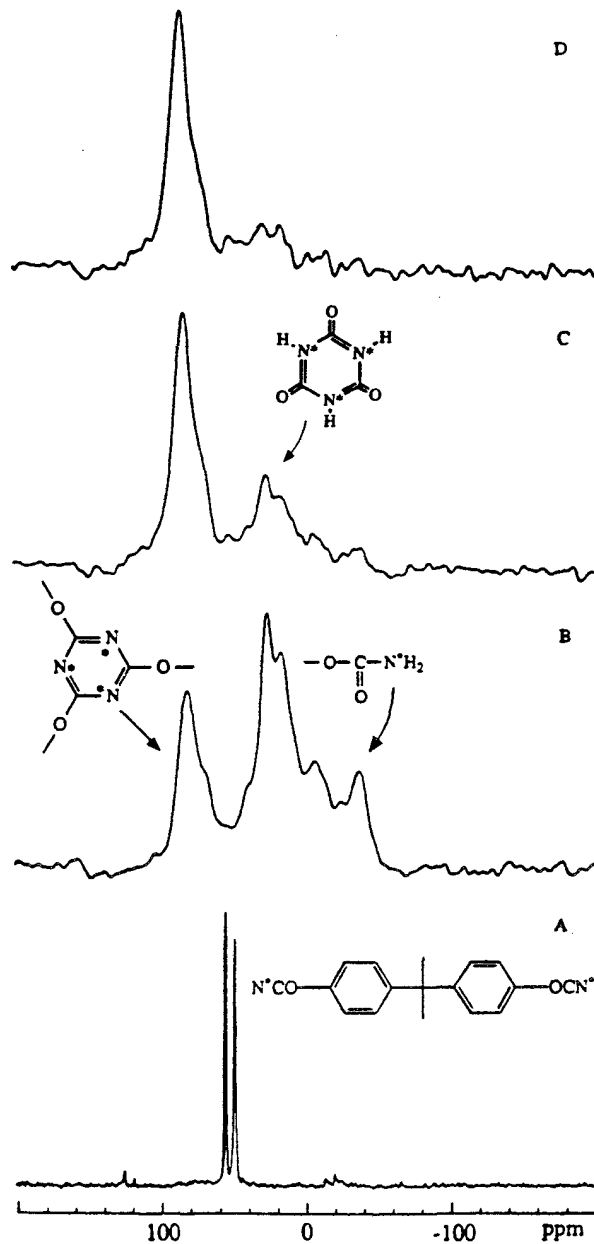
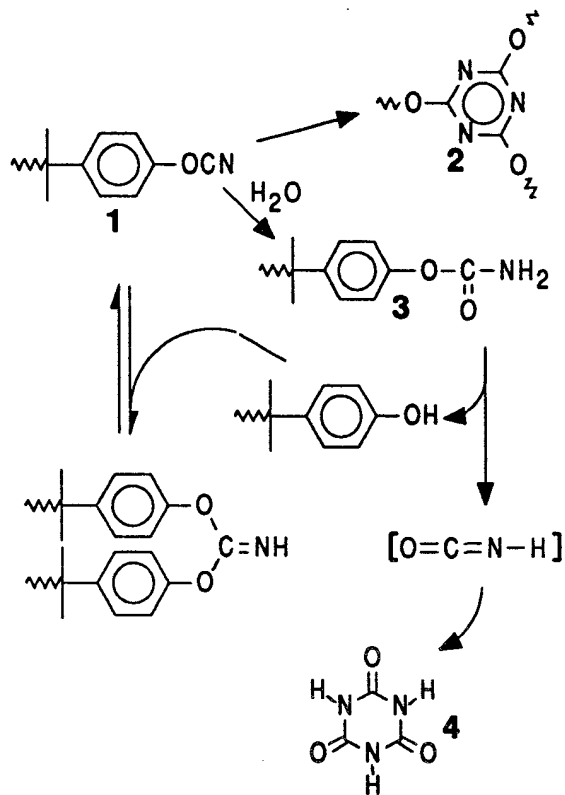


Figure 2. ^{15}N solid state CP/TOSS/MAS NMR spectra at 40.6 MHz of (A) the ^{15}N enriched BPADCN monomer, (B) the solid sample obtained by evaporation of the solvent after curing the ^{15}N enriched BPADCN in MEK and acetone- d_6 at 110 C

for 1 day, contact time 1 ms, (C) and (D) spectra of the same sample as in (B), but with contact time 5 ms and 10 ms respectively.

In the solution curing process, besides the main triazine product **2**, ^{13}C and ^{15}N NMR studies on model compounds show that the cyanate also reacts with H_2O present in the solvent to produce carbamate **3**, cyanuric acid **4**, and phenol side products.



The curing reaction in bulk is much more efficient than that in solution. In the bulk curing, only the triazine product formed from three cyanate groups is observed. There is no evidence of formation of any dimer or other intermediates. To quantify the efficiency of the curing reaction in the bulk, a series of ^{13}C and ^{15}N NMR spectra with contact time variation and no sideband suppression were obtained (Figure 3). The spectra show that more than 95% of the cyanate functional groups are converted to triazine rings during curing, a remarkably efficient process.

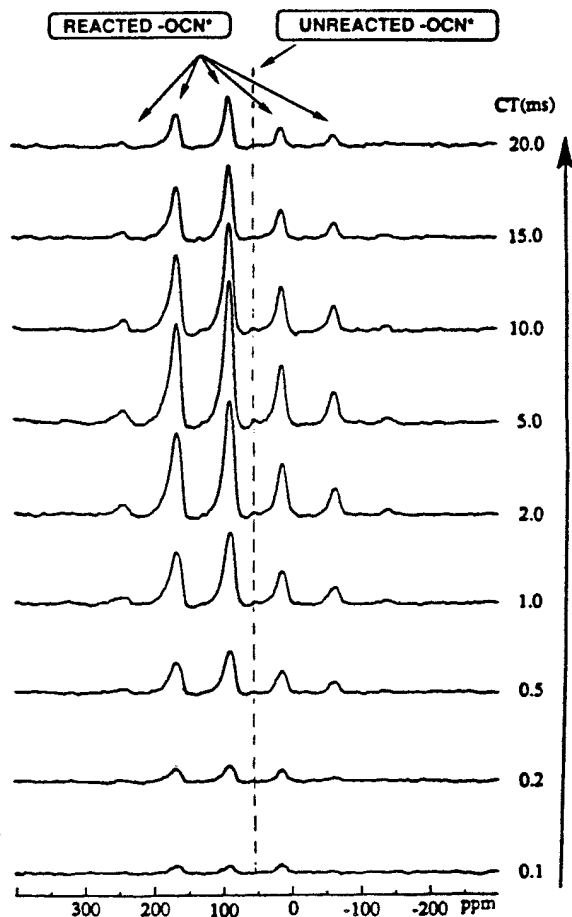


Figure 3 Series of ^{15}N solid state NMR spectra with variation of the contact time (CT) using the CP/MAS sequence only without sideband suppression. The resin sample was obtained by bulk curing a mixture of 50% ^{13}C enriched and 50% ^{15}N enriched BPADCN monomer at 180 °C for 30 minutes.

The high efficiency of the curing reaction in the bulk can be rationalized in terms of the very strong intermolecular interaction between the cyanate groups in different molecules observed in the crystal structure of the bisphenol A dicyanate monomer obtained from a single crystal X-ray diffraction experiment (Figure 4).

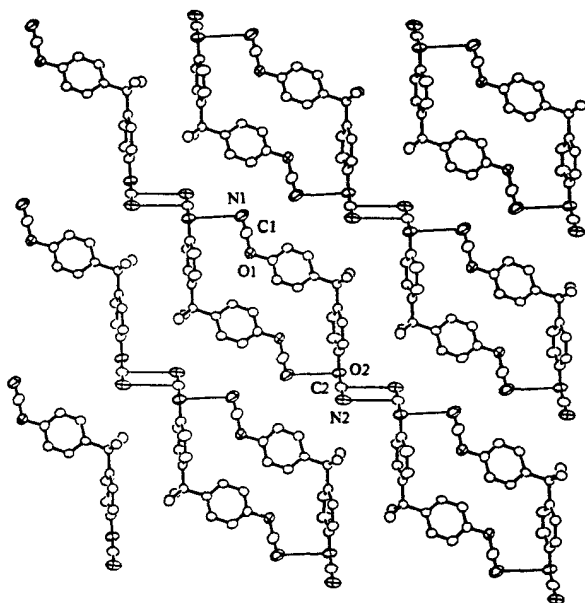


Figure 4. The intermolecular interaction diagram in the BADCN crystal.

In the crystal, the packing of the molecules is determined by intermolecular interactions between cyanate groups. The cyanate groups needed to form a triazine ring are very close to each other with very strong interactions between two of them forming a four membered ring (Figure 4), which could play an very important role in the ultimate formation of the triazine ring. Although melting the sample will disrupt the ordering pattern, it is expected that strong interactions between cyanate groups will still occur and substantial local ordering may persist in the molten state to facilitate the cyanate curing reaction.

REFERENCES

- [1] Wang, D. W. in "Electronic Packaging Materials Science III" edited by Jaccodine, R.; Jackson, K. A.; and Sundahl, R. C.; Nat. Res. Soc. Symp. Proc., 108, 125 (1988).
- [2] Shimp, D. A.; Christenson, J. R.; and Ising, S. J.; Proc. 34th Intl. SAMPE Symp., 34, 222 (1989).
- [3] Frye, J. S.; and Maciel, G. E.; J. Mag. Res., 48, 125 (1982).
- [4] (a). Zumbulyadis, N.; Henrichs, P. M.; Young, R. H.; J. Chem. Phys., 75, 1603 (1981). (b).

Bohm, J.; Fenzyke, D.; Pfeiffer, H.; J. Mag. Res., 55, 197 (1983). (c). Naito, A.; Ganapathy, S.; McDowell, C. A.; J. Chem. Phys., 74, 5393 (1981). (d). Naito, A.; Ganapathy, S.; McDowell, C. A.; J. Mag. Res., 48, 367 (1982).

[5] Dixon, W. T.; J. Mag. Res., 49, 341 (1982).

³¹P NMR STUDY ON PHYTASE - CATALYZED HYDROLYSIS OF PHYTATE

E. Brosio*, E. Carnovale**, M. Delfini*, L. Pizzoferrato**, G. Veglia*

* Dipartimento di Chimica, Università di Roma (La Sapienza)
P.le A. Moro 5 - 00185 Roma (Italy)

** Istituto Nazionale della Nutrizione
via Ardeatina 546 - 00178 Roma (Italy)

1 Abstract

Phytase provides inorganic phosphate from phytate (myo-inositol hexaphosphate) during seed germination. In the present study the enzymatic hydrolysis of phytate in an isolated system has been investigated by ³¹P Nuclear Magnetic Resonance (NMR).

The ³¹P NMR seems to be very a suitable method to follow, directly in the NMR tube, the fate of the different hydrolysis products of phytate. The method is highly specific. All the resonance signals of the phosphorylated species deriving from inositol-exa-phosphate can be assigned.

2 Introduction

Phytase, or myo inositol hexaphosphate phosphorylase, is widely distributed in plant and animal tissues. The main function of phytase in seed is to provide inorganic phosphate from phytate (myo-inositol hexaphosphate) during germination [1]. The first product of phytate hydrolysis can be identified as inositol pentaphosphate, but with increasing time, lower inositol phosphates have also been identified.

In the present study the enzymatic hydrolysis of phytate in an isolated system has been investigated by ³¹P Nuclear Magnetic Resonance (NMR). The time and temperature dependence of phytate and hydrolysis product has also been studied.

3 Experimental

Materials

Phytic acid dodecasodium salt and the phytase enzyme preparation (0.04 U/mg), crude from wheat, were purchased from Sigma Chemical Co (St. Louis, MO). EDTA was from Carlo Erba (Milano, I).

Distilled water was purified using a Milli-Q Ion Exchanger (Millipore).

Samples

The phytate solution (80mg/ml), containing EDTA (12 mg/ml), was prepared in deionized water and the pH was adjusted to 5.0.

The samples for analysis were prepared directly in NMR tubes by mixing the phytate solution with the same volume of a phytase solution (20mg/ml).

NMR measurements

High resolution ³¹P-NMR spectra, broad band decoupled from protons, were obtained at 202.4 MHz on a Bruker AM 500 spectrometer using the following parameters: spectral width 10,000 Hz; number of data points 16K; pulse width 5μsec (40°); number of acquisition 16; interpulse delay 4 sec.

The ³¹P chemical shifts were measured with reference to an external standard of dimethyl-methylene-phosphonic acid (DMP) 0.1M in Tris-HCl 0.2M, pD=8.9.

The concentration of each enzymatic degradation product was measured from the area of the best resolved assigned peak.

4 Results and Discussion

³¹P NMR spectra of phytase-phytate solutions were measured at time intervals of 0.5 hrs. As an example, ³¹P NMR spectra measured at 50°C for 0, 2 and 16 hours of hydrolysis are reported in Fig.1.

The spectrum measured at t=0 makes evidence of the four resonance signals of phytate. New resonance signals appear after the addition of the phytase solution, while the intensities of the initial four resonances decrease.

All the resonance signals of the phosphorylated species can be assigned.

In Fig. 2 the time dependence of phytate and hydrolysis product concentrations measured at 50°C is reported. The curve trend of hexa and penta phosphate seems to be related to a consecutive reaction kinetics, according to the following scheme:



The relevant differential equations are:

$$-d[\text{hexa}]/dt = K_1[\text{hexa}]$$

$$-d[\text{penta}]/dt = -K_1[\text{hexa}] + K_2[\text{penta}]$$

$$d[\text{tetra}]/dt = K_2[\text{penta}]$$

with the solutions:

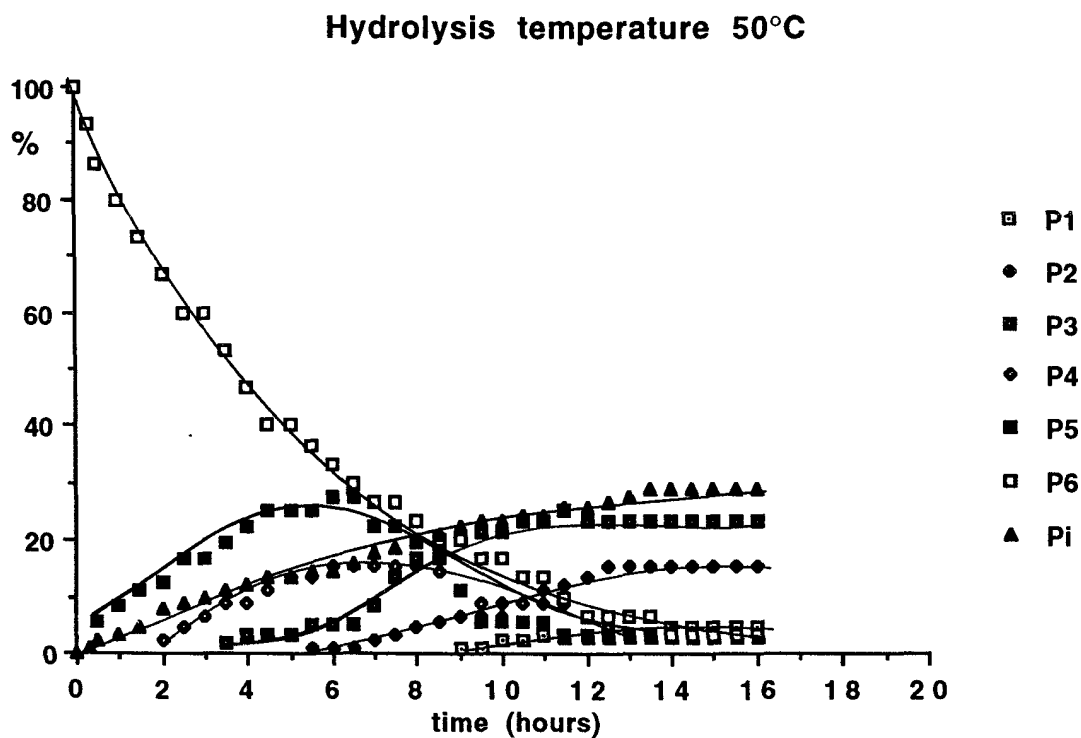
$$a) \quad [\text{hexa}] = 100 \exp(-K_1 t)$$

$$b) \quad [\text{penta}] = \left[\frac{100K_1 \exp(K_2 - K_1)t}{(K_2 - K_1)} - \right.$$

$$\left. \frac{100K_1}{(K_2 - K_1)} \right] \exp(-K_2 t)$$

A non linear least-squares fitting of experimental curves by eq. a) and b) enables to find the kinetic constant of inositol hexa and penta phosphate degradation.

Fig.2 Time dependence of concentration of phytate and hydrolysis products



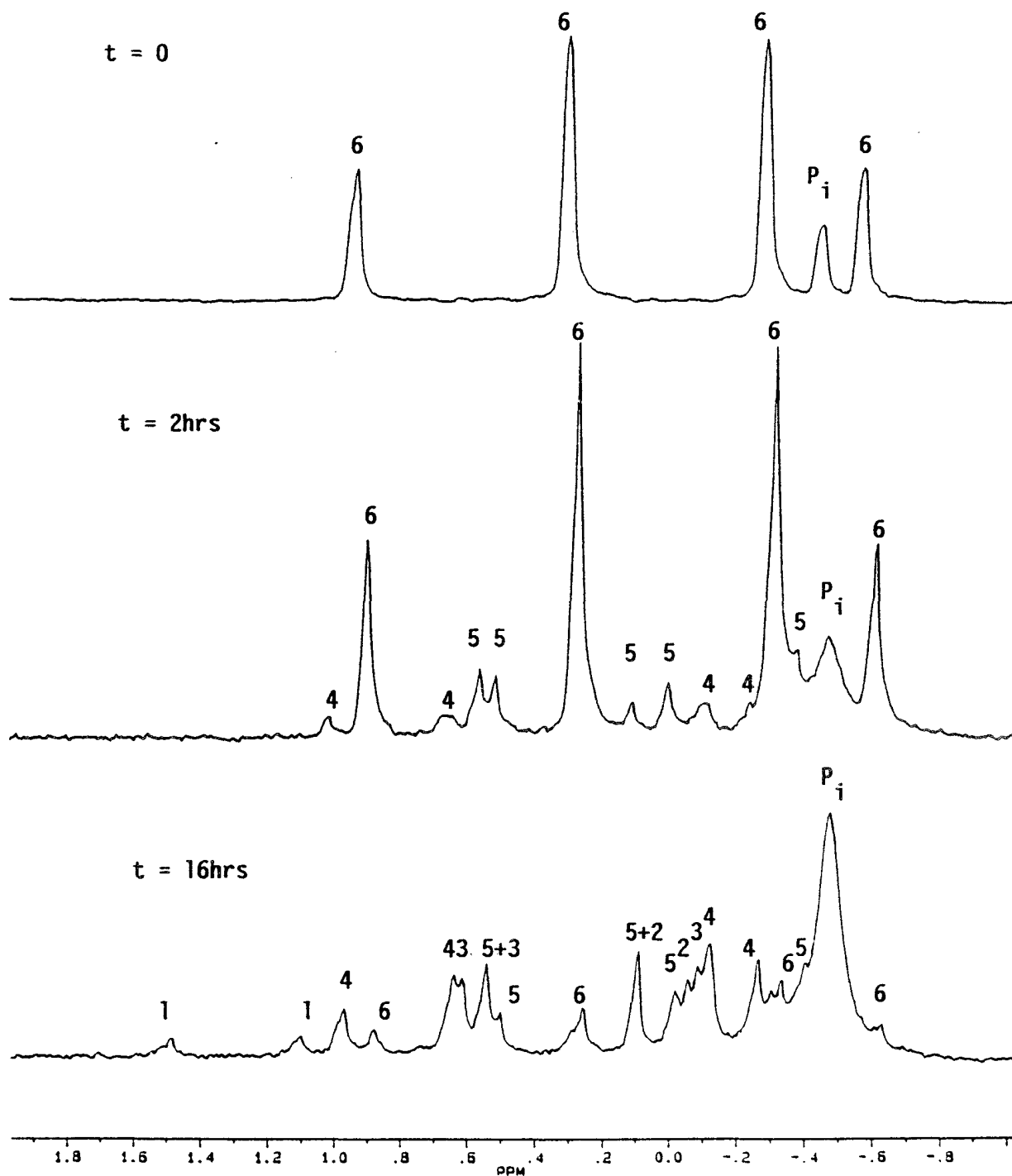


Fig. 1 ^{31}P NMR spectra measured at 50°C for 0, 2, 16 hours.

In Tab.1 the results obtained for two different temperatures of hydrolysis are reported.

Table 1. Enzymatic hydrolysis of phytate: kinetic parameters.

T (°C)	$K_1(\text{hr}^{-1})$	$K_2(\text{hr}^{-1})$
37	0.146 ± 0.003	0.306 ± 0.002
50	0.188 ± 0.003	0.438 ± 0.003

5 Conclusions

The ^{31}P NMR seems to be very a suitable and highly specific method to follow, directly in the NMR tube, the fate of the different hydrolysis products of phytate. The obtained results make evidence that, as the hydrolysis proceeds, different lower inositol phosphates are present in solution so that it seems unlikely that hydrolysis proceeds in a stepwise manner, as already reported by some Authors [2], [3]. In our experimental conditions the phytate hydrolysis seems to follow a consecutive reaction mechanism.

6 References

- [1] M.Torre, A.R.Rodriguez, F.Saura-Calixto, 1991, CRC Crit. Rev. Food Sci. Nutr., 1, 1-22
- [2] W.Frolich, T.Drakenberg, N.G. Asp, 1986, J. Cereal Sci., 4, 325-334
- [3] W.Frolich, M.Wahlgren, T.Drakenberg, 1988, J. Cereal Sci., 8, 47-53

Molecular Beam Magnetic Resonance via the Longitudinal Stern-Gerlach Effect

Leonard J. Mueller and Daniel P. Weitekamp

Arthur Amos Noyes Laboratory of Chemical Physics
California Institute of Technology, 127-72
Pasadena, CA 91125 USA

Contribution No. 8780

1 Introduction

Trigger methods have long been known to increase the sensitivity of magnetic resonance by the detection of energies far greater than those of magnetic resonance transitions. Sensitivity is also increased when a magnetic resonance signal is proportional to the number of spin flips in either direction and does not rely on population differences within the sample. Perhaps the most celebrated trigger method is the Rabi experiment,^{1,2} which detects spin flips as changes in the flux of a molecular beam by combining two opposing Stern-Gerlach deflecting regions with resonant excitation in a central homogeneous magnetic field. In the absence of a spin transition, the second Stern-Gerlach deflection magnet refocuses a particle in a plane perpendicular to the beam direction, while a spin transition causes the refocusing onto the detector to fail. A magnetic resonance spectrum is then recorded as the intensity at a detector as a function of the excitation frequency.

In this paper we propose a sensitive new technique for magnetic resonance by detection of the flux of molecules within a molecular beam. In contrast to the Rabi experiment, which relies on spin-dependent beam deflection, our method uses the longitudinal Stern-Gerlach (LSG) effect,^{3,4,5,6,7,8} the change in a particle's velocity due to the interaction of its spin magnetic moment with a magnetic field and field gradient aligned along the beam axis. This has the experimental advantage of requiring no other gradients except those encountered along the axis of a standard solenoid. A novel arrangement of slotted disk velocity selector plates has been designed that converts small spin-dependent accelerations in this velocity component into beam flux changes, while maintaining higher throughput than conventional velocity selection.

Another advantage of the longitudinal Stern-Gerlach experiment is that it is applicable to charged particles.^{9,10} If one attempted to perform the traditional Stern-Gerlach experiment on ions, with the magnetic field perpendicular to the initial ion beam direction, this transverse momentum would be wrapped around into cyclotron motion, leaving only the longitudinal momentum to be substantially affected by spin dependent forces, as in the LSG experiment. The LSG experiment for ions can be accurately described by considering the motion of the center of the cyclotron orbit (guiding center) from source to detector. The longitudinal field gradients interact with the spin magnetic moment, as before, with a slight complication due to the added interaction of the constant mechanical magnetic moment associated with the ion cyclotron motion.

2 The Longitudinal Stern-Gerlach Experiment

The potential energy of a particle possessing a spin magnetic moment μ in a magnetic field \mathbf{B} is $V = -\mu \cdot \mathbf{B}$. For an eigenstate $|m\rangle$ of this interaction, there is a force $F_m = -\nabla \langle m | V | m \rangle = \gamma \hbar m G$, where G is the gradient in the field direction. Depending on the sign of the spin projection m , this force will either increase or decrease the component of the particle's velocity in the field direction. On the way out of the magnetic field the gradient has opposite sign, and the particle will be returned to its initial velocity. If a particle undergoes a single-quantum spin flip while in the homogeneous region of the magnetic field, m is changed by one, and the force on the particle is no longer equal and opposite. Thus the particle leaves the magnetic field moving faster or slower, depending on its initial spin state, relative to the velocity with which it

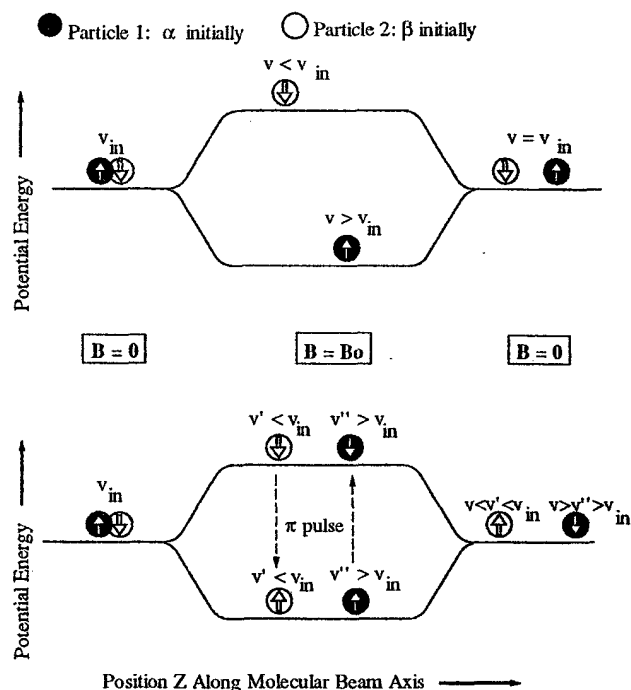


Figure 1: The longitudinal Stern-Gerlach (LSG) experiment for spin- $\frac{1}{2}$ particles. (top) The particles change velocity according to their spin states as they enter the magnetic field, but are returned to their initial velocities as they exit. (bottom) If the particles undergo a spin flip while in the magnetic field region they change potential surfaces. They now leave the magnetic field region moving faster or slower than when they entered.

entered. This experiment is illustrated for the case of spin- $\frac{1}{2}$ particles in Figure 1.

3 Detection Schemes

The fundamental barrier to exploiting this LSG effect for the detection of magnetic resonance of beam species is that the spread in velocities for a typical molecular beam is much larger than velocity changes resulting from these spin transitions. Mechanical velocity selection via a slotted disk velocity selector (SDVS)^{11,12} can be used to narrow the incoming velocity distribution. An SDVS consists of several displaced disks with radial slots rotating synchronously. For a particle to pass through the selector it must arrive at each disk at the proper time, defining its velocity, as shown in Figure 2. In scattering applications a single velocity is selected, leading to low throughput.

We have designed a novel three disk SDVS that allows for the detection of small kinetic energy changes while allowing a relatively large fraction of the velocity distribution to pass.¹³ In our arrangement, the second disk passes many narrow velocity ranges and the third disk is positioned to allow passage of only those particles whose velocities have changed while in the region between the

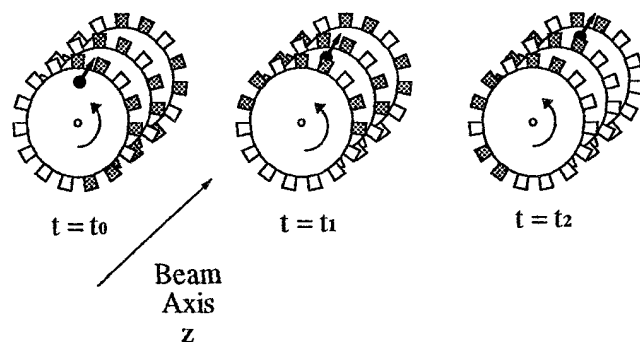


Figure 2: The slotted disk velocity selector (SDVS). An SDVS consists of several displaced disks with radial slots rotating synchronously. For a particle to pass through the selector it must arrive at each disk at the proper time, defining its velocity.

second and third disks. Thus, the net effect is to select for acceleration, rather than velocity.

4 The Longitudinal Stern-Gerlach Magnetic Resonance (LSG-MR) Experiment

The experimental setup for the LSG-MR experiment is shown in Figure 3. The symmetric arrangement of the magnetic field about disk 2 ensures that other magnetic moments that are invariant (spin, orbital, or rotational magnetic moments) do not contribute to the difference in time of flight for the two intradisk regions. In this way, only the changes in transit time due to a spin flip between disks two and three are detected. For spin-flip-induced velocity changes that are small compared to the initial velocity, the change in arrival time associated with a spin flip is proportional to the spin magnetic moment and the magnetic field, and inversely proportional to both the mass

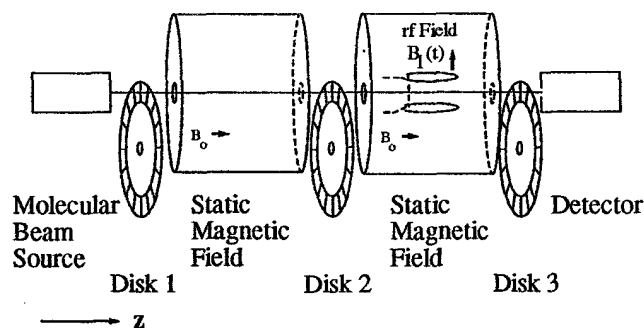


Figure 3: The longitudinal Stern-Gerlach magnetic resonance experiment. The SDVS disks are positioned such that only particles that spend a different amount of time in the region between disks two and three than in the region between disks one and two go on to the detector. For magnetic resonance, this difference in time of flight is due to the change in velocities associated with a spin flip.

of the particle and the cube of its initial velocity. The time-of-flight resolution is determined by the slot spacing and rate of disk rotation.

A detailed sensitivity analysis has been performed taking into account beam flux, SDVS throughput, detection efficiency, and background counts.¹³ We define the signal for this experiment as $S = \frac{N_{rf} - N_o}{N_{rf} + N_o}$, where N_{rf} is the

number of particles detected during radiofrequency excitation and N_o is the number of particles detected in the absence of a resonance. Both N_{rf} and N_o contain pressure dependent background counts. The signal-to-noise ratio, determined by counting statistics, is

$$\frac{S}{N} = \frac{(N_{rf} - N_o)\sqrt{N_{rf} + N_o}}{2N_o}$$

Given typical modern molecular beam, magnet, and SDVS technology, it is calculated that proton NMR will be feasible up to a mass of 750 amu with a signal-to-noise ratio of $3\sqrt{t_d/s}$, where t_d is the time during which particles are detected. For lighter particles, signal-to-noise ratios of over $300\sqrt{t_d/s}$ are predicted. Electron spin resonance will be feasible to much higher mass, limited primarily by the ability to volatilize large molecules.

5 A Stern-Gerlach Experiment for Ions

For ions the most direct analogs of the Stern-Gerlach experiment are impractical, since the transverse momentum of the ion (perpendicular to the static field) is converted into cyclotron oscillation around a field line. If the ion beam is parallel to the static field, spin-dependent longitudinal acceleration (the LSG effect) is possible, but is coupled to the larger mechanical magnetic moment associated with the cyclotron motion. This mechanical magnetic moment is a constant of motion,¹⁴ however, and the symmetric nature of the LSG-MR experiment causes the effect of its interaction with the magnetic field gradients to cancel. There are several other new issues that arise when using ions in the LSG experiment: 1) ions may be reflected by the magnetic field; 2) the collision cross section with the chopper will be dominated by the cyclotron radius rather than the van der Waals radius, leading to a lower transmittance of ions; and 3) ion-ion interactions are long range and may cause velocity changes larger than the spin dependent energy changes, thus limiting the beam flux.

We have solved the equations of motion for a radially symmetric field that approximately models a 5 Tesla solenoid, with or without a spin flip at the center. The velocity selection scheme is similar to that described for neutrals above. Numerical simulations using conservative experimental parameters show that nuclear magnetic resonance on ions up to a mass of 100 amu should be possible with a signal-to-noise ratio of $3\sqrt{t_d/s}$. For

lighter ions, signal-to-noise ratios of over $10\sqrt{t_d/s}$ are expected. Again, ESR will be feasible to much higher mass.

LJM acknowledges an NSF Graduate Fellowship and a DoD National Defense Science and Engineering Graduate Fellowship. DPW is a Camille and Henry Dreyfus Teacher-Scholar. This work was supported in part by the National Science Foundation (CHE-9005964).

¹I.I. Rabi, J.R. Zacharias, S. Millman, and P. Kusch, *Phys. Rev.* **53**, 318 (1938).

²I.I. Rabi, S. Millman, P. Kusch, and H.R. Zacharias, *Phys. Rev.* **53**, 526 (1939).

³G.M. Drabkin and R.A. Zhitnikov, *JETP* **38**, 1013 (1960).

⁴S. Funahashi, *Nucl. Instrum. Methods* **137**, 99 (1976).

⁵B. Alefeld, G. Badurek, and H. Rauch, *Phys. Lett.* **83A**, 32 (1981).

⁶H. Weinfurter, G. Badurek, H. Rauch, and D. Schwahn, *Z. Phys. B - Condensed Matter* **72**, 195 (1988).

⁷J. Schwinger, M.O. Scully, and B.-G. Englert, *Z. Phys. D - Atoms, Molecules and Clusters* **10**, 135 (1988).

⁸Ch. Miniatura, F. Perales, G. Vassilev, J. Reinhardt, J. Robert, and J. Baudon, *J. Phys. II* **1**, 425 (1991).

⁹The Stanford Low Temperature Physics Group used the LSG effect to produce ground state electrons. See F.C. Witteborn, Ph.D. Thesis, Stanford University, Stanford (1965). Efforts to confirm their observations by other groups, however, have been unsuccessful. See J. Kessler, *Polarized Electrons*, 2nd. ed. (Springer, New York, 1985).

¹⁰For charged particles in bound orbits within electromagnetic traps other applications of spin dependent forces can be used. Dehmelt measured the *g*-value of a trapped electron using the "continuous Stern-Gerlach effect." R.S. Van Dyck, Jr., P.B. Schwinberg, and H.G. Dehmelt, in *New Frontiers in High Energy Physics*, edited by B. Kursunoglu, A. Perlmutter, and L. Scott (Plenum, New York, 1978); in *Atomic Physics 9*, edited by R.S. Van Dyck, Jr. and E.N. Fortson (World Scientific, Singapore, 1984). Pizarro and Weitekamp have proposed a magnetic resonance experiment for trapped molecular ions: P.J. Pizarro and D.P. Weitekamp, *Bull. Mag. Res.* **14**, 220 (1992).

¹¹C.J.N. van den Meijdenberg in *Atomic and Molecular Beam Methods*, Vol. 1, edited by G. Scoles (Oxford, New York, 1988).

¹²S.M. Trujillo in *Electronic and Atomic Collisions*, Vol. 2, edited by J.S. Risely and R. Geballe, (University of Washington Press, Seattle and London, 1975).

¹³L.J. Mueller and D.P. Weitekamp, to be published.

¹⁴G. Schmidt, *Physics of High Temperature Plasmas*, 2nd. ed. (Academic Press, New York, 1979).

Fourier-Transform Time-Sequenced Optical Nuclear Magnetic Resonance of Gallium Arsenide

S.K. Buratto, J.Y. Hwang, N.D. Kurur, D.N. Shykind, and D.P. Weitekamp

Arthur Amos Noyes Laboratory of Chemical Physics
California Institute of Technology, 127-72
Pasadena, CA 91125 USA

Contribution No. 8796

1 Introduction

Optical nuclear polarization (ONP) and optical detection (OD) of nuclear magnetic resonance (NMR) in III-V semiconductors have proven to be effective methods for increasing the sensitivity of NMR over that of conventional methods.¹ These two processes address the fundamental problems responsible for the low sensitivity of conventional NMR: the small population difference between nuclear spin levels and the difficulty in detecting radiofrequency photons above the thermal noise. The combination of ONP and OD into one optical NMR experiment has led to sensitivity enhancements of at least 10^5 in several GaAs-based materials such as epitaxially grown $\text{Ga}_{1-x}\text{Al}_x\text{As}^2$ and GaAs^3 , as well as $\text{GaAs}/\text{Ga}_{1-x}\text{Al}_x\text{As}^4$ heterojunctions and quantum wells.^{5,6} The quasi steady-state optically detected NMR (ODNMR) method used in all of these studies have resulted in NMR lineshapes which were either distorted by the high rf fields needed to see signals or broadened by the presence of spin-polarized electrons during NMR.

Recently, we demonstrated in GaAs a new method of optical NMR in which ONP, nuclear spin resonance, and OD are separated into distinct sequential periods which can be separately optimized for sensitivity and resolution.⁷ This

time-sequenced optical NMR (TSO-NMR) technique results in order-of-magnitude improvements in sensitivity and resolution over the previous steady-state ODNMR method, where these processes are simultaneous. In addition to improvements in sensitivity and resolution, time-domain experiments are also possible with the TSO-NMR technique, putting all of the well established techniques of multiple-pulse and multidimensional NMR at the disposal of optical NMR. We have performed both the cw and Fourier transform variants of the TSO-NMR experiment on two nominally similar epitaxial p-type GaAs samples both doped with Zn acceptors at a concentration of $10^{17}/\text{cm}^3$.

2 Time-sequenced Optical NMR

The general timing sequence for a TSO-NMR experiment is: (i) ONP until a steady-state nuclear spin polarization is achieved, (ii) a period of NMR to selectively modulate nuclear spin order, and (iii) OD to sensitively assess this modulation. During the ONP period of the TSO-NMR experiment, the sample is irradiated with circularly-polarized light near the band gap energy in a magnetic field along the optical (z) axis. The excited electrons are polarized by a transfer of photon angular momentum to the excited electron.

The resulting steady-state electron polarization is given by

$$\langle S \rangle = \frac{C}{1 + \tau / \tau_s}$$

where τ is the recombination lifetime, τ_s is the electron spin-lattice relaxation time, and C is a constant which depends on the selection rules of the transition. For bulk GaAs, $C = 0.5$ due to the valence band ($J = 3/2$) degeneracy of the heavy-hole ($m_j = \pm 3/2$) and light-hole ($m_j = \pm 1/2$) subbands at $k=0$. In a quantum well, the degeneracy is removed and the heavy-hole transition can be selected, giving $C = 1.0$ ^{1,8}.

Nuclear spins are then polarized through hyperfine-modulated cross-relaxation with the spin-polarized conduction electrons, as in the Overhauser effect. The cross-relaxation is most efficient for nuclei near localized electrons. In bulk p-type samples, the conduction electrons are localized on defect sites of unknown identity, called optically relevant defects (ORDs). The steady-state nuclear spin polarization is proportional to the electron spin polarization and occurs within the region of carrier localization and in adjoining regions within the range of spin diffusion through nuclear spin-spin couplings. The length scale of both localization and spin diffusion during the several seconds of the experiment can be estimated to be ≈ 10 nm. The nuclear spin polarization $\langle I \rangle$ is detected as a hyperfine-weighted average, called the nuclear field B_n , which acts on the electrons.

Once a steady-state nuclear field is established, its value can be changed with NMR. The power of the TSONMR technique comes from the flexibility in the type of NMR experiment that can be performed. The NMR of the valence band can be measured by turning off the light. In this manner the resolution is maximized because NMR is performed in the absence of spin polarized photocarriers, which degrade spectral resolution. The rf field can be applied in a cw fashion or as a series of pulses and delays, the latter of which is more versatile, as evidenced by modern time-domain NMR spectroscopy.

The nuclear field resulting from NMR is then optically detected through a type of Hanle effect.¹

To optimize this process, the nuclear field is first adiabatically rotated to a direction x perpendicular to the optical z axis by rotating the DC field. Restoring the band-gap light causes the newly-created photocarrier spins to precess in the field

$B_T = B_n + B_o^d$, where B_o^d is the applied field during optical detection. The polarization of the recombination luminescence, $\rho = 2C^2 \langle S \rangle$, is determined by B_T and its variation is arranged to be linear in B_n .

3 Experimental Results

The experiments have been performed at 77K. In the CW-TSONMR experiment, the sample is irradiated with low-power rf at frequency ω which is stepped for each point. The CW-TSONMR spectrum for ⁷¹Ga consists of a single resonance with a linewidth of approximately 3 kHz⁹, the same width expected for spin-spin couplings alone.^{10,11} This indicates that although the ONP and OD processes are more strongly weighted by the nuclei near the ORD, which should exhibit quadrupole effects, the cw resonance is dominated by bulk spins. The importance of this result is that the TSONMR experiment can ultimately be used to detect any site in the irradiated volume and is not limited to the spins associated with the ORD. The absence of quadrupole-perturbed resonances in the cw spectrum is a motivation for time-domain experiments.

The Fourier-transform variant of the TSONMR experiment is performed by giving a sequence of two near-resonant rf pulses during the NMR period (Figure 1).

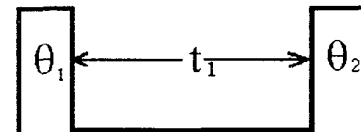


Figure 1. Pulse sequences for FT-TSONMR experiment. The FID (free induction decay) is acquired pointwise by stepping t_1 on successive repetitions.

The first pulse θ_1 puts the magnetization in the transverse plane, and the magnetization undergoes free evolution during t_1 . The second pulse stores

one transverse magnetization component along the z -axis for optical detection. The evolution time t_1 is incremented for successive points in the experiment. This FID is then Fourier-transformed with respect to t_1 to obtain the NMR spectrum.

Figure 2 shows the FT-TSONMR spectra of both sample A and B. A surprising difference between the FT and cw spectra is the broadening of the linewidth in the FT spectra by approximately 2 kHz. The FT spectra for the two samples are also quite different from each other. The spectrum of sample B not only shows broadening of the central transition, but also exhibits structure outside the main resonance not seen in the spectrum of sample A.

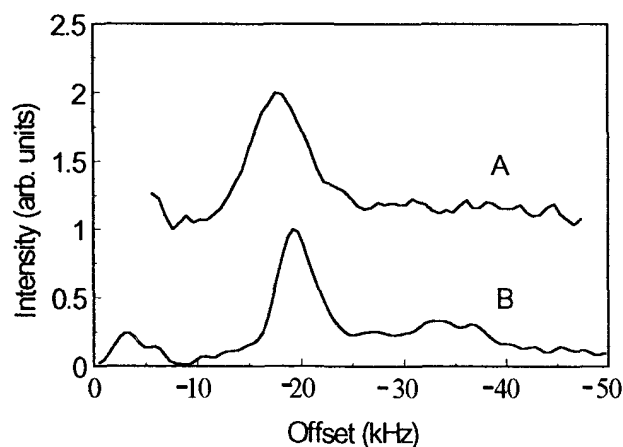


Figure 2. FT-TSONMR spectrum of ^{71}Ga . The abscissa gives the offset relative to 170 kHz. The carrier frequency for each spectrum corresponds to the left most data point. Both spectra were acquired with a 12.0 μsec , 90° pulse.

Another feature is the shift of the ^{71}Ga resonance in the FT spectrum of sample B relative to that of the FT spectrum of sample A and the cw spectrum of sample A and B. Due to the different time scales of the two experiments, the FT and cw experiment are sensitive to different spins. In the FT pulse sequence, which occurs in a time ≤ 1 msec, sites near the ORDs can contribute since spin diffusion from the more abundant bulk spins is less effective. In a cw experiment, the sample is irradiated for $\cong 100$ msec and unperturbed distant nuclei can effectively repolarize sites near the ORD, erasing their resonant depolarization.

To determine the nature of the broadening, a spin echo experiment with a π pulse at $t_1/2$ was

performed. The results of the echo experiment on A show little change in the linewidth.⁸ The spin-echo experiment in sample B results in a narrowing of the linewidth by approximately 3 kHz. The broadening of the linewidth in sample A, relative to the bulk linewidth, is thus dominated by first-order quadrupole satellites, which are not refocused by the spin-echo experiment. The narrowing of the central transition in sample B by the echo experiment indicates that the terms responsible are odd functions of I_z . The most likely mechanism is broadening due to the second-order quadrupole shift of the central transition. Such higher order quadrupole effects may also be the cause of the frequency shift of the spectral maxima in sample B.

The relative strength of the quadrupole coupling can be determined by a nutation experiment. A nutation TSONMR experiment uses a continuous pulse of length t_1 in the NMR period. The signal as a function of pulse length t_1 is then Fourier-transformed to give the nutation spectrum. The effective Rabi frequency for a spin $3/2$ nucleus with a quadrupole splitting $\omega_Q \gg \omega_1$ occurs at frequency $2\omega_1$. The nutation spectrum of sample B shows a peak at $2\omega_1$ indicating sites where $\omega_Q \gg 20$ kHz (Figure 3). The nutation spectrum of sample A, however, shows no such sites.

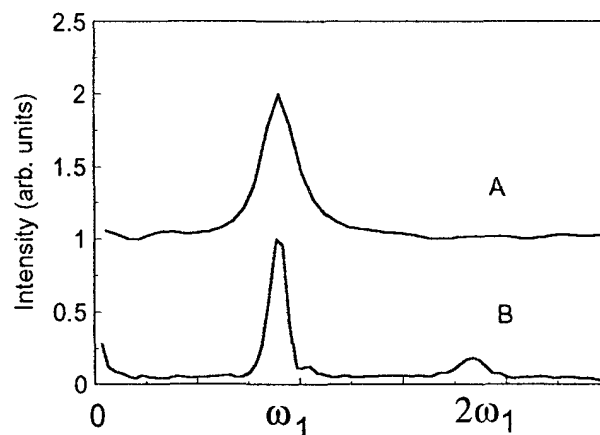


Figure 3. ^{71}Ga nutation spectra. The nutation frequency of sample A is $\omega_1 = 12$ kHz and that of sample B is $\omega_1 = 18$ kHz.

4 NMR of the ORD

The difference in the FT experiment of the two samples is presumably due to a chemical difference in the samples themselves. Although the two samples, from different sources, are nominally the same in terms of acceptor concentration, the defects which make up the ORDs are apparently different, leading to different FT-TSONMR spectra. The concentration of the donors which are the ORDs in high quality p-type material have been estimated to be ≤ 1 ppm ($\leq 10^{16}/\text{cm}^3$). Since NMR is a chemically specific technique, it should be possible to identify the ORD by its NMR spectrum. This can be likely be accomplished by combining our TSONMR experiment with double resonance methods well-established in conventional NMR.^{12,13,14}

The key to the success of such experiments is that the dipolar couplings have time to transfer spin order between species. The appropriate time constants, T_1 , T_{1d} and T_{1p} have all been measured using TSONMR, and the results are favorable for double resonance experiments. The T_1 for ^{71}Ga in sample B was measured by an inversion-recovery sequence and found to be 5.7 s. The spin relaxation time T_{1d} was measured to be 2.0 s in both zero field and at 15 mT by adiabatic demagnetization and remagnetization (after a variable delay) to B_d for optical detection. The relaxation time in the rotating frame, T_{1p} , was found to be 300 msec by a spin-locking TSONMR experiment. By using double resonance techniques with TSONMR, it will be possible to identify the ORD as well as obtain local structural information relevant to materials fabrication.

Conclusion

The ODNMR technique has been shown to provide dramatic enhancements in the sensitivity of NMR for the study of III-V semiconductors by a factor of 10^5 . However, these quasi-steady state ODNMR experiments suffer from distorted NMR lineshapes. The TSONMR technique has been shown to solve many of these problems and allows order-of-magnitude improvements in

sensitivity. However, the real power of this technique lies in the possibility of applying multipulse and multidimensional NMR to the optical detection of NMR. We have demonstrated FT variants of the TSONMR experiment.

FT spectra were obtained for two nominally similar samples A and B and differences were observed which were not present in the cw spectra. Sample B shows spectral evidence of strongly quadrupole perturbed sites, while sample A shows only weak first-order quadrupole broadening.

The differences between the FT and cw experiment are hypothesized to be the result of the sensitivity of the FT experiment to sites near the ORD and the cw experiment to sites distant from the ORD. One of the challenges of this new technique is to discover the identity of the ORD. We propose to accomplish this by combining the TSONMR experiment with the traditional NMR double resonance experiments. We have measured the relevant relaxation parameters and the results look favorable for double resonance experiments.

Acknowledgements: This research is sponsored by the Caltech Consortium in Chemistry and Chemical Engineering; founding members: E.I. du Pont de Nemours and Company, Inc., Eastman Kodak Company, and Minnesota Mining and Manufacturing. S.K.B. is an AT&T Bell Laboratories Ph.D. scholar. D.P.W. is a Camille and Henry Dreyfus Teacher-Scholar.

REFERENCES

1. For a review on optical pumping techniques in semiconductors, see *Optical Orientation*, ed. F. Meier and B.P. Zakharchenya (North Holland, Amsterdam, 1984)
2. A.I. Ekimov and V.I. Safarov, *ZhETF Pis. Red.* **15**, 453 (1972) [*JETP Lett.* **15**, 319 (1972)].
3. D. Paget, *Phys. Rev. B* **24**, 3776 (1981).
4. M. Krapf, G. Denninger, H. Pascher, G. Weimann, and W. Schlapp, *Solid State Comm.* **78**, 459 (1991).
5. G.P. Flinn, R.T. Harley, M.J. Snelling, A.C. Tropper, and T.M. Kerr, *J. of Lumines.* **45**, 218 (1990).

6. V.K. Kalevich, V.L. Korenev, and O.M. Fedorova, *Pis'ma Zh. Eksp. Teor. Fiz.* **52**, 964 (1990) [*JETP Lett.* **52**, 349 (1990)].
7. S.K. Buratto, D.N. Shykind, and D.P. Weitekamp, *Phys. Rev. B* **44**, 9035 (1991).
8. Twardowski, A., Hermann, C., *Phys. Rev. B* **35**(15), 8144 (1987).
9. S.K. Buratto, J.Y. Hwang, N.D. Kurur, D.N. Shykind, and D.P. Weitekamp, to be published.
10. R.G. Shulman, B.J. Wyluda, and H.J. Hrotowski, *Phys. Rev.* **109**, 808 (1958).
11. O.H. Han, H.K.C. Timken, and E. Oldfield, *J. Chem. Phys.* **89**, 6046 (1988).
12. S.R. Hartmann and E.L. Hahn, *Phys. Rev.* **128**, 2042 (1962).
13. F.M. Lurie and C.P. Slichter, *Phys. Rev.* **133**, A1109 (1964).
14. R.E. Slusher and E.L. Hahn, *Phys. Rev.* **166**, 332, (1968).

NMR Characterization of the Homopolymers and Copolymers formed from Tetraethoxysilane and Methytriethoxysilane In a Sol-Gel Process

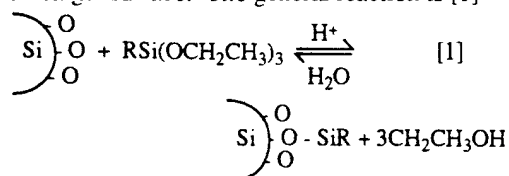
C. A. Fyfe, P. P. Aroca ; Y. Zhang

Dept. of Chemistry, Univ. of British Columbia, Vancouver, Canada, V6T 1Z1

1. INTRODUCTION

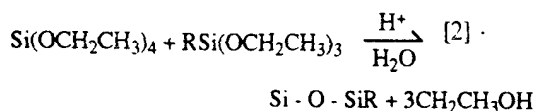
Immobilized reagents are widely used for improved control of reactions and products, and the removal and/or reuse of toxic and/or expensive compounds.¹ Often the reagents of interest are immobilized onto silica gel which is inert, inexpensive, non-swelling and has a high surface area.

The conventional preparation of organofunctionalized silica gels involves condensation of a functionalized silane onto a silica gel surface. The general reaction is [1]



where R is the functionality. A drawback to this reaction is that the presence of water promotes self condensation of the functionalized monomer resulting in polymeric species where there is no guarantee that their functionalities will be accessible.

In this work, an alternative approach to the preparation of organofunctionalized gels is presented. This involves the direct copolymerization of tetraethoxysilane (TEOS) and methyltriethoxysilane (MTES), reaction [2].



Methyl groups were used in this study to model the organic functionality. The optimization of this copolymerization would maximize the random distribution of the functionalities throughout the polymer, improving their potential efficiency. The nature of the copolymerization process was studied using both high-resolution solution and MAS solid state NMR.

2. NMR EXPERIMENTS

All the MAS solid state NMR experiments were carried out on a Bruker MSL-400. The high resolution solution kinetic work was carried out on a Bruker AMX-500. In both cases the reference, for the ²⁹Si resonance is tetramethylsilane.

3. RESULTS AND DISCUSSION

A) 1D ²⁹Si CP/MAS EXPERIMENTS

Figure 1 shows the ²⁹Si 1D CP/MAS spectra of MTES anchored onto the silica gel (top), the MTES/TEOS copolymer (middle) and a mechanical mixture of TEOS and MTES homopolymers (bottom). In all three cases, the regions due to the two monomers can be clearly distinguished. The three low field absorptions are due to Si(OSi)₄; Si(OH)(OSi)₃ and Si(OH)₂(OSi)₂ from TEOS, the different ratios providing an indication of the amount of surface hydroxyl groups present. A parallel scenario is true for the upfield MTES. Other than differences in intensities, the spectra are identical.

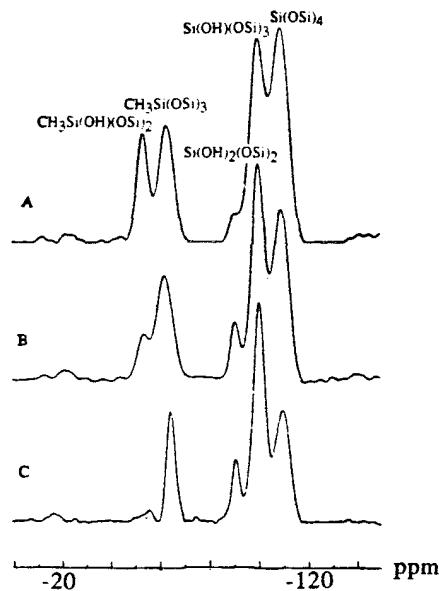


Figure 1. 1D ²⁹Si CP/MAS NMR Experiments

Any small differences in the chemical shifts, due to the different chemical environments in the three samples, are obscured by the broadness of the lines and the samples cannot be differentiated by chemical shifts alone. In all cases the two monomers remained intact but the extent of mixing or phase separation can not be addressed by 1D spectra.

B) 2D Heteronuclear Correlation CP Experiments

The aim of these 2D experiments is to determine whether the system is phase separated or "mixed" by studying the spatial proximity of the MTES methyls to the ^{29}Si signal in TEOS. The pulse sequence, Figure 2, involves cross polarization from ^1H to the dilute ^{29}Si spins ².

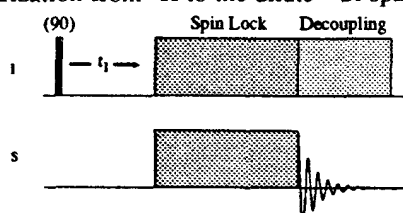


Figure 2 Pulse Sequence for 2D CP

Cross polarization is dependent on the dipolar interaction between these two nuclei. Which is inversely proportional to the cube of the distance between the two spin reservoirs. Consequently, if there is a correlation between the ^1H in the methyl groups and the silicon in TEOS, the system is mixed, not phase separated.

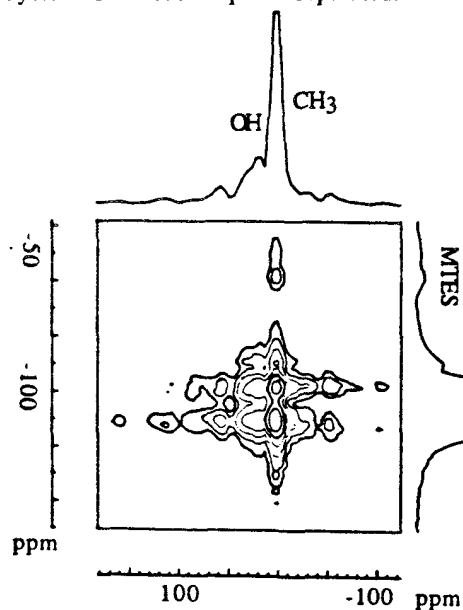


Figure 3 2D $^1\text{H}/^{29}\text{Si}$ CP/MAS Experiment on the Copolymer Gel.

It is clearly seen from Figure 3 that the copolymer made by the copolymerization preparation is "mixed", not phase separated.

C) KINETICS

To assess the extent of mixing, the hydrolysis and dimer formation reactions were investigated in solution, on the assumption that the extent of mixed dimer formation is an indicator of the degree of mixing. As illustrated in Figure 4 for the TEOS system all of the intermediate products formed in the hydrolysis and dimer formation are clearly differentiable and quantifiable, the same is true for the MTES system.

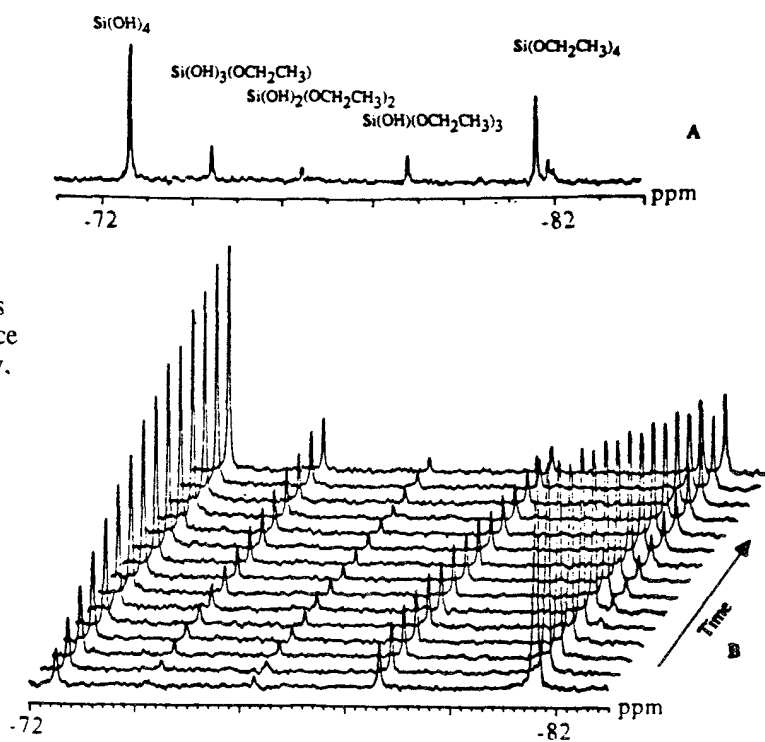


Figure 4 1D ^{29}Si NMR of the polymerization of TEOS with water acidified to $\text{pH}=2.33$
A - 1D spectrum with the peaks assigned
B - Collection of 1D spectra as a function of time

For both homopolymers the kinetic constants were obtained by fitting the differential equations to percent concentration versus time curves such as in Figure 5, for all the intermediate species formed in the reactions outlined below for TEOS.

Reactions for TEOS

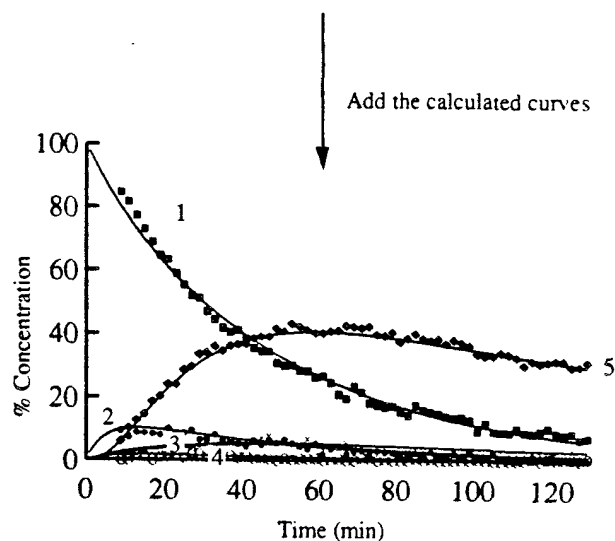
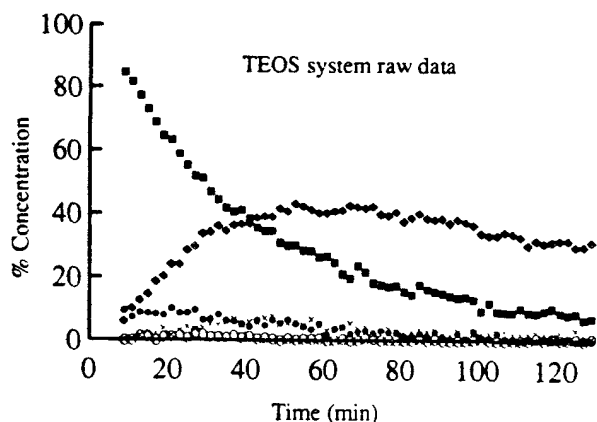
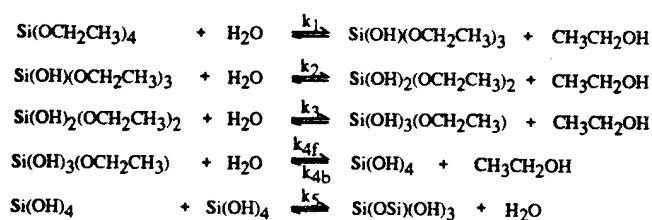


Figure 5 - Overview of the fitting of the hydrolysis reactions of the tetraethoxysilane at a pH = 2.55

- 1 - TEOS
- 2 - $\text{Si(OH)(OCH}_2\text{CH}_3)_3$
- 3 - $\text{Si(OH)}_2\text{(OCH}_2\text{CH}_3)_2$
- 4 - $\text{Si(OH)}_3\text{(OCH}_2\text{CH}_3)$
- 5 - Si(OH)_4

A parallel set of reactions were used to fit the MTES system.

In order to obtain pH independent constants, kinetic constants were obtained for eight different pHs. The final fitting process included the change in water and ethanol concentration, one equilibrium reaction in order to fit the data for $\text{Si(OH)}_3\text{(OSi)}$ and $\text{CH}_3\text{Si(OH)}_2\text{(OSi)}$ in the TEOS and MTES system, respectively, and the dimer formation to fit the depletion of the fully hydrolyzed monomer in both systems. Acceptable fits were obtained for the kinetic data as illustrated for TEOS in Figure 5. These kinetic constants were plotted against concentration of acid to obtain the pH independent kinetic constants for TEOS and MTES as listed in Table 1.

Further, in the copolymer system of TEOS and MTES, the formation of both the homodimers and also the co-dimer is clearly observed, Figure 6. Changing the time of mixing of the two monomers, their relative concentrations or doubling the water concentration has little effect on the formation of either the homo- or co-dimers suggesting that in this system there is a strong tendency for the formation of a random copolymer.

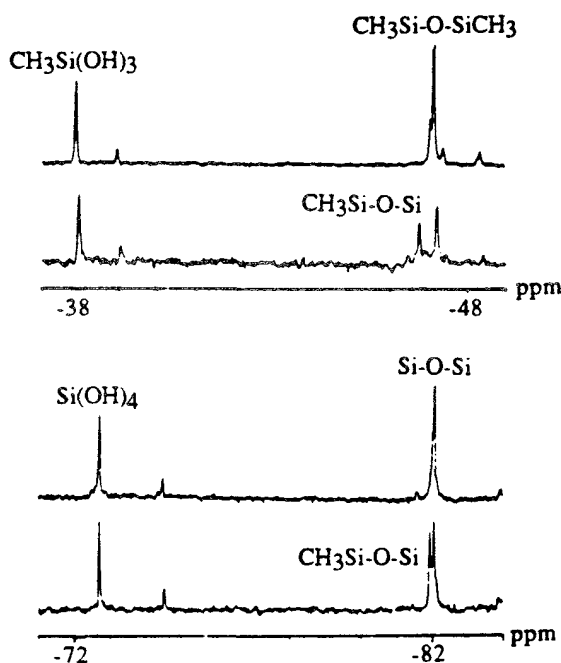


Figure 6 Copolymer compared to homopolymers
 A - MTES homopolymer
 B - Copolymer MTES region
 C - TEOS homopolymer
 D - Copolymer TEOS region

Table 1 - pH independent kinetic constants

Kinetic Constants	TEOS system (min ⁻¹)	MTES system (min ⁻¹)
k ₁	0.87 ± 0.03	8.1 ± 0.6
k ₂	4.8 ± 0.2	28 ± 3
k ₃	19 ± 1	-
k _{3f}	-	30 ± 3
k _{3b}	-	2.5 ± 0.2
k ₄	-	5.5 ± 0.3
k _{4f}	16 ± 3	-
k _{4b}	2.8 ± 0.5	-
k ₅	13.3 ± 0.5	-

4. CONCLUSIONS

2D ²⁹Si CP/MAS NMR measurements on the functionalized silica gel made by copolymerization of TEOS and MTES indicate that the two components are mixed rather than phase separated. High-resolution ²⁹Si solution NMR investigations of the sol-gel process yield the kinetic constants for hydrolysis and condensation and indicate a tendency towards alternation. These results suggest that this alternative method may be superior to the conventional approaches for the preparation of organofunctionalized gels.

5. REFERENCES

1. C.J. Brinker, D.E. Clark, D.R. Ulrich Better Ceramics Through Chemistry. Materials Research Society. In Materials Research Society Symposia Proceeding. (1984)
2. P.Caravatti, G. Bodenhausen, and R.R. Ernst, Chem.Phys.Lett. 89, 363, (1982)

Comparison of short-range interactions in zero electric field gradient mixtures

T. Chandrakumar, and E. Elliott Burnell
Department of Chemistry, University of British Columbia
2036 Main Mall, Vancouver, B.C., Canada V6T 1Z1

The solute ortho dichlorobenzene is studied in the zero electric field gradient mixtures 55 wt% 1132/EBBA and 70 wt% 5CB/EBBA using proton NMR. The short range interactions which are responsible for orientation in these special liquid crystal mixtures are compared. The short range potential is described by a one-parameter model. The order parameters calculated from the model are in very good agreement with the experimental order parameters.

I. INTRODUCTION

The nature of intermolecular interactions leading to orientational ordering in liquid crystals is not well understood. Some insight into these interactions can be obtained from studies of differences among liquid crystals. Usually, the intermolecular interactions are expressed as a mean field potential — each molecule experiences a potential via its interaction with other surrounding molecules.

The use of small solutes in liquid crystal solvents has been useful in understanding the differences among liquid crystals. In particular, studies involving the D_2 molecule dissolved in the liquid crystals 1132, 5CB and EBBA showed that the orientation of the D_2 molecule in these liquid crystals depends on the liquid crystal environment [1–5]. Further, it has been shown that there is an average electric field gradient present in the liquid crystals 1132, 5CB and EBBA, and that analysis of the NMR spectrum of D_2 gives an estimate of the magnitude of this electric field gradient [2–4]. This average electric field gradient, which differs from one liquid crystal environment to another, has a positive sign in the liquid crystals 1132 and 5CB and has a negative sign in EBBA. The interaction between this average electric field gradient and the electric quadrupole moment of a solute contributes to the anisotropic intermolecular potential [6,7]. In the case of D_2 this interaction is the dominant orientational mechanism [2–5].

A mixture of the liquid crystals 1132 and EBBA, or of 5CB and EBBA, can yield a liquid crystal combination in which the average electric field gradient as seen by the 2H nucleus in D_2 vanishes. The measured electric field gradient is zero for a mixture of 55 wt% 1132/EBBA at 301.4 K [6,7] and for a mixture of 70 wt% 5CB/EBBA at 316K [8]. We shall refer to these special mixtures, in which the measured average electric field gradient is zero, as zero efg mixtures. If the electric quadrupole moment - electric field gradient interaction is the only contribution to the intermolecular potential, then it is expected that the orientation of any small solute in the zero efg mixtures is zero. However, studies involving small solutes in the mixtures 55% 1132/EBBA [6,9–11] and 70% 5CB/EBBA [8] showed that the orientations of the solutes in these mixtures are non-zero. Therefore, there

must be an additional mechanism contributing to the intermolecular potential. Our group has proposed that this additional mechanism involves short-range interactions that depend on the size and shape of the solute [6,7,9].

To investigate the short-range interactions, it is useful to study a small solute in the zero efg mixtures where the contribution of the electric quadrupole moment - electric field gradient interaction to the intermolecular potential can be neglected. In this paper, the molecule ortho dichlorobenzene (ODCB) has been studied at a range of temperatures in the zero efg mixtures 55% 1132/EBBA and 70% 5CB/EBBA. We shall use a model based on the size and shape of the solute for the short-range potential and shall neglect the small contribution to the orientational ordering from the electric field gradient - electric quadrupole moment interaction at temperatures different from those when it is zero.

II. EXPERIMENTAL

The liquid crystal ZLI-1132, which is an eutectic mixture of alkylcyclohexylcyanobenzene and alkylcyclohexylcyanobiphenyls, and the liquid crystal 5CB were purchased from Merck and not purified prior to use. The liquid crystal EBBA was synthesized in Amsterdam [12]. The 1132, EBBA and 5CB were used to prepare the mixtures 55 wt% 1132/EBBA and 70 wt% 5CB/EBBA. The liquid crystal mixtures were placed into 5 mm NMR sample tubes, and 1-2 mol% of ODCB was dissolved in each mixture.

Proton NMR experiments were performed on a Bruker WH-400 high-resolution NMR spectrometer operating at 9.4 T (400.1 MHz for proton) and equipped with a temperature control unit. 1H - free induction decays were collected, and the spectra were obtained by Fourier transforming the free induction decays. The experiment was repeated as a function of temperature for both liquid crystal mixtures.

III. RESULTS

The experimental spectrum of ODCB in the 70% 5CB/EBBA mixture at 300K is shown in Fig. 1. The

line positions were measured using the Bruker Peak Picking routine. The spectral line widths are typically in the range 3-5 Hz for room temperature spectra, and are broadened at temperatures far from room temperature. For broad peaks, the line positions were measured at the centre of the area of the peak.

The measured line positions were fitted using the programme LEQUOR [13] to obtain the dipolar couplings, D_{ij} , and the two chemical shifts ν_1 and ν_2 . These values are reported in Tables 1 and 2 for all temperatures studied. Scalar couplings, J_{ij} , are assumed to be equal to the isotropic values taken from reference [14].

IV. DISCUSSION

The dipolar couplings D_{ij} of ODCB in the zero efg mixtures can be related to the geometry and orientation of the ODCB by the equation

$$D_{ij} = \frac{-\gamma_i \gamma_j \hbar}{8\pi^2 r_{ij}^3} [S_{zz}(3 \cos^2 \theta_{ijz} - 1) + (S_{xx} - S_{yy})(\cos^2 \theta_{ijx} - \cos^2 \theta_{ijy})] \quad (1)$$

where the molecule-fixed axes x , y and z are defined in Fig. 1. S_{zz} and $S_{xx}-S_{yy}$ are the order parameters of the ODCB in the liquid crystal mixtures. The programme SHAPE [15] was used to obtain these order parameters from the dipolar couplings and from an assumed geometry of ODCB from reference [14]. The order parameters S_{zz} and $S_{xx}-S_{yy}$ are plotted against temperature in Fig. 2 (filled points). We also plot the order parameters S_{zz} and $S_{xx}-S_{yy}$ against reduced temperature, T_r , in Fig. 3, where T_r is defined as $T_r = T/T_{NI}$ and T_{NI} is the nematic - isotropic transition temperature. The T_{NI} values of the mixtures 55% 1132/EBBA and 70% 5CB/EBBA are found to be 333K and 317K.

The order parameters $S_{\alpha\beta}$ can be related to the intermolecular potential, $U(\Omega)$, by

$$S_{\alpha\beta} = \frac{\int (3 \cos \theta_\alpha \cos \theta_\beta - \delta_{\alpha\beta}) \exp(-U(\Omega)/kT) d\Omega}{2 \int \exp(-U(\Omega)/kT) d\Omega} \quad (2)$$

where $\cos \theta_\alpha$, $\cos \theta_\beta$ are the direction cosines of the α , β axes with respect to the director, Z , axis. The intermolecular potential can be written as a summation of the electric field gradient - electric quadrupole moment interaction potential and a short-range potential, $U_{sr}(\Omega)$ [6]. Due to the absence of the electric field gradient in the zero efg mixtures, the intermolecular potential $U(\Omega)$ is assumed to be equal to the short-range potential, $U_{sr}(\Omega)$.

The main aim of this study is to see if the short-range potentials in the two different zero efg mixtures 55% 1132/EBBA and 70% 5CB/EBBA are the same. The precise nature of the short-range potential is not known well. In this study we shall choose a one-parameter model that was very successful in modelling the order parameters of 46 small solutes in 55% 1132/EBBA at 301.4K [16]. The chosen model is

$$U_{sr}(\Omega) = -\frac{1}{2} k_s \int_{Z_{min}}^{Z_{max}} C_Z(\Omega) dZ \quad (3)$$

where k_s is a model parameter, Z is the projection of the solute along the Z (director) direction and $C_Z(\Omega)$ is the circumference of the solute at distance Z . To calculate the $C_Z(\Omega)$, the solute molecule is taken as a collection of van der Waals spheres, and van der Waals radii are taken from Bondi *et al.* [17].

A least-squares fit was done on the experimental order parameters for each temperature to obtain the best fit model parameter k_s . This best fit model parameter was then used to estimate the recalculated order parameters S_{zz} and $S_{xx}-S_{yy}$ of ODCB, and these recalculated order parameters are plotted in Fig. 2 (open triangles and squares). The agreement between the experimental and recalculated order parameters S_{zz} is very good. Although the recalculated $S_{xx}-S_{yy}$ values are close to the experimental values, the agreement is not as good as for S_{zz} . The quantity $S_{xx}-S_{yy}$ is the difference between two order parameters and is often more difficult to fit than S_{zz} [16].

The fitted model parameters k_s are plotted against temperature in Fig. 4. It is instructive to compare the k_s value obtained in this fit for 55% 1132/EBBA at 301K, 67.54 dyn/cm, to the value 76.7 dyn/cm obtained from a study of 46 solutes in 55% 1132/EBBA at 301K [16].

We note that in Fig. 3(a) the S_{zz} values of 55% 1132/EBBA and 70% 5CB/EBBA are very close for a given reduced temperature. In order to understand this plot in terms of the model parameters k_s , we consider eq. 2 and eq. 3 and find that the order parameter $S_{\alpha\beta}$ depends on k_s/T . Thus, $S_{\alpha\beta}$ can be written as:

$$S_{\alpha\beta} = f(k_s/T) \quad (4)$$

To examine the dependence of the quantity k_s/T on liquid crystal environment, we plot k_s/T vs. T_r for both liquid crystal mixtures in Fig. 5. The plot shows that there is very good agreement between the k_s/T values for 55% 1132/EBBA and 70% 5CB/EBBA. Based on this agreement, we write the following relationship

$$(k_s/T)_{T_r,55} = (k_s/T)_{T_r,70} \quad (5)$$

for a given T_r , where the subscripts 55 and 70 stand for the liquid crystal mixtures 55% 1132/EBBA and 70% 5CB/EBBA. Substituting eq. 5 into eq. 3, we get the relationship

$$(U_{sr}/T)_{T_r,55} = (U_{sr}/T)_{T_r,70} \quad (6)$$

In order to simplify the notation, we introduce the reduced short-range potential, U_{sr}^r , and reduced model parameter, k_s^r , defined by $U_{sr}^r = U_{sr}/T$ and $k_s^r = k_s/T$.

Equations 5 and 6 suggest that at a given T_r the reduced short-range potential, U_{sr}^r , and the reduced model parameter, k_s^r , are transferable from one of these two

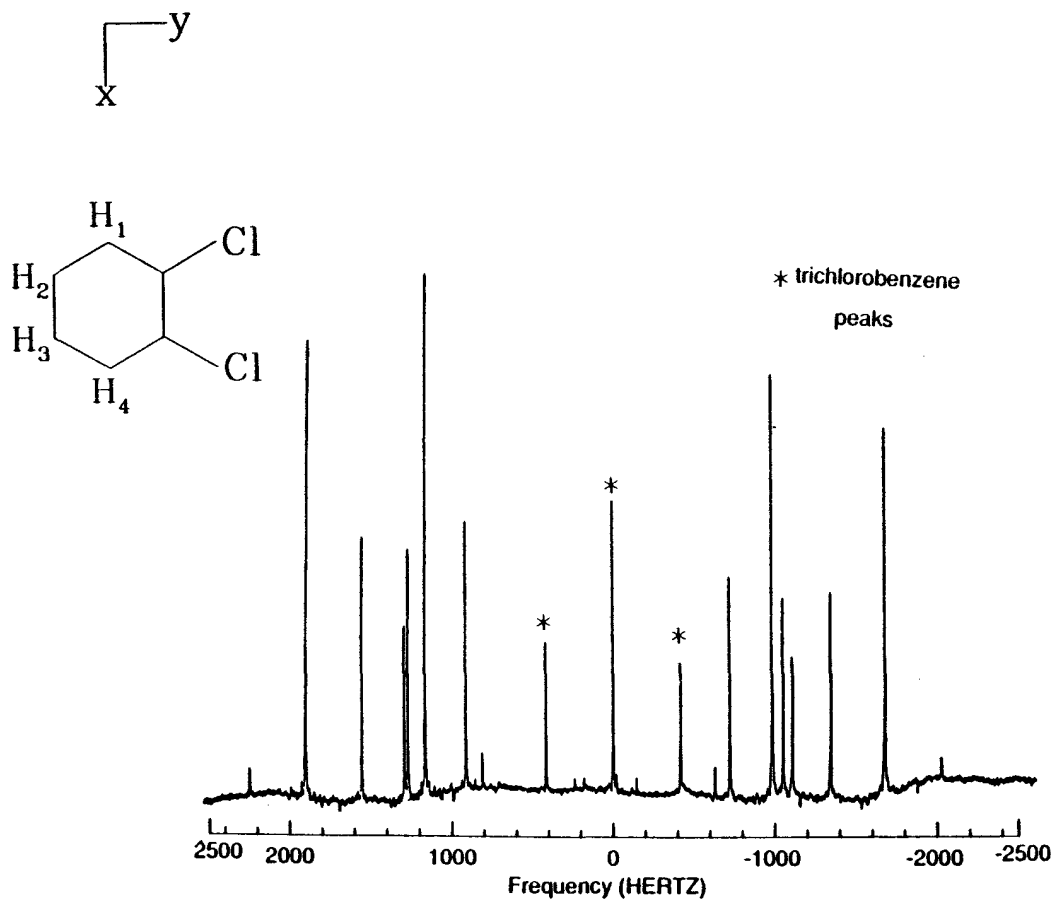


FIG. 1. Experimental ^1H -NMR spectrum of ortho dichloro benzene dissolved in the zero efg mixture 70% 5CB/EBBA at 300K along with the coordinate system and atom numbering scheme used in this paper.

Temp / K	$D_{12} = D_{34}$	$D_{13} = D_{24}$	D_{14}	D_{23}
301	-1036.32 ± 0.04	-132.30 ± 0.01	-64.49 ± 0.02	-494.85 ± 0.05
305	-996.55 ± 0.05	-128.31 ± 0.02	-63.11 ± 0.02	-484.58 ± 0.06
310	-945.08 ± 0.03	-122.93 ± 0.08	-61.05 ± 0.09	-469.47 ± 0.04
315	-886.20 ± 0.10	-116.50 ± 0.29	-58.46 ± 0.22	-450.11 ± 0.13
320	-817.69 ± 0.16	-108.92 ± 0.39	-55.20 ± 0.44	-424.28 ± 0.19
322	-799.08 ± 1.11	-106.65 ± 0.33	-54.79 ± 0.46	-417.20 ± 1.28
325	-747.60 ± 0.46	-99.74 ± 1.01	-51.64 ± 1.48	-394.86 ± 0.66
327	-710.45 ± 0.70	-95.73 ± 0.21	-49.01 ± 0.29	-379.39 ± 0.80
330	-643.93 ± 1.02	-87.12 ± 0.32	-43.87 ± 0.43	-349.43 ± 1.17
	$J_{12} = J_{34} = 8.00$	$J_{13} = J_{24} = 1.50$	$J_{14} = 0.30$	$J_{23} = 7.40$

TABLE I. Dipolar couplings in Hz of 55% 1132/EBBA obtained from LEQUOR. J_{ij} values are taken from reference [14].

Temp / K	$D_{12} = D_{34}$	$D_{13} = D_{24}$	D_{14}	D_{23}
288	-1022.54 ± 0.33	-122.96 ± 1.31	-56.86 ± 0.97	-431.07 ± 0.46
292	-987.28 ± 0.15	-119.75 ± 0.38	-55.50 ± 0.54	-422.13 ± 0.19
298	-955.73 ± 0.30	-117.17 ± 1.09	-53.13 ± 0.79	-415.82 ± 0.40
300	-895.85 ± 0.04	-110.40 ± 0.10	-51.86 ± 0.03	-396.96 ± 0.09
302	-895.03 ± 0.02	-110.30 ± 0.09	-51.77 ± 0.02	-396.67 ± 0.07
304	-879.09 ± 0.04	-108.66 ± 0.10	-51.13 ± 0.03	-392.03 ± 0.08
305	-865.92 ± 0.09	-107.26 ± 0.02	-50.69 ± 0.03	-387.92 ± 0.11
307	-848.48 ± 0.12	-105.47 ± 0.03	-49.97 ± 0.05	-382.62 ± 0.14
309	-829.01 ± 0.10	-103.30 ± 0.24	-48.95 ± 0.30	-376.31 ± 0.12
311	-766.75 ± 0.28	-96.28 ± 0.68	-46.57 ± 0.87	-354.58 ± 0.35
313	-715.33 ± 0.36	-90.26 ± 1.03	-43.47 ± 0.94	-335.75 ± 0.42
315	-661.30 ± 0.18	-84.37 ± 0.44	-40.69 ± 0.56	-314.04 ± 0.23
316	-606.30 ± 0.64	-77.70 ± 1.77	-37.00 ± 1.40	-293.59 ± 0.75
	$J_{12} = J_{34} = 8.00$	$J_{13} = J_{24} = 1.50$	$J_{14} = 0.30$	$J_{23} = 7.40$

TABLE II. Dipolar couplings in Hz of 70% 5CB/EBBA obtained from LEQUOR. J_i values are taken from reference [14].

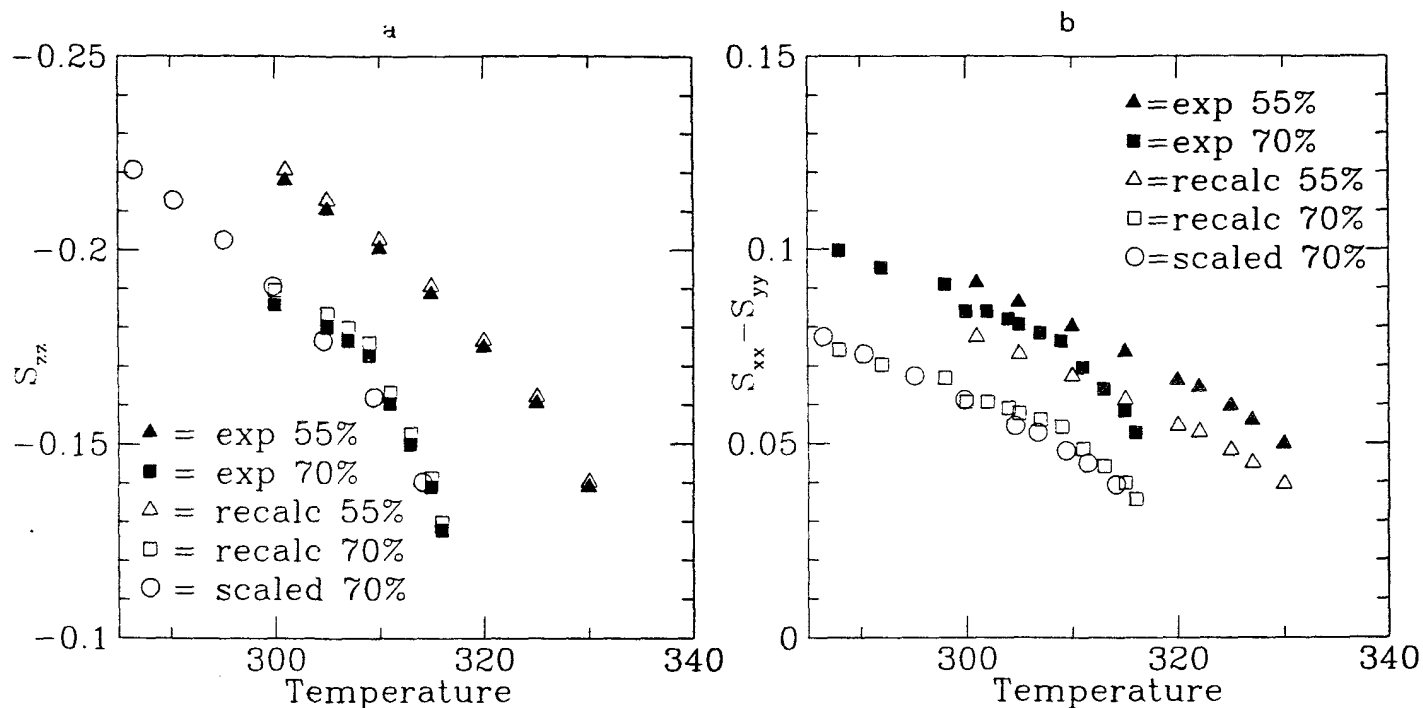


FIG. 2. (a) The order parameter S_{zz} versus temperature for the mixtures 55% 1132/EBBA and 70% 5CB/EBBA. Closed triangles (\blacktriangle) and open triangles (\triangle) represent the experimental and recalculated order parameters S_{zz} of 55% 1132/EBBA. Closed squares (\blacksquare) and open squares (\square) represent the experimental and recalculated order parameters S_{zz} of 70% 5CB/EBBA. The open circles (\circ) represent the scaled order parameters S_{zz} of 70% 5CB/EBBA. (b) The order parameter $S_{xx} - S_{yy}$ versus temperature for the mixtures 55% 1132/EBBA and 70% 5CB/EBBA. The symbols have the same meaning as in (a).

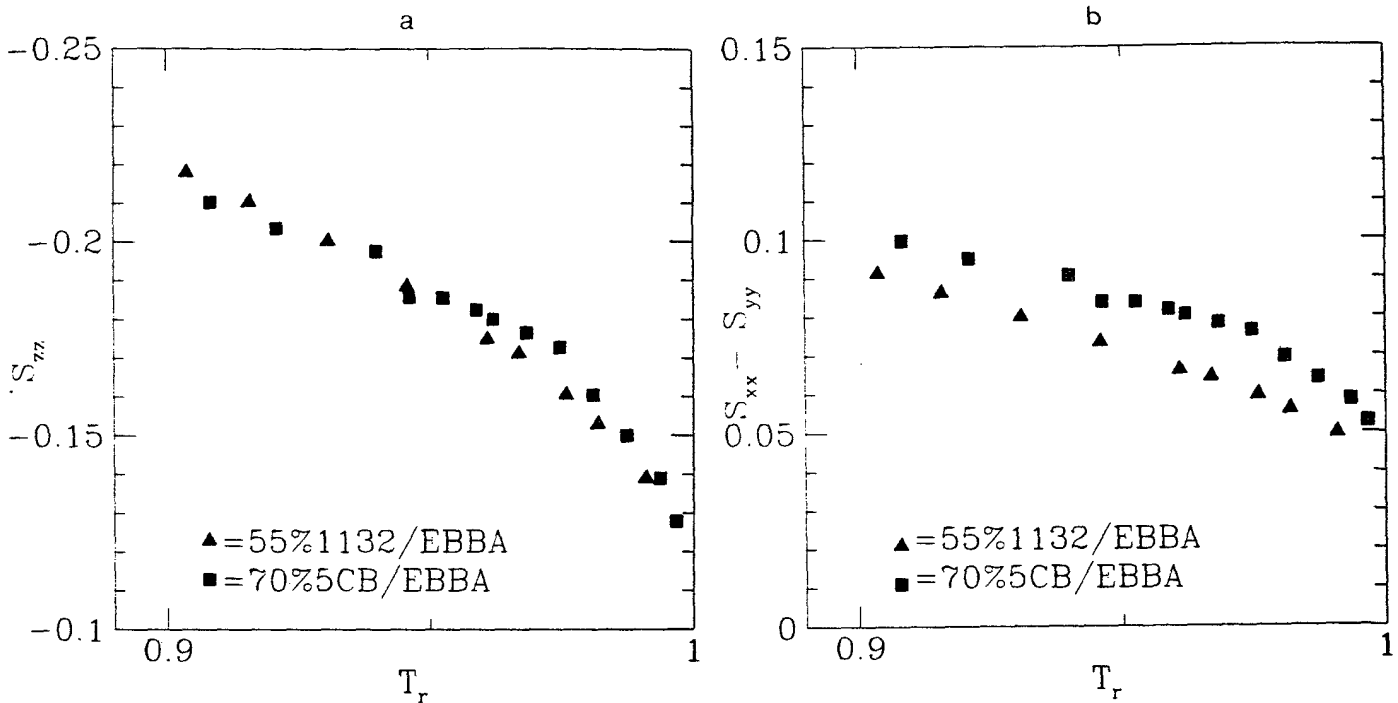


FIG. 3. (a) The order parameter S_{zz} versus reduced temperature. Closed triangles (\blacktriangle) and closed squares (\blacksquare) represent the order parameters S_{zz} of the mixtures 55% 1132/EBBA and 70% 5CB/EBBA. (b) The order parameter $S_{xx} - S_{yy}$ versus reduced temperature. The symbols have the same meaning as in (a).

mixtures to the other. This suggests that the order parameters of one zero efg mixture can be predicted knowing the reduced model parameters of the other. We shall call these predicted order parameters "Scaled order parameters", and the calculation of the Scaled order parameters is described as follows.

For a given reduced temperature, the temperature of the mixture 55% 1132/EBBA, T_{55} , differs from that of 70% 5CB/EBBA, T_{70} . The ratio of the temperatures T_{55}/T_{70} at all reduced temperatures is equal to the nematic-isotropic transition temperature ratio, $(T_{NI})_{55}/(T_{NI})_{70}$, which is equal to 1.050. This value shall be referred to as Temperature Scaling Factor (TSF).

In this study, we shall start from the model parameters of 55% 1132/EBBA and predict the order parameters of 70% 5CB/EBBA. The parameters k_s and temperatures (T_{55}) of 55% 1132/EBBA are scaled down by the TSF, and these scaled values are used to calculate the scaled order parameters $S_{\alpha\beta}$ of 70% 5CB/EBBA using eq. 2 and eq. 3. The Scaled (circles) along with experimental (filled symbols) and recalculated (open symbols) order parameters S_{zz} and $S_{xx} - S_{yy}$ of ODCB are plotted against temperature in Fig. 2. The Scaled order parameters S_{zz} agree very well with the experimental and recalculated order parameters for 70% 5CB/EBBA. The agreement between the scaled and recalculated order parameters $S_{xx} - S_{yy}$ is also good. This confirms that the reduced model parameter k_s^r and the reduced short-range poten-

tial U_{sr}^r is transferable from the zero efg mixture 55% 1132/EBBA to the zero efg mixture 70% 5CB/EBBA. Thus, the reduced short range potentials U_{sr}^r are the same in both zero efg mixtures.

V. CONCLUSION

The model used for the short range potential is quite successful in calculating the order parameters of ODCB in the zero efg mixtures 55% 1132/EBBA and 70% 5CB/EBBA. The model parameters are useful in comparing the short-range interactions of the two mixtures, and it is found that the reduced model parameters, k_s^r , of the two mixtures are the same. Further, the Scaled order parameters of ODCB in the 70% 5CB/EBBA mixture are well predicted starting from the reduced model parameters of the 55% 1132/EBBA mixture. Thus, the short range potentials are the same in the zero efg mixtures 55% 1132/EBBA and 70% 5CB/EBBA.

We thank Dan Zimmerman, Leon ter Beek and James Polson for their valuable discussions. We also Acknowledge to the Natural Science and Engineering Research Council of Canada for support of this research. We thank Hans Barnhoorn of the University of Amsterdam for the gift of EBBA.

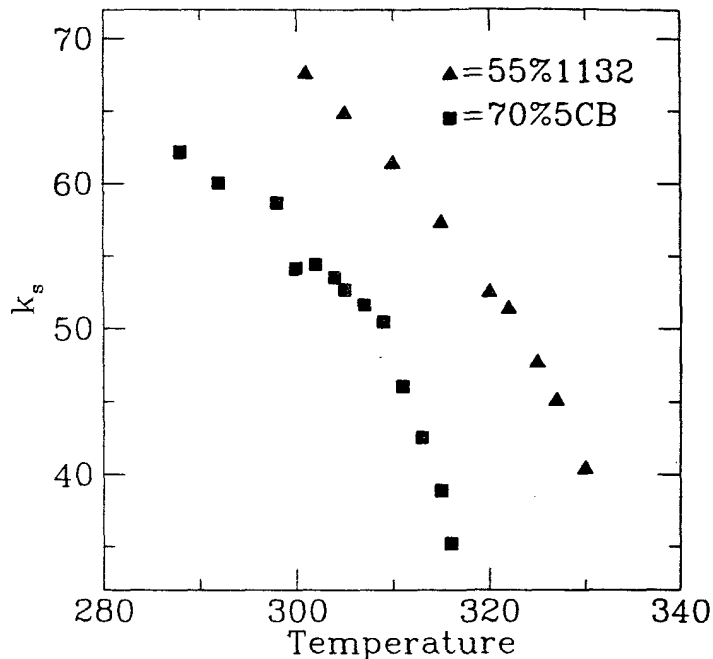


FIG. 4. The model parameter k_s versus temperature. Closed triangles (\blacktriangle) and closed squares (\blacksquare) represent the model parameters k_s of the mixtures 55% 1132/EBBA and 70% 5CB/EBBA.

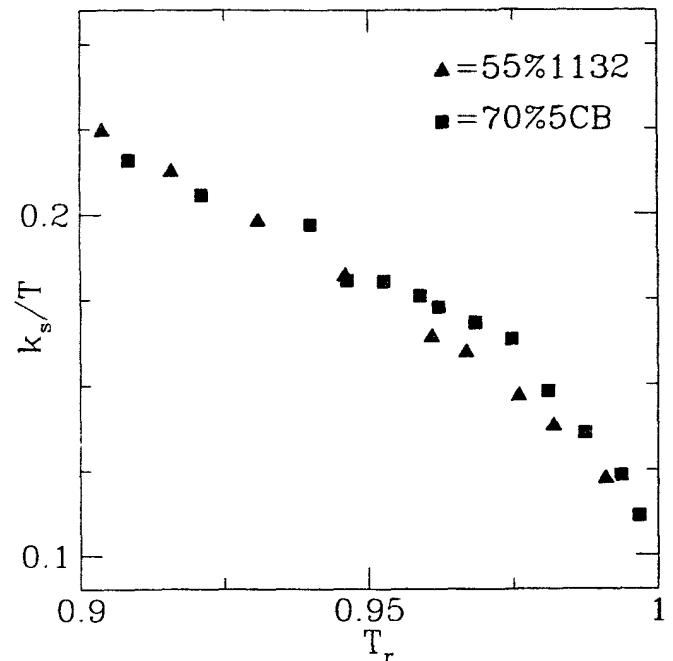


FIG. 5. The reduced model parameter k_s/T versus reduced temperature. Closed triangles (\blacktriangle) and closed squares (\blacksquare) represent the model parameters k_s/T of the mixtures 55% 1132/EBBA and 70% 5CB/EBBA.

- [1] Burnell, E.E., de Lange, C.A., and Snijders, J.G., 1982, *Phys. Rev. A*, **25**, 2339.
- [2] Barker, P.B., van der Est, A.J., Burnell, E.E., Patey, G.N., de Lange, C.A., and Snijders, J.G., 1984, *Chem. Phys. Lett.*, **107**, 426.
- [3] Patey, G.N., Burnell, E.E., Snijders, J.G., and de Lange, C.A., 1983, *Chem. Phys. Lett.*, **99**, 271.
- [4] Weaver, A., van der Est, A.J., Rendell, J.C.T., Hoatson, G.L., Bates, G.S., and Burnell, E.E., 1987, *Liq. Crystals*, **2**, 633.
- [5] van der Est, A.J., Burnell, E.E., and Lounila, J., 1988, *J. Chem. Soc., Faraday Trans. 2*, **84**, 1095.
- [6] van der Est, A.J., Kok, M.Y., Burnell, E.E., 1987, *Mol. Phys.*, **60**, 397.
- [7] van der Est, A.J., 1987, Ph. D. thesis, University of British Columbia.
- [8] Barnhoorn, J.B.S., de Lange, C.A., and Burnell, E.E., *Liq. Crystals*. (in press).
- [9] Zimmerman, D.S., and Burnell, E.E., 1990, *Mol. Phys.*, **69**, 1059.
- [10] Li, K.Y., Zimmerman, D.S., Burnell, E.E., *Mol. Phys.*, (in press).
- [11] Zimmerman, D.S., Li, K.Y., Burnell, E.E., 1991, *Mol. Cryst. Liq. Cryst.*, **203**, 61.
- [12] Keller, P., and Liebert, L., 1978, *Solid State Phys. Suppl.*, **14**, 19.
- [13] Diehl, P., Kellarhals, H., and Lusting, E., "NMR Basic Principles and Progress", 1972, **6**, 1.
- [14] Diehl, P., and Ketrapal, C.L., 1968, *Mol. Phys.*, **15**, 201.
- [15] Diehl, P., Henrichs, P.M., and Niederberger, W., 1971, *Mol. Phys.*, **20**, 139.
- [16] Zimmerman, D.S., and Burnell, E.E., *Mol. Phys.*, (in press).
- [17] Bondi, A., 1964, *J. Phys. Chem.*, **68**, 441.

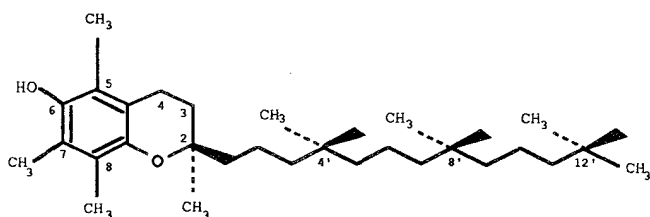
^2H NMR STUDIES OF MEMBRANE STABILIZATION**BY VITAMIN E**Stephen R. Wassall, Sudha Ayalasomayajula,
George L. Griffith and M. Alan McCabeDepartment of Physics
Indiana University-Purdue University at Indianapolis
402 N. Blackford Street
Indianapolis, IN 46202-3273, USA

and

William D. Ehringer and William Stillwell

Department of Biology
Indiana University-Purdue University at Indianapolis
723 W. Michigan Street
Indianapolis, IN 46202-5132, USA**INTRODUCTION**

The major constituent of vitamin E is α -tocopherol. It is a lipid soluble antioxidant that is generally believed to protect phospholipids from peroxidation. Structural roles have also been

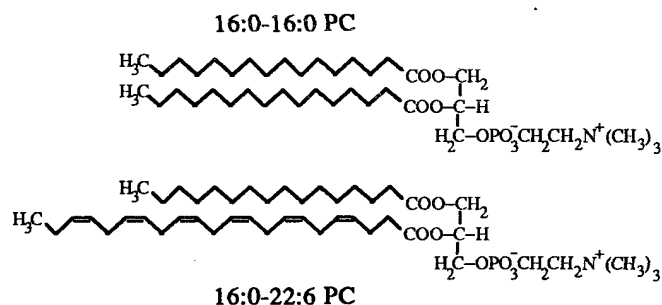


ALPHA-TOCOPHEROL

hypothesized [1,2]. The current studies focus on the proposal that the conformation of polyunsaturated phospholipid chains provides pockets into which the methyl groups on the phytyl side chain of α -tocopherol fit and stabilize the membrane [1]. The work demonstrates that the techniques of broadband ^2H NMR have the potential to definitively evaluate the hypothesis.

When α -tocopherol is incorporated into membranes the chromanol moiety resides near the surface while the phytyl side chain extends towards the interior and lies parallel, on average, to the phospholipid chains [3,4]. The gel to liquid crystalline phase transition is broadened, and the onset temperature is depressed [5]. Acyl chain mobility becomes less restricted in the gel phase, whereas in the liquid crystalline state order is greater and fluidity is reduced [5,6]. These observations refer to single component PC (phosphatidylcholine) membranes.

In the experiments described here, lineshape analyses of ^2H NMR spectra were implemented to investigate the influence α -tocopherol has on phase behaviour and molecular ordering for each component in a saturated/polyunsaturated mixed phospholipid membrane. The collection of essentially distortion free spectra with the quadrupolar echo sequence, $90^\circ_x - \tau_2 - 90^\circ_y$ -acquire-delay, made this possible [7]. Specifically, ^2H NMR spectra were recorded for $[^2\text{H}_{62}]16:0-16:0\text{PC}/16:0-22:6\text{PC}$ (1,2- $[^2\text{H}_{62}]$ dipalmitoylPC/1-palmitoyl-2-docosahexaenoylPC) (4:1 mol ratio) and $16:0-16:0\text{PC}/[^2\text{H}_{31}]16:0-22:6\text{PC}$ (1,2-dipalmitoylPC/1- $[^2\text{H}_{31}]$ palmitoyl-2-docosahexaenoylPC) (4:1 mol ratio) membranes containing 0 or 9 mol% α -tocopherol. The effects of α -tocopherol on the saturated and polyunsatu-



rated phospholipids could then be compared, which represents a direct test of the hypothesized membrane stabilization due to interactions with polyunsaturated fatty acyl chains. Such interactions would be presumably manifest in a discrimination between the phospholipids.

^2H NMR

Phase Behaviour

^2H NMR spectra for $[\text{}^2\text{H}_{62}]16:0-16:0$ PC/ $16:0-22:6$ PC membranes in the presence of 0 and 9 mol% α -tocopherol are shown in Figure 1. The spectra monitor the *sn*-1 and -2 chains of the saturated phospholipid. Motional equivalence of the chains, although not strictly true, is assumed [8]. Typical gel state spectra were obtained at 15°C . They are similar, but not identical, with and without α -tocopherol. The edges at ± 63 kHz

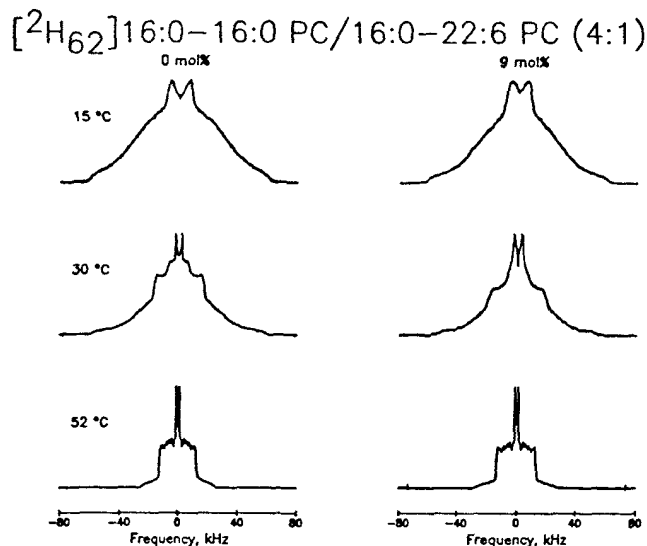


Figure 1. ^2H NMR spectra for $[\text{}^2\text{H}_{62}]16:0-16:0$ PC/ $16:0-22:6$ PC (4:1 mol ratio) membranes with 0 and 9 mol% α -tocopherol.

correspond to static methylenes, while spectral intensity towards the centre indicates the occurrence of some acyl chain motion. The spectra at 52°C are characteristic of the liquid crystalline phase. They possess sharp edges at approximately $\pm 13-14$ kHz corresponding to a plateau region of almost constant order in the upper portion of the chain. The peaks within the spectra are due to individual segments in the lower portion of the chain where order decreases towards the terminal methyl group. The spectrum is of slightly greater width and the peaks are less well resolved when α -tocopherol is present. At 30°C , the spectra suggest that the saturated $[\text{}^2\text{H}_{31}]16:0-16:0$ PC is in phase transition. Both gel and liquid crystalline spectral components are clearly apparent in the absence of α -tocopherol. The shape of the spectrum is noticeably dissimilar following the incorporation of α -tocopherol, but the intermediate spectral component of approximately 40 kHz width is indicative of rapid reorientation for the methylene chain as a whole at the onset of the transition.

The spectra plotted in Figure 2 for $16:0-16:0$ PC/ $[\text{}^2\text{H}_{31}]16:0-22:6$ PC membranes focus on the $[\text{}^2\text{H}_{31}]16:0$ *sn*-1 chain of the polyunsaturated phospholipid and so facilitate comparison with the saturated membrane constituent. Although they demonstrate that the phospholipids respond comparably to the introduction of α -tocopherol when the entire membrane is in the liquid crystalline phase as at 52° , the trend exhibited at lower temperature differs appreciably. The spectrum for $16:0-16:0$ PC/ $[\text{}^2\text{H}_{31}]16:0-22:6$ PC membranes at 30°C is almost completely

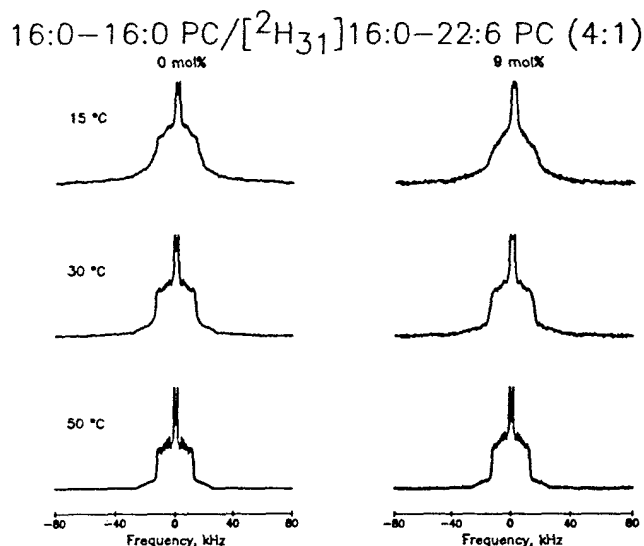


Figure 2. ^2H NMR spectra for $16:0-16:0$ PC/ $[\text{}^2\text{H}_{31}]16:0-22:6$ PC (4:1 mol ratio) membranes with 0 and 9 mol% α -tocopherol.

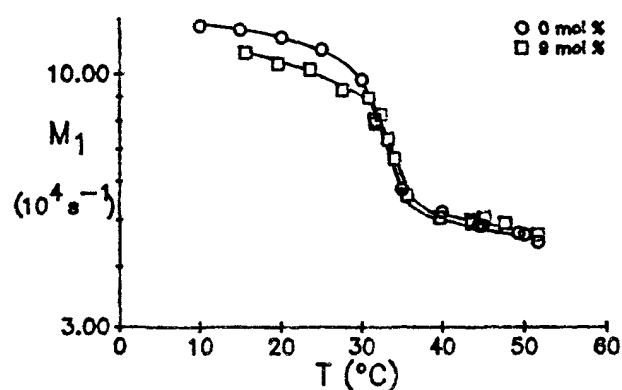
liquid crystalline despite the largely gel state nature of the saturated component at the same temperature. This implies phase separation of the saturated and polyunsaturated phospholipids. Monotectic behaviour for mixtures of phospholipids with markedly dissimilar chains has previously been concluded on the basis of calorimetric measurements [9]. Spectral broadening and an almost total loss of peak resolution are observed at 30°C for $16:0-16:0$ PC/ $[\text{}^2\text{H}_{31}]16:0-22:6$ PC upon addition of α -tocopherol. These changes resemble those seen at higher temperature in the completely liquid crystalline membrane, except that the effect on the polyunsaturated phospholipid at the lower temperature is greater. At 15°C , relatively narrow spectra are recorded for $16:0-16:0$ PC/ $[\text{}^2\text{H}_{31}]16:0-22:6$ PC membranes containing 0 or 9 mol% α -tocopherol. They establish that the *sn*-1 chain of the polyunsaturated phospholipid still possesses considerable mobility and has not adopted gel state structure. Detailed interpretation is precluded here by their ill-defined spectral shape.

Spectral moments M_n are defined by

$$M_n = \frac{\int_{-\infty}^{\infty} |\omega|^n f(\omega) d\omega}{\int_{-\infty}^{\infty} f(\omega) d\omega} \quad (1)$$

where ω is the frequency with respect to the central Larmor frequency, $f(\omega)$ is the lineshape and n is the order of the moment [7]. They are very sensitive to membrane phase, exhibiting a discontinuity in value on going from gel to liquid crystal. The graphs of first moment M_1 v. temperature T presented in Figure 3 for $[^2\text{H}_{62}]16:0-16:0\text{PC}/16:0-22:6\text{PC}$ and $16:0-16:0\text{PC}/[^2\text{H}_{31}]16:0-22:6\text{PC}$ membranes clearly demonstrate that the saturated and polyunsaturated phospholipids have different phase behaviour within the mixed membrane. Further support is therefore derived for phase separation. The discontinuity in

$[^2\text{H}_{62}]16:0-16:0\text{PC}/16:0-22:6\text{PC}$ (4:1)



$16:0-16:0\text{PC}/[^2\text{H}_{31}]16:0-22:6\text{PC}$ (4:1)

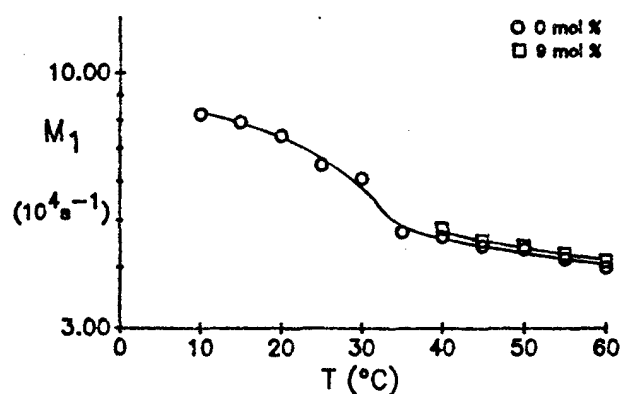


Figure 3. First moment M_1 v. temperature T for $[^2\text{H}_{62}]16:0-16:0\text{PC}/16:0-22:6\text{PC}$ (4:1 mol ratio) and $16:0-16:0\text{PC}/[^2\text{H}_{31}]16:0-22:6\text{PC}$ (4:1 mol ratio) membranes with 0 and 9 mol% α -tocopherol.

M_1 observed for $[^2\text{H}_{62}]16:0-16:0\text{PC}/16:0-22:6\text{PC}$ shows that the transition from gel to liquid crystalline state for the saturated phospholipid is about 6°C wide and has a mid point temperature of approximately $T_m = 32^\circ\text{C}$. In contrast, the temperature dependence observed for $16:0-16:0\text{PC}/[^2\text{H}_{31}]16:0-22:6\text{PC}$ does not show a dramatic discontinuity in M_1 for the polyunsaturated phospholipid. The first moments, which never attain values corresponding to gel phase in the restricted temperature range studied, gradually decrease between 10°C and 30°C before becoming characteristic of liquid crystalline phase at higher temperatures. As expected, the plots in Figure 3 differ from those previously published for single component membranes from which phase transition temperatures were measured at 37°C for $[^2\text{H}_{62}]16:0-16:0\text{PC}$ and at $-12^\circ\text{C}/-3^\circ\text{C}$ (temperature decreasing/increasing) for $[^2\text{H}_{31}]16:0-22:6\text{PC}$ [10,11].

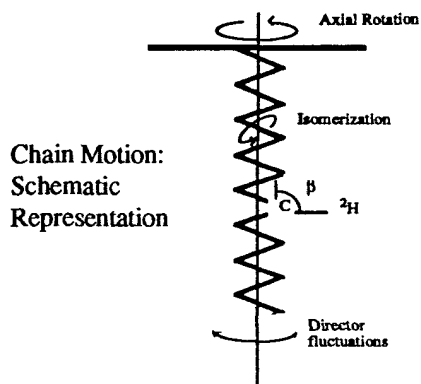
The first moments shown in Figure 3 for $[^2\text{H}_{62}]16:0-16:0\text{PC}/16:0-22:6\text{PC}$ membranes containing 9 mol% α -tocopherol imply that the introduction of this concentration of the vitamin causes little change in the gel to liquid crystalline phase transition for the saturated phospholipid. Specifically, the transition is of similar width and its mid point temperature is raised by about 2°C . This is considerably different from the behaviour seen in single component PC- d_{31} (*sn*-2- $[^2\text{H}_{31}]16:0$ substituted egg PC) bilayers, where the incorporation of 10 mol% α -tocopherol broadens the phase transition from $\leq 2^\circ\text{C}$ to approximately 8°C in width and lowers the mid point temperature from $T_m = 40^\circ\text{C}$ to 36°C [5]. Our interpretation is that the vitamin partitions into fluid regions of the mixed membrane which consist predominantly of polyunsaturated phospholipid when the saturated phospholipid passes into the gel phase, thereby modifying the phase transition of the latter phospholipid to only a small extent. The marked effect α -tocopherol has on the ^2H NMR spectrum for $16:0-16:0\text{PC}/[^2\text{H}_{31}]16:0-22:6\text{PC}$ membranes at 30°C (Figure 2), a temperature at which the saturated phospholipid is mainly gel while the polyunsaturated phospholipid is largely liquid crystalline, is consistent with this explanation. A preference of α -tocopherol for fluid regions of mixed membranes when gel and liquid crystalline phases coexist was earlier proposed in calorimetric work on $14:0-14:0\text{PC}/18:0-18:0\text{PC}$ (1,2-dimyristoylPC/1,2-distearoylPC) membranes [12].

Molecular Ordering

The motion of phospholipid acyl chains in the liquid crystalline state is axially symmetric about the normal to the membrane surface. The degree of anisotropy for the motion of an individual segment is quantified by ^2H NMR in terms of the order parameter

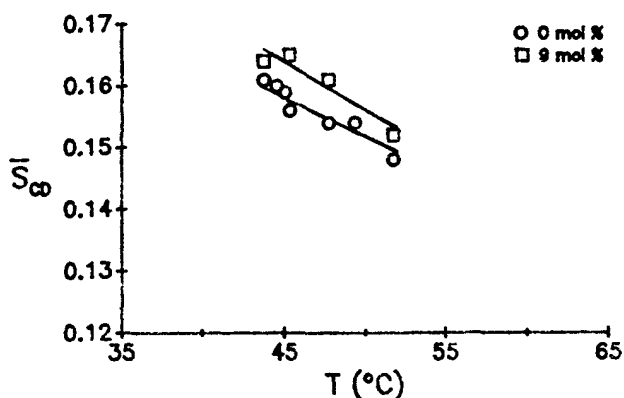
$$S_{\text{CD}} = \frac{1}{2} \langle 3 \cos^2 \beta - 1 \rangle \quad (2)$$

where β is the time dependent angle between the C- ^2H bond and the membrane normal, and the angular brackets designate a time average over the ^2H NMR timescale ($< 10^{-6}$ s) [13]. The



order parameter takes values in the range $0 \leq |S_{CD}| \leq \frac{1}{2}$, the respective limits representing effective isotropic motion (i.e. all angles sampled) and fast axial rotation (i.e. all *trans* chain, $\beta =$

$[^2\text{H}_{62}]16:0-16:0 \text{ PC}/16:0-22:6 \text{ PC (4:1)}$



$16:0-16:0 \text{ PC}/[^2\text{H}_{31}]16:0-22:6 \text{ PC (4:1)}$

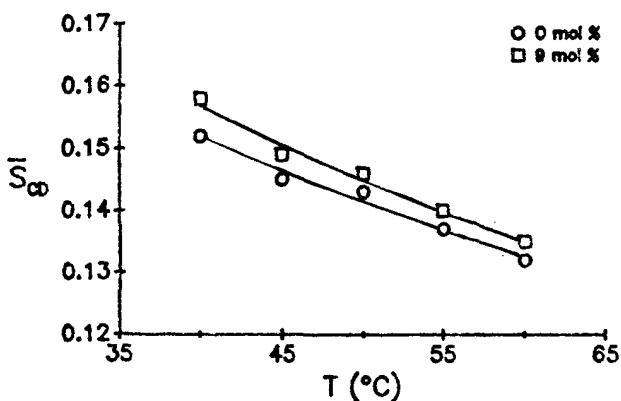


Figure 4. Average order parameters \bar{S}_{CD} v. temperature T for $[^2\text{H}_{62}]16:0-16:0\text{PC}/16:0-22:6\text{PC}$ (4:1 mol ratio) and $16:0-16:0\text{PC}/[^2\text{H}_{31}]16:0-22:6\text{PC}$ (4.1 mol ratio) membranes with 0 and 9 mol% α -tocopherol.

90°). It is directly related to the quadrupole splitting for a specifically deuterated segment, while for a perdeuterated chain an average order parameter \bar{S}_{CD} is calculated from the first moment M_1 with

$$M_1 = \frac{\pi}{\sqrt{3}} \left(\frac{e^2 q Q}{h} \right) \bar{S}_{CD} \quad (3)$$

where $(e^2 q Q/h) = 167 \text{ kHz}$ is the static quadrupolar coupling constant [7].

Average order parameters \bar{S}_{CD} determined as a function of temperature are presented in Figure 4 for $[^2\text{H}_{62}]16:0-16:0\text{PC}/16:0-22:6\text{PC}$ and $16:0-16:0\text{PC}/[^2\text{H}_{31}]16:0-22:6\text{PC}$ membranes with or without α -tocopherol. They reveal that the intercalation of α -tocopherol increases average order by approx. 3% for the saturated phospholipid v. approx. 2% for the polyunsaturated phospholipid. These changes are small compared to the increase of 9% measured in single component PC- d_{31} membranes when 10 mol% α -tocopherol was added [5]. The trend agrees with previous ESR and ^2H NMR experiments which revealed that α -tocopherol orders membranes to a lesser extent in the presence of acyl chain unsaturation [6,14,15]. The similarity in response registered by both components in the mixed membrane suggests that α -tocopherol does not interact preferentially with polyunsaturated phospholipids and argues against membrane stabilization by such a mechanism.

The depaking procedure numerically deconvolutes a powder pattern to extract an aligned spectrum [16]. The results of its application to spectra from $[^2\text{H}_{62}]16:0-16:0\text{PC}/16:0-22:6\text{PC}$ membranes at 52°C and $16:0-16:0\text{PC}/[^2\text{H}_{31}]16:0-22:6\text{PC}$

$[^2\text{H}_{62}]16:0-16:0 \text{ PC}/16:0-22:6 \text{ PC (4:1)}$



$16:0-16:0 \text{ PC}/[^2\text{H}_{31}]16:0-22:6 \text{ PC (4:1)}$

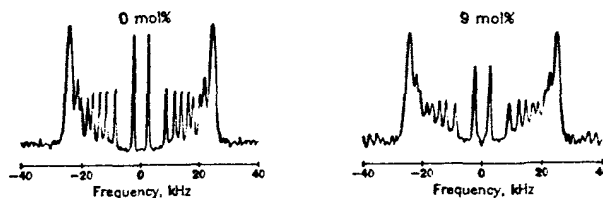


Figure 5. Depaked spectra for $[^2\text{H}_{62}]16:0-16:0\text{PC}/16:0-22:6\text{PC}$ (4:1 mol ratio) membranes at 52°C and $16:0-16:0\text{PC}/[^2\text{H}_{31}]16:0-22:6\text{PC}$ (4:1 mol ratio) membranes at 50°C with 0 and 9 mol% α -tocopherol.

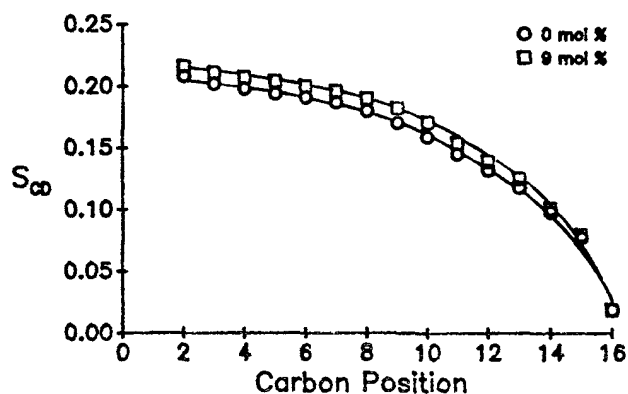
membranes at 50°C are shown in Figure 5 before and after the incorporation of 9 mol% α -tocopherol. They are equivalent to the spectra that would be obtained for a planar membrane oriented so that the normal to the surface coincides with the magnetic field direction. The enhanced resolution makes doublets visible, the splittings $\Delta\nu(\theta)$ of which correspond to order parameters via

$$\Delta\nu(\theta) = \frac{3}{2} \left(\frac{e^2 q Q}{h} \right) |S_{CD}| P_2(\cos \theta) \quad (4)$$

where $\theta = 0^\circ$ is the angle the membrane normal makes with the magnetic field and $P_2(\cos \theta)$ is the second order Legendre polynomial.

Smoothed order parameter profiles constructed from the depaked spectra in Figure 5 on the assumption that S_{CD} monotonically

$[^2\text{H}_{62}]16:0-16:0 \text{ PC}/16:0-22:6 \text{ PC} (4:1)$



$16:0-16:0 \text{ PC}/[^2\text{H}_{31}]16:0-22:6 \text{ PC} (4:1)$

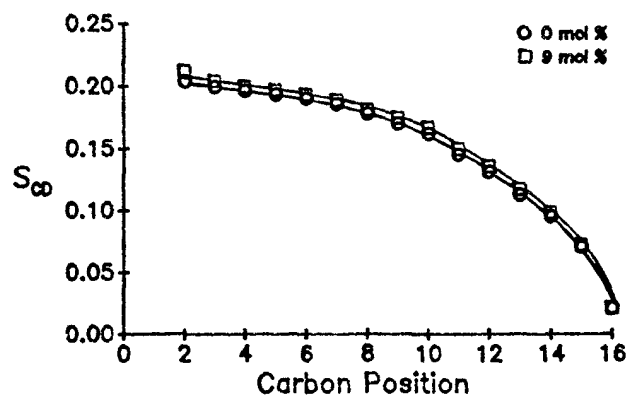


Figure 6. Order parameter profiles for $[^2\text{H}_{62}]16:0-16:0\text{PC}/16:0-22:6\text{PC}$ (4:1 mol ratio) membranes at 52°C and $16:0-16:0\text{PC}/[^2\text{H}_{31}]16:0-22:6\text{PC}$ (4:1 mol ratio) membranes at 50°C with 0 and 9 mol% α -tocopherol.

decreases along the chain from the membrane surface towards the centre are plotted in Figure 6 [17]. They confirm that α -tocopherol causes small comparable increases in order for the saturated and polyunsaturated components within the mixed membrane. The effect on the saturated phospholipid is, as also sensed by \bar{S}_{CD} (Figure 4), slightly bigger. It is furthermore demonstrated that the form of the profile is retained, which is consistent with earlier studies on single component PC-d_{31} membranes [5]. Specifically, α -tocopherol shifts upward the plateau region of almost constant order in the upper portion of the chain. The shift becomes progressively less in the lower portion where order gradually decreases towards the terminal methyl group.

CONCLUSION

The studies presented here illustrate that broadline ^2H NMR provides a superb, non-invasive probe of molecular interactions within membranes. They specifically represent an attempt to verify a proposal that vitamin E stabilizes membranes by interacting with polyunsaturated phospholipids. The results, although admittedly limited to a mixed saturated/polyunsaturated phospholipid membrane of single composition, do not offer evidence in favour of the hypothesis. A preference of α -tocopherol for the polyunsaturated component is implied when the saturated component becomes gel but, instead of a selective interaction based on polyunsaturated acyl chain conformation, is considered to reflect phase separation into liquid crystalline regions. When the saturated and polyunsaturated phospholipids are both liquid crystalline, moreover, they display comparable increases in order due to α -tocopherol.

ACKNOWLEDGMENTS

It is a pleasure to thank Ed Sternin for the generous gift of a copy of the depacking program and Margo Page for cheerful assistance in preparing the manuscript.

REFERENCES

1. Maggio, B., Diplock, A. T. and Lucy, J. A. (1977) *Biochem. J.* 161, 111-121.
2. Erin, A. N., Skrypin, V. V. and Kagan, V. E. (1985) *Biochim. Biophys. Acta* 815, 209-214.
3. Perly, B., Smith, I. C. P., Hughes, L. Burton, G. W. and Ingold, K. U. (1985) *Biochim. Biophys. Acta* 819, 131-135.
4. Ekiel, I. H., Hughes, G. W., Burton, G. W., Jovall, P. Å., Ingold, K. U. and Smith, I. C. P. (1988) *Biochemistry* 27, 1432-1440.
5. Wassall, S. R., Thewalt, J. L., Wong, L., Gorrissen, H. and Cushley, R. J. (1986) *Biochemistry* 25, 319-326.
6. Wassall, S. R., Wang, L., McCabe, R. C. Y., Ehringer, W. D. and Stillwell, W. (1991) *Chem. Phys. Lipids* 60, 29-37.
7. Davis, J. H. (1983) *Biochim. Biophys. Acta* 737, 117-171.

8. Pauls, K. P., MacKay, A. L. and Bloom, M. (1983) *Biochemistry* 22, 6101-6109.
9. McElhaney, R. N. (1982) *Chem. Phys. Lipids* 30, 229-259.
10. Davis, J. H. (1979) *Biophys. J.* 27, 339-358.
11. Barry, J. A., Trouard, T. P., Salmon, A. and Brown, M. F. (1991) *Biochemistry* 30, 8386-8394.
12. Ortiz, A., Aranda, F. J. and Gómez-Fernández, J. C. (1987) *Biochim. Biophys. Acta* 898, 214-222.
13. Seelig, J. (1977) *Quart. Rev. Biophys.* 10, 353-418.
14. Wassall, S. R., Phelps, T. M., Wang, L., Langsford, C. A. and Stillwell, W. (1989) *Progress in Clinical and Biological Research, Vol. 292: Biological and Synthetic Membranes* (Butterfield, D. A., Ed.) pp. 435-444, Alan R. Liss, Inc., New York.
15. Wassall, S. R., Yang, R. C., Wang, L., Phelps, T. M., Ehringer, W. and Stillwell, W. (1990) *Bull. Magn. Reson.* 12, 60-64.
16. Sternin, E., Bloom, M. and McKay, A. L. (1983) *J. Magn. Reson.* 55, 274-282.
17. Lafleur, M., Fine, B., Sternin, E., Cullis, P. R. and Bloom, M. (1989) *Biophys. J.* 56, 1037-1041.